Ernest Orlando Lawrence Berkeley National Laboratory

Technical Report
November 2010

Modeling Studies on the Transport of Benzene and H_2S in CO_2-Water Systems

Lawrence Berkeley National Laboratory (LBNL)

Contact:

Jens T. Birkholzer
Ph: (510) 486-7134
Email: jtbirkholzer@lbl.gov

Authors:
Liange Zheng, Nicolas Spycher, Jens Birkholzer,
Tianfu Xu, John Apps (LBNL)

Yousif Kharaka (USGS)

Submitted to:
U.S. Environmental Protection Agency

EPA Project Manager:
Sean Porse

Table of Contents

1. Introduction 5
2. Approach 8
3. Development of New Modeling Capabilities 10
   3.1. Coupling TMVOC with TOUGHREACT 10
      3.1.1. The Existing TMVOC Simulator 10
      3.1.2. The Existing TOUGHREACT Simulator 11
      3.1.3. The New TMVOC_REACT Simulator 11
   3.2. Partitioning of Benzene between CO_2 and Water 12
   3.3. Calculating the Phase Behavior of the $H_2S + CO_2 + H_2O$ System 13
4. Mobilization and Transport of Organics 14
   4.1. Relevant Processes and Conceptual Mobilization Scenario 14
   4.2. Organics of Concern, Properties, and Selection of Key Compound 15
   4.3. Mobilization of Benzene by Supercritical CO_2 in a Deep Saline Formation 20
      4.3.1. Benzene Content in Aqueous and Solid Phases in Deep Saline Aquifers 20
      4.3.2. Release of Benzene from Sediments 22
      4.3.3. 1-D Model 23
      4.3.4. 2-D Model 28
5. Impact of Co-Injection of CO_2 with H_2S 36
   5.1. Relevant Processes 36
      5.1.1. Phase Partitioning 37
      5.1.2. Chemical Processes in Response to H_2S+CO_2 Injection 37
   5.2. Fate of Co-injected H_2S in Deep Saline Aquifers 38
      5.2.1. H_2S Movement in the Storage Formation 38
      5.2.2. The Breakthrough of H2S through a Leakage Pathway 44
   5.3. Impact of co-injected H_2S on the quality of a fresh water aquifer 58
      5.3.1. Model Setup: Base Case 59
      5.3.2. Results of Base-Case Model 62
      5.3.3. Sensitivity Analysis 71
6. Summary and Conclusions 82

Acknowledgment 85

References 85

Appendix A 94
   A1. Solubility of CO_2 in Water and Brine 94
   A2. Mutual Solubility of Benzene and Water 95
   A3. Reformulation of Solubility Data as Equilibrium Constants 99
   A4. Binary Benzene + CO_2 System 103
   A5. Ternary Benzene+CO_2+Water System. 105
   A6. PVT Properties of $H_2S + CO_2$ Mixtures 108
   A7. Solubility of H_2S in Water 109
   A8. Distribution of Benzene between Kerogen and Water 116

List of Tables

Table 4.1. Some reported BTEX, PAHs and phenols concentration (mg/L) in production waters 16
Table 4.2. MCLs for benzene, benzo(a)pyrene (a common PAH compound) and some phenols. 16
Table 4.3. Comparison of solublities of benzene and some PAHs in supercritical CO_2 (400 bar and 50°C) and ambient water (25°C, 1 bar) unless shown otherwise 17
Table 4.4. Published partition coefficients of phenol between CO_2 and water. 18
Table 4.5. Benzene content of brines co-produced with crude oil (Zarrella et al., 1967) 21
Table 4.6. Variation of benzene concentrations in formation brines with distance from production (Zarrella et al., 1967). 21
Table 4.7. Benzene content in brines from wells in multiple test zones (Zarrella et al., 1967). 22
Table 4.8. Hydrogeologic properties for the base model 29
Table 5.1. Hydrodynamic parameters. 60
Table 5.2. Initial total aqueous concentration of major constituents obtained by initial equilibrium run for the base model. 60
Table 5.3. Kinetic properties for minerals considered in the model (see text for data sources). 61
Table 5.4. Surface complexation of lead on different minerals. 61
Table 5.5. Surface complexation of arsenic on different minerals. 62
Table 5.6. Computed speciation of aqueous lead for cases of intrusion of pure CO_2 ("pure CO_2") and H_2S+CO_2 mixture ("H_2S+CO_2") at 3.5 years. 66
Table 5.7. Mass distribution (% with respect to the total mass at t = 0) of Pb and As in solid form (in mineral or adsorbed on mineral surfaces) and in the aqueous phase at the start of simulations (initial t = 0) 69
Table 5.8. Computed arsenic speciation for cases of intrusion of pure CO_2 ("pure CO_2") and of a H_2S+CO_2 mixture (base case, "H_2S+CO_2") at 3.5 years. 69
Table A.1. List of references discussing the solubility of benzene in water 98
Table A.2. Mutual solubility data for the H_2O-benzene system vapor-liquid-liquid equilibrium at various temperatures and pressures, and fitted benzene log(K) values for Equation (3.3) (see text). 101
Table A.3. List of references discussing mutual solubility data for the binary benzene + CO_2 system. 104
Table A.4. Published partition coefficient of benzene between SCC and water (Ghonasgi et al., 1991). y_i and x_i are the mole fraction of benzene in SCC and water, respectively. 106
Table A.5. List of literature discussing H_2S solubility in water (note that published data at pressure around 1 bar are not included in this table) 111
Table A.6. Measured H_2S solubility (x= mole fraction) by Suleimenov and Krupp (1994) and calculated value by TMVOC_REACT. 112
Table A.7. Compilation of published K_d for benzene between soil and water 117
Table A.8. Published K_{ow} and K_{oc} (unitless). 118

List of Figures

Figure 1.1. Schematic illustrating potential groundwater quality changes in response to CO_2 leakage from deep storage sites. 5
Figure 4.1. Solubility of benzene/phenol in SCC at 40°C as a function of pressure. The solubilities of benzene in SCC are taken from Ohgaki and Katayama (1976), Gupta et al. (1982), Kim et al. (1986) while those for phenol are from Leer and Paulaitis (1980). 18
Figure 4.2. Solubility of benzene/phenol in SCC at 60°C as a function of pressure. The solubilities of benzene in SCC are taken from Ohgaki and Katayama (1976), while those for phenol are from Van Leer and Paulaitis (1980). 18
Figure 4.3. Solubility of benzene/phenol in SCC at 100°C as a function of pressure. The solubilities of benzene in SCC are taken from Kim et al. (1986), while those for phenol are from Pfohl et al. (1997). 18
Figure 4.4. Schematic representation of 1-D model, not to scale. 23
Figure 4.5. Computed distribution of SCC "liquid" saturation as a function of distance at different times, for a case when the partitioning of benzene into SCC is suppressed. 24
Figure 4.6. Computed benzene concentration in the aqueous phase as a function of distance at different times, for a case when the partitioning of benzene into SCC is suppressed. 24
Figure 4.7. Computed time evolution of benzene mass distribution in water (aqueous), SCC ("gas" phase) and sediments (adsorbed phase), as a percentage of total benzene mass. 25
Figure 4.8. Computed mass fraction of benzene in SCC at as a function of distance from the injection point, at different times. 26
Figure 4.9. Computed benzene concentration profiles in the aqueous phase as a function of distance from the injection point, at different times. 26
Figure 4.10. Computed mass fraction of benzene in SCC at 5 years, as a function of distance from the injection point: base case and case with smaller initial total benzene mass. 27
Figure 4.11. Computed benzene concentration profiles in the aqueous phase at 5 years, as a function of distance from the injection point: base case and case with smaller initial total benzene mass. 27
Figure 4.12. Computed mass fraction of benzene in SCC at 5 years, as a function of distance from the injection point: base case and case with 5x smaller initial benzene aqueous concentration. 28
Figure 4.13. Computed benzene concentration profiles in the aqueous phase at 5 years, as a function of distance from the injection point: base case and case with 5x smaller initial aqueous benzene concentration. 28
Figure 4.14. Schematic representation of hypothetical 2-D simulation scenario. 30
Figure 4.15. Numerical mesh for the vertical 2-D model 31
Figure 4.16. Computed initial (regional) pressure distribution (bar). 31
Figure 4.17. Computed initial (regional) temperature distribution (°C). 32
Figure 4.18. Computed spatial pressure distribution (left) and pressure buildup (the difference between the pressure at a given time and initial pressure) (right) after 3.5 years. 33
Figure 4.19. Computed spatial distribution of SCC ("liquid") saturation after 3.5 years. 33
Figure 4.20. Spatial distribution of benzene mass fraction in the compressed "gas" phase at 0.5 (a), 1.5 (b), 2.5 (c) and 3.5 years (d). 34
Figure 4.21. Spatial distribution of the concentration of aqueous benzene (molal) after 3.5 years 35
Figure 5.1. Schematic representation of the 2-D model used to simulate the movement of H_2S in a storage formation. 39
Figure 5.2. Contour of fluid saturation for the CO_2+H_2S supercritical mixture after 2 years of injection. 40
Figure 5.3. Contour of CO_2 mass fraction in the supercritical CO_2+H_2S supercritical mixture after 2 years of injection (the CO_2 mass fraction in the injected mixture is 0.95). 41
Figure 5.4. Profile of CO_2 mass fraction in the CO_2+H_2S supercritical mixture at z = -1900 (top of the storage formation) as a function of distance from the left model boundary after 2 years of injection (injection occurs at 200 m, with a CO_2 mass faction of 0.95). 41

Figure 5.5. Contour of H_2S mass fraction in the CO_2+H_2S supercritical mixture after 2 years of injection (the H_2S mass fraction in the injected fluid is 0.05). 42
Figure 5.6. Profile of H_2S mass fraction in the CO_2+H_2S supercritical mixture at z = -1900 (top of the storage formation) as a function of distance from the left model boundary after 2 years of injection (injection occurs at 200 m, with a H_2S mass faction of 0.05). 42
Figure 5.7. Contour of the concentration (molal) of dissolved CO_2 in the aqueous phase after 2 years of injection. 43
Figure 5.8. Profile of concentration (molal) of dissolved CO_2 in the aqueous phase at z = -1900 (top of the storage formation) as a function of distance from the left model boundary after 2 years of injection (injection occurs at 200 m). 43
Figure 5.9. Contour of concentrations (molal) of dissolved H_2S in the aqueous phase after 2 years of injection. 44
Figure 5.10. Profile of concentrations (molal) of dissolved H_2S in the aqueous phase at z = -1900 (top of the storage formation) as a function of distance from the left model boundary after 2 years of injection (injection occurs at 200 m). 44
Figure 5.11. Profile of temperature (thin line) and pressure (thick line) with depth assuming a hydrostatic pressure gradient and a geothermal gradient of 30 ^oC/1000 m (for use in computing the CO_2 and H_2S solubilities shown on Figure 5.12). 45
Figure 5.12. Computed solubilities (mass fraction) of CO_2 and H_2S in water as a function of depth, following temperature and pressure profiles shown on Figure 5.11. 46
Figure 5.13. Schematic representation of the 2-D model used to simulate leakage of a CO_2+H_2S supercritical mixture. 47
Figure 5.14. Snap shots of the "gas" plume fluid saturation at 0.5 (a), 1.5 (b), 2.5 (c), 3.5 (d) years. 48
Figure 5.15. Spatial pressure (bar) distribution after 3.5 years 49
Figure 5.16. Snap shots of pressure buildup (pressure at a given time minus initial pressure) at 0.5 (a), 1.5 (b), 2.5 (c), 3.5 (d) years. 50
Figure 5.17. Spatial distribution of mass fraction of H_2S in the compressed "gas" plume after 3.5 years of injection. 51
Figure 5.18. Profile of H_2S mass fraction in the compressed "gas" plume (YH_2S) at z = -1900 (top of the storage formation) as a function of distance from the left model boundary after 3.5 years of injection (injection occurs at 200 m). 52
Figure 5.19. Profile of H_2S mass fraction in gas phase (YH_2S) at z = -700 (top of the overlying aquifer) as a function of distance from the left model boundary after 3.5 years of injection (leakage into the aquifer occurs at 300 m). 52
Figure 5.20. Spatial distribution of CO_2 mass fraction in the compressed "gas" phase after 3.5 years. 53
Figure 5.21. Profile of CO_2 mass fraction in the compressed "gas" plume (YCO_2) at z = -1900 (top of the storage formation) as a function of distance from the left model boundary after 3.5 years of injection (injection occurs at 200 m). 53
Figure 5.22. Profile of CO_2 mass fraction in the compressed "gas" plume (YCO_2) at z = -700 (top of the overlying aquifer) as a function of distance from the left model boundary after 3.5 years of injection (leakage into the aquifer occurs at 300 m). 54
Figure 5.23. Time evolution of the H_2S mass fraction (YH_2S) in the compressed "gas" plume at the bottom of the fracture (A), where the fracture connects to the storage formation, and at the top of the fracture (B), where the fracture connects to the overlying aquifer. 55
Figure 5.24. Time evolution of the CO_2 mass fraction (YCO_2) in the compressed "gas" plume at the bottom of the fracture (A), where the fracture connects to the storage formation, and at the top of the fracture (B), where the fracture connects to the overlying aquifer. 55
Figure 5.25. Spatial distribution of CO_2 concentration (molal) in the aqueous phase after 3.5 years of injection. 56
Figure 5.26. Profile of CO_2 concentration (XCO_2) in the aqueous phase at z = -1900 (top of the storage formation) as a function of distance from the left model boundary after 3.5 years of injection (injection occurs at 200 m). 56

Figure 5.27. Profile of CO_2 concentration (molal) in the aqueous phase at z = -700 (top of the overlying aquifer) as a function of distance from the left model boundary after 3.5 years of injection (leakage into the aquifer occurs at 300 m). 57
Figure 5.28. Spatial distribution of H_2S concentration (molal) in the aqueous phase after 6 years of injection. 57
Figure 5.29. Profile of dissolved H_2S concentration (molal) in the aqueous phase at z = -1900 (top of the storage formation) as a function of distance from the left model boundary after 6 years of injection (injection occurs at 200 m). 58
Figure 5.30. Profile of dissolved H_2S concentration (molal) in aqueous phase at z = -700 (top of the overlying aquifer)as a function of distance from the left model boundary after 6 years of injection (leakage into the aquifer occurs at 300 m). 58
Figure 5.31. Schematic representation for the setup of the reactive transport model 60
Figure 5.32. Spatial distribution of intruding CO_2+H_2S fluid saturation at 100 years 63
Figure 5.33. pH profile along x at y=0 at different times (the CO_2+H_2S mixture intrudes at x= 105 m) 63
Figure 5.34. Total aqueous sulfide concentration profile (as HS^-) along x at y=0 at different times (the CO_2+H_2S mixture intrudes at x= 105 m). 64
Figure 5.35. Profile of the goethite volume fraction change (dimensionless) along x at y=0 at different times (the CO_2+H_2S mixture intrudes at x= 105 m). 64
Figure 5.36. Profile of the pyrite volume fraction change (dimensionless) along x at y=0 at different times. 65
Figure 5.37. Profile of total ferrous iron concentration (as Fe^{+2}) along x at y=0 at different times. 65
Figure 5.38. Profile of the total sorbed lead along x at y=0 at different times. 66
Figure 5.39. Profile of the galena volume fraction change (dimensionless) along x at y=0 at different times 67
Figure 5.40. Profile of lead concentration along x at y=0 at different times, also shown is the Maximum Contaminants Level (MCL) of lead. 68
Figure 5.41. Profile of total sorbed arsenic concentrations (left) and relative change in these concentrations (right, see text) along x at y=0 at different times. 70
Figure 5.42. Profile of the arsenian pyrite volume fraction change (dimensionless) along x at y=0 at different times. 70
Figure 5.43. Profile of the orpiment volume fraction change (dimensionless) along x at y=0 at different times. 70
Figure 5.44. Profile of the arsenic concentration along x at y=0 at different times. 71
Figure 5.45. Profile of the goethite volume fraction change along x at y=0 at different times (left) and the comparison of the goethite volume fraction change at 100 years between the sensitivity run and base-case model (right). 72
Figure 5.46. Profile of the pyrite volume fraction change along x at y=0 at different times (left) and the comparison of the pyrite volume fraction change at 100 years between the sensitivity run and base-case model (right). 72
Figure 5.47. Profile of total aqueous sulfide concentration (as HS^-) along x at y=0 at different times (left) and comparison of the ferrous iron concentration at 100 years between the sensitivity run and base-case model (right). 72
Figure 5.48. Profile of total ferrous iron concentration (as Fe^{+2}) along x at y=0 at different times (left) and the comparison of the ferrous iron concentration at 100 years between sensitivity run and base model (right). 73
Figure 5.49. Profile of the siderite volume fraction change along x at y=0 at different times. 73
Figure 5.50. Profile of total sorbed lead along x at y=0 at different times. 74
Figure 5.51. Profile of galena volume fraction change along x at y=0 at different times. 74
Figure 5.52. Profile of aqueous lead concentration along x at y=0 at different times. 74
Figure 5.53. Comparison of lead concentration at 20 (left) and 100 years between sensitivity run and base model. 75
Figure 5.54. Profile of the total sorbed arsenic (left) and the relative change (right) along x at y=0 at different times 76
Figure 5.55. Comparison of total adsorbed arsenic change at 100 years for the sensitivity run and base-case model. 76

Figure 5.56. Profile of arsenic concentration along x at y=0 at different times. 76
Figure 5.57. Profile of arsenian pyrite (left) and orpiment (right) volume fraction change along x at y=0 at different times. 77
Figure 5.58. Comparison of the ferrous iron concentration at 100 years for the sensitivity run and base-case model. The Y axis on the left figure is linear, and the Y axis on the right figure is logarithmic. The MCL for arsenic is also shown in the right figure. 77
Figure 5.59. Profile of orpiment volume fraction change along x at y=0 at different times. 78
Figure 5.60. Profile of hydrogen sulfide concentration along x at y=0 at different times. 78
Figure 5.61. Profile of the arsenic concentration along x at y=0 at different times (left) and the comparison of the arsenic concentration at 100 years between the sensitivity run and base-case model (right), note that the Y axis on the left figure is linear, and the Y axis on the right figure is logarithmic. 79
Figure 5.62. Profile of the hydrogen sulfide concentration along x at y=0 at different times (left) and the comparison of the hydrogen sulfide concentration at 100 years between sensitivity run and base model (right). 79
Figure 5.63. Profile of the total adsorbed lead along x at y=0 at different times (left) and comparison of the total adsorbed lead at 5 years between the sensitivity run and base-case model (right). 80
Figure 5.64. Profile of the lead concentration along x at y=0 at different times (left) and comparison of the lead concentration at 100 years between the sensitivity run and base-case model (right). 80
Figure 5.65. Profile of total adsorbed arsenic concentration change (%) along x at y=0 at different times (left) and comparison of the total adsorbed arsenic concentration change at 100 years between the sensitivity run and base-case model (right). 81
Figure 5.66. Profile of aqueous arsenic concentrations along x at y=0 at different times (left) and comparison of the total adsorbed arsenic change at 100 years between the sensitivity run and base model (right). Note that the Y axis on the left figure is linear, and the Y axis on the right figure is logarithmic. 81
Figure A.1. Measured (Koschel et al., 2006) and calculated CO_2 solubilities in water at 50 °C by TMVOC_REACT and ECO2N. 94
Figure A.2. Measured (Koschel et al., 2006; Pfohl et al., 1997) and calculated CO_2 solubilities in water at 100 °C by TMVOC_REACT(Pruess, 2005). 95
Figure A.3. Pressure–temperature phase diagram for the water–benzene mixture — thick solid lines: one-phase critical curve and liquid–liquid–vapor (LLV) three-phase equilibrium curve; c.p.: critical point (Furutaka and Ikawa, 2001). 96
Figure A.4. Solubility of several hydrocarbons in water as a function of temperature at saturation pressures (GSPA, 2004). 97
Figure A.5. Published solubility data for benzene in water, as a function of temperature (at saturation pressures). 98
Figure A.6. Mole fraction of benzene in water as a function of vapor (total) pressure (at saturation temperatures). 99
Figure A.7. Mole fraction of benzene in water as a function of pressure at liquid-liquid equilibrium at temperature ranging from 25–200°C (Miller and Hawthorne, 2000)) and along the three-phase pressure curve (Neely et al., 2008) at saturation temperatures. 99
Figure A.8. Fitted equilibrium constant (log(K)) for Equation (3.3) compared to published solubility data and Henry's constants as a function of temperature (assuming negligible pressure effect over the fitted P-T range). Also shown is the log(K) calculated from published standard Gibbs free energy data at 25°C, 1 bar. 102
Figure A.9. Measured and computed mole fraction of benzene in water for benzene-H_2O vapor-liquid-liquid equilibrium as a function of temperature, ignoring pressure effects. 102
Figure A.10. Equilibrium constants for the equilibrium between liquid benzene and benzene in water calculated from Neely et al. (2008) and the fitting polynomial equation. 103
Figure A.11. Published vapor pressure data versus CO_2 mole fraction in the liquid phase at 25°C for the benzene-CO_2 system. "VP C6H6" is the vapor pressure of pure benzene whereas "VP CO_2" is that of pure CO_2. 104

Figure A.12. Published vapor pressure data versus CO_2 mole fraction in the liquid phase at 40°C. "VP C6H6" is the vapor pressure of pure benzene while "VP CO_2" is that of pure CO_2. 105
Figure A.13. Comparison of measured partition coefficients of benzene between water and SCC (symbols) and calculated values by TMVOC_REACT at 40°C (line). 107
Figure A.14. Comparison of measured partition coefficients of benzene between water and SCC (symbols) and calculated values by TMVOC_REACT at 50°C (line). 107
Figure A.15. Comparison of benzene mole fraction in water, x_i, derived from experimental measurements (symbols), and calculated values by TMVOC_REACT at 40°C (line). 107
Figure A.16. Pressure-Temperature diagram for H_2S+CO_2 mixtures (Bierlein and Kay, 1953) 108
Figure A.17. Measured (Chapoy et al., 2005) and calculated H_2S solubilities in water at 35°C (right) and 45°C (left). 113
Figure A.18. Measured (Chapoy et al., 2005) and calculated H_2S solubilities in water at 55°C (right) at 65°C (left). 113
Figure A.19. Measured (Pohl, 1961) and calculated H_2S solubilities in water as a function of temperature at pressure of 17 bar. 113
Figure A.20. Measured (Gilespie et al., 1984; Selleck et al., 1952) and calculated H_2S solubilities in water by TMVOC_REACT and TMVOC (Pruess and Battistelli, 2002) 114
Figure A.21. Measured (Koschel et al., 2007) and calculated H_2S solubilities in water by TMVOC_REACT. 115
Figure A.22. Measured (Xia et al., 2000) and calculated H_2S solubilities in 4M NaCl solution at 40°C (right) and 60°C (left). 115
Figure A.23. Measured (Xia et al., 2000) and calculated H_2S solubilities in 4M NaCl solution at 80°C (right) and 120°C (left). 115
Figure A.24. Measured (Xia et al., 2000) and calculated H_2S solubilities in 6M NaCl solution at 40°C (right) and 60°C (left). 116
Figure A.25. Measured (Xia et al., 2000) and calculated H_2S solubilities in 6M NaCl solution at 80°C (right) and 120°C (left). 116

List of Acronyms and Abbreviations

As	Arsenic
BTEX	Benzene, Toluene, Ethylbenzene, and Xylenes
CCS	Carbon Capture and geologic Storage
EPA	Environmental Protection Agency
NAPL	Nonaqueous Phase Liquids
NCG	Noncondensable Gases
MCL	Maximum Contaminant Level
PAH	Polycyclic Aromatic Hydrocarbons
Pb	Lead
SCC	Supercritical CO_2
VOC	Volatile Organic Compounds

List of Referenced Minerals and Their Chemical Formulas

Name	**Formula**
Ankerite	$Ca(Mg_{0.3}Fe_{0.7})(CO_3)_2$
Arsenian pyrite	$FeAs_{0.05}S_{1.95}$
Calcite	$CaCO_3$
Chlorite	$Mg_{2.5}Fe_{2.5}Al_2Si_3O_{10}(OH)_8$
Dawsonite	$NaAlCO_3(OH)_2$
Dolomite	$CaMg(CO_3)_2$
Ferroselite	$FeSe_2$
$FeS_{(am)}$	FeS
Galena	PbS
Goethite	FeO(OH)
Illite	$K_{0.6}Mg_{0.25}Al_{1.8}Al_{0.5}Si_{3.5}O_{10}(OH)_2$
K-feldspar	$KAlSi_3O_8$
Kaolinite	$Al_2Si_2O_5(OH)_4$
Oligoclase	$CaNa_4Al_6Si_{14}O_{40}$
Orpiment	As_2S_3
Pyrite	FeS_2
Pyromorphite	$Pb_5(PO_4)_3(Cl)$
Quartz	SiO_2
Realgar	AsS
Smectite-Ca	$Ca_{0.145}Mg_{0.26}Al_{1.77}Si_{3.97}O_{10}(OH)_2$
Smectite-Na	$Na_{0.290}Mg_{0.26}Al_{1.77}Si_{3.97}O_{10}(OH)_2$

Executive Summary

CO_2 sequestration into deep reservoirs must ensure the safety of overlying groundwater aquifers. Questions exist whether groundwater could become contaminated by leakage and upward migration of CO_2, possibly comprising co-injected H_2S and/or organic compounds mobilized by supercritical CO_2 (SCC) at depth.

In the first part of an EPA-funded project on potential effects of carbon capture and geologic storage (CCS) on groundwater resources (Birkholzer et al., 2008), we evaluated the potential for mobilization of trace elements in response to CO_2 intrusion via systematic reactive-transport simulations involving hypothetical release scenarios (Zheng et al., 2009; Apps et al., 2010). Other researchers have investigated this issue by laboratory experiments (e.g., Carroll, 2009; McGrath et al., 2007; Smyth et al., 2009) as well as modeling work integrated with controlled field experiments of CO_2 release in freshwater aquifers (e.g., Kharaka et al., 2010; Ambats et al., 2009).

Less work has been conducted with respect to the potential impact on groundwater from organic constituents and co-injectants such as H_2S. This report presents research related to these issues, and completes the second chapter of the aforementioned EPA-funded project. The objective of this study was primarily the development of modeling capabilities to assess the mobilization and transport of organics with supercritical CO_2, and the co-injection and transport of H_2S with SCC. Focus was given to mobilization/transport aspects more than to actual effects on shallow groundwater quality, since these effects would vary depending on aquifer characteristics such as water composition, mineralogy, sorption behavior, and pH buffering capacity. Specific project goals included:

- The upgrade of TOUGHREACT modules to allow simulation of multiphase flow and transport of multiple gases, including SCC and H_2S
- The implementation, into the simulator, of phase-partitioning data for H_2S and at least one key organic compound with SCC/water mixtures
- Identification of key organics of potential concern if mobilized by SCC
- Simulation of CO_2 deep injection, leaching of organics, and a hypothetical leak scenario to a shallower aquifer
- Simulation of H_2S/CO_2 deep co-injection and a hypothetical leak scenario to a shallower aquifer
- Simulation of the groundwater quality changes in response to the leakage of mixture of $H_2S + CO_2$.

To meet the specific needs for this project, the existing simulator TMVOC (Pruess and Battistelli, 2002) was coupled with the chemical reaction module of TOUGHREACT (Xu et al., 2006) to yield a new simulator referred to as TMVOC_REACT. New features in TMVOC_REACT relative to TMVOC include:

- Incorporation of phase-partitioning relationships and transport capabilities for benzene, water, and SCC mixtures, using data from the literature

- Incorporation of aqueous CO_2 solubility modules from module ECO2N (Pruess, 2005)
- Incorporation of aqueous H_2S solubilities from the model presented by Duan et al. (2007)

Organic compounds that could potentially be mobilized by SCC were evaluated in terms of probability of occurrence and abundance in deep storage formations, as well as potential for environmental hazard. Benzene, PAHs, and phenols were identified as good candidates for further evaluation. Of these, benzene was selected for further investigation by numerical modeling because of: (1) its relatively low Maximum Contaminants Level (MCL), (2) its high solubility in SCC, (3) its relatively high solubility in water and (4) its high partition coefficient between SCC and water.

Numerical simulations were conducted to evaluate the possible mobilization of benzene by SCC. A prescribed amount of benzene was assumed initially present in the storage formation, both in the aqueous phase and tied to solid phases. A literature search was conducted to obtain reasonable initial conditions and define appropriate ranges for key parameters. A one-dimensional (1-D) model was first established to evaluate the mobilization of benzene by SCC in a deep saline aquifer, from an area where the sediments contain benzene, to a downstream region that is initially benzene free. The objective of these simulations was to test the code's capability to simulate the transport of benzene, and to identify the transport and chemical processes that control the mobilization of benzene by SCC. Two-dimensional (2-D) models were then developed for a hypothetical scenario in which benzene is mobilized by SCC injection into a deep saline reservoir, and then transported vertically along a preferential pathway into an overlying shallow aquifer. Upon CO_2 injection, benzene preferentially partitions into SCC, and is therefore depleted from the solid and aqueous phases. Because SCC is buoyant in water, it has the potential to migrate upward through a fault or another preferential pathway. The mutual solubilities of the components involved (CO_2, benzene, and water) change as a function of pressure and temperature, and therefore the partitioning behavior changes along the flow path. Thus, the main question is whether the transport of benzene in SCC along a leakage pathway could impact overlying fresh water aquifers. Model results indicate that benzene may co-migrate with CO_2 into overlying aquifers if a leakage pathway were present. Because the aqueous solubility of benzene in contact with CO_2 is lower than the aqueous solubility of CO_2, benzene becomes enriched in the CO_2 phase as the SCC plume advances. For the case studied here, which considered a 1100 m long preferential pathway, the predicted aqueous benzene concentration mobilized by SCC to the overlying aquifer is on the same order of magnitude as the initial concentration in the storage formation.

Simulations were also conducted for the case of H_2S co-injection with CO_2. As for benzene, the fate of H_2S in the storage formation and its behavior along a potential leakage pathway are controlled by chromatographic partitioning between the gas (CO_2) and the aqueous phase (brine). The component with lower solubility in the aqueous phase is preferentially enriched into the gas phase and vice versa. However, contrary to benzene, the solubility of H_2S in water is higher than its solubility in SCC, and therefore H_2S tends

to become depleted from the CO_2 phase as the SCC plume advances. The main question in this case is whether H_2S could completely leach out of the SCC plume before it reaches an overlying aquifer. Three different 2-D models were set up to evaluate the potential for groundwater contamination by H_2S. The first model comprises the storage formation and a sealing cap rock. This model was established to assess the fate of H_2S within the storage formation. A second model similar to that used for the benzene transport case was developed to investigate how H_2S might migrate along a leakage pathway. Model results suggest that:

1. Leakage pathways may allow co-migration of CO_2+H_2S despite the preferential dissolution (stripping) of H_2S at the edge of the advancing CO_2+H_2S plume.
2. There is some delay between the CO_2 and H_2S times of arrival (into the shallow aquifer) caused by the preferential dissolution of H_2S over CO_2, but this effect does not last very long.
3. Once this stripping effect is over, H_2S co-migrating with CO_2 is predicted to enter the aquifer at about the same concentration as in the CO_2 stream injected into the deep formation.

A third model was used to evaluate the potential consequences of CO_2 plus H_2S leaking into a hypothetical shallow groundwater aquifer. The setup of this third model, including hydrogeologic properties, initial chemical composition of groundwater, and chemical reaction network, is similar to that adopted in the first part of this project (Birkholzer et al., 2008; Zheng et al., 2009). The differences from the previous model are: (1) a mixture of 95% CO_2 and 5% H_2S instead of pure CO_2 is considered; and (2) arsenic sulfides (orpiment, As_2S_3, and realgar, As_4S_4) are added to the list of potentially forming secondary phases. In addition to the adverse effects of H_2S itself (i.e., odor and taste), the leakage of H_2S (in addition to CO_2) is likely to exacerbate impacts on shallow groundwater. Possible geochemical reactions induced by the leakage of a H_2S+CO_2 mixture are as follows:

1. Desorption of lead and arsenic, mainly due to aqueous complexation with sulfide, could lead to increased concentrations of aqueous lead and arsenic.
2. The precipitation of pyrite (and/or FeS) could partly mitigate elevated aqueous sulfide concentrations, or could even sequester a large portion of the injected H_2S if there were a sufficient amount of ferrous iron supplied in the aquifer, either produced by the reduction of Fe(III) (hydr)oxides, or present in other minerals.
3. The reductive dissolution of Fe(III) (hydr)oxides could produce significant amounts of ferrous iron, and may therefore be critical for dampening the adverse effects of H_2S by precipitation of pyrite (and/or FeS). However, the precipitation of siderite may compete with sulfide for ferrous iron. Whether siderite precipitates or not depends on the relative rates of Fe mineral dissolution and precipitation, and on other conditions such as temperature, pressure, and concentration of bicarbonate.
4. The desorption of arsenic could be accompanied by the precipitation of arsenian pyrite and orpiment. The precipitation of these minerals would dampen aqueous

arsenic concentrations, although these concentrations could remain very high in sulfidic waters.

The assessment of organic compound and/or metal mobilization by CO_2 leakage from deep aquifers requires knowledge of many parameters, including the nature of phases associated with organics and metals, as well as sediment sorption characteristics for these compounds. These properties are not only quite site specific, they are also mostly unknown. Therefore, any exploratory, generic, modeling must rely on assumptions that are approximate at best, yielding results that should be regarded as more qualitative than quantitative, and highly dependent on those assumptions. For these reasons, it must be pointed out that the simulations presented in this report are primarily intended to illustrate the capabilities of the new simulator and to provide a better understanding of the various processes at play for hypothetical scenarios. Model results are not intended as realistic assessments of groundwater quality changes for specific sites, and they certainly do not provide an exhaustive evaluation of all possible site conditions, given the large variability and uncertainty of hydrogeologic and geochemical key parameters. The code capabilities developed here will become useful, however, when site-specific studies are being attempted in the future.

1. Introduction

Carbon dioxide (CO_2) buildup in the atmosphere could be mitigated through its capture from stationary sources, such as coal-burning power plants, and subsequent injection into suitable deep geologic formations for long-term storage. As a result, many studies have been undertaken to assess the feasibility of carbon capture and geologic storage (CCS) as a mitigation measure to curb rising CO_2 emissions. Proper site selection and management of CO_2 storage projects will minimize risks to human health and the environment (Bachu, 2000). However, it is possible that CO_2 could migrate from a storage formation into overlying aquifers containing drinking water. The schematic in Figure 1.1 shows such a scenario, in which a local high-permeability pathway—such as a permeable fault or an open abandoned well—would allow CO_2 to escape from depth and reach a shallow aquifer. The buoyant CO_2 would undergo a phase transition during transit and would typically reach shallow aquifers in a gaseous state and partially or completely dissolve into the groundwater.

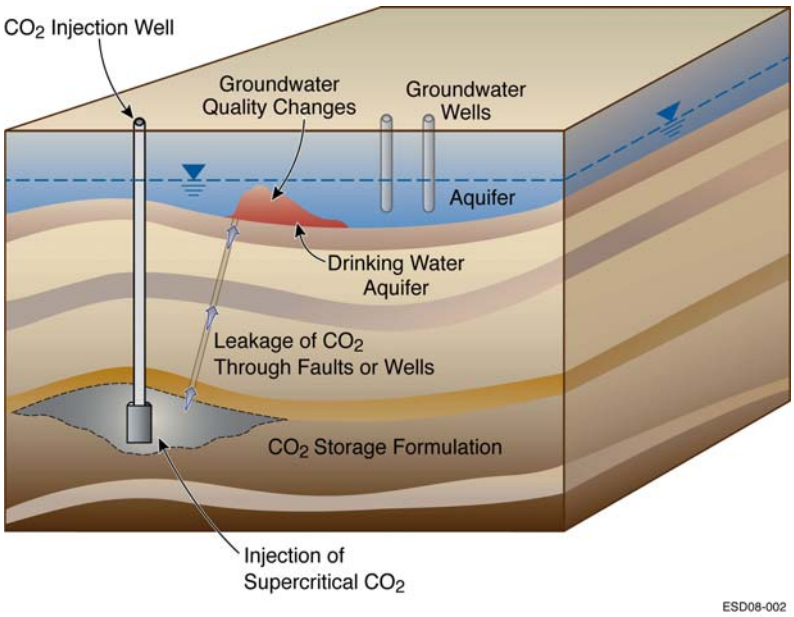

Figure 1.1. Schematic illustrating potential groundwater quality changes in response to CO_2 leakage from deep storage sites.

The leakage of CO_2 could affect overlying potable aquifers in several ways. First, the dissolution of CO_2 in water increases the concentration of dissolved carbonic acid and thus increases acidity, which could mobilize trace elements through mineral dissolution, desorption reactions, and/or exchange reactions involving H^+ and other mobilized constituents (Aiuppa et al., 2005; Ambats et al., 2009; Zheng et al., 2009). In addition, the increased dissolved CO_2 concentrations could result in desorption of metals such as arsenic (As) by competitive sorption of carbonate ions (Appelo et al., 2002). Second, because supercritical CO_2 (SCC) is also an excellent solvent for organic compounds

(Anitescu and Tavlarides, 2006), concerns have been raised about the potential mobilization of organic constituents from depth and subsequent transport to shallow drinking water bodies via leakage pathways. Third, co-injectants such as H_2S, if migrating with leaking CO_2, may exacerbate the impact on groundwater quality by the formation of strong metal-sulfide complexes, reductive dissolution of metal-sorbing Fe(III) hydroxides, and/or strong effects of pH decrease from sulfide oxidation (Palandri and Kharaka, 2005; Xu et al., 2007).

In the first part of an EPA-funded project on CCS and groundwater resources (Birkholzer et al., 2008), we evaluated the potential for mobilization of trace elements in response to CO_2 intrusion via a comprehensive reactive-transport simulation study involving hypothetical release scenarios (Zheng et al., 2009; Apps et al., 2010). Other researchers have investigated this issue by laboratory experiments (Carroll, 2009; McGrath et al., 2007; Smyth et al., 2009) as well as modeling work integrated with controlled field experiments of CO_2 release in freshwater aquifers (Ambats et al., 2009; Kharaka et al., 2010).

Less work has been conducted with respect to potential impact on groundwater from organic constituents and co-injectants such as H_2S. For example, while the possible extraction of organic compounds by supercritical CO_2 in deep reservoirs is a well-known phenomenon (e.g., Kharaka and Hanor, 2007), the potential for groundwater contamination from mobilized organic constituents transported to shallow aquifers has not been studied to date, to our knowledge. The effect of co-injected H_2S on mineral trapping of CO_2 and mineralogical alteration of reservoir host rocks has been studied previously (Gunter et al., 2000 and 2005; Knauss et al., 2005; Palandri and Kharaka, 2005; Palandri et al., 2005; Xu et al., 2007), but with focus on the geochemical evolution in the storage formation at relatively high temperature and pressure ($T>70^oC$, $P>150$ bar). The behavior of co-injected H_2S along a leakage pathway, while affected by chromatographic partitioning between CO_2 and water (Bachu and Bennion, 2009; Bachu et al., 2009), and/or the potential consequence of CO_2 plus H_2S intruding into a shallow groundwater aquifer, have remained largely uninvestigated.

This report presents research related to these issues and completes the second chapter of the abovementioned EPA-funded project. The objective of this study was primarily the development of modeling capabilities to assess the mobilization and transport of organics with SCC, and the co-injection and transport of H_2S with SCC. Focus was given to mobilization/transport aspects more than to actual effects on shallow groundwater quality, since these effects would vary depending on aquifer characteristics such as water composition, mineralogy, sorption, and pH buffering capacity. Specific project goals included:

- The upgrade of TOUGHREACT modules to allow simulation of multiphase flow and transport of multiple gases, including SCC and H_2S
- Identification of key organics of potential concern if mobilized by SCC
- The implementation, into the simulator, of phase-partitioning data for H_2S and at least one key organic compound with SCC/water mixtures

- Simulation of H_2S/CO_2 deep co-injection and a hypothetical leak scenario to a shallower aquifer
- Simulation of CO_2 deep injection, leaching of organics, and a hypothetical leak scenario to a shallower aquifer

Benzene was chosen as one of the key compounds to consider for potential mobilization by SCC, the rationale for which is presented later in this report. The mobilization of benzene by SCC and its subsequent transport along an assumed leakage pathway was investigated by numerical modeling. The co-injection and transport of H_2S, along with CO_2, from a deep storage formation to an overlying aquifer was also simulated to evaluate the potential deleterious effects of CO_2 plus H_2S intrusion on shallow groundwater quality. Significant code development work was necessary for this purpose, because existing simulators were not capable of handling all relevant processes.

It should be pointed out that the simulations presented in this report are mostly intended to illustrate the capabilities of the new simulator and to provide a better understanding of the various processes at play for hypothetical scenarios. Model results are not intended as realistic assessments of groundwater quality changes for specific sites, and they certainly do not provide an exhaustive evaluation of all possible site conditions, given the large variability and uncertainty of hydrogeologic and geochemical key parameters. The code capabilities developed here will become useful, however, when site-specific studies are being attempted in the future.

2. Approach

This investigation relies entirely on numerical simulations. Evaluating the mobilization of organic compounds and potential effect of H_2S co-injection requires predictive capabilities for a significant number of coupled processes. These include multiphase flow and transport, fluid-phase equilibria, solvent properties of supercritical CO_2, geochemical speciation, mineral dissolution and precipitation, adsorption/desorption, and cation exchange. The coupling of all these processes poses a challenge to existing simulators. The TOUGH family of codes comprises different simulators that can deal with some, but not all of these processes combined. For example, TMVOC (Pruess and Battistelli, 2002) is a numerical simulator for three-phase nonisothermal flow of water, noncondensible gases, and a multicomponent mixture of volatile organic chemicals (VOCs) in saturated-unsaturated media. Thus, TMVOC can handle transport of organics and gas mixtures, but lacks the necessary reactive-transport modeling capabilities offered by TOUGHREACT (Xu et al., 2006). TOUGHREACT, in turn, does not provide for handling of arbitrary gas mixtures and/or organic solvents.

To meet the specific needs for this project, the existing simulator TMVOC was coupled with the chemical-reaction module of TOUGHREACT. The new simulator is referred to hereafter as TMVOC_REACT. Enhancements made to TMVOC_REACT in terms of multiphase flow, relative to the original TMVOC code, include:

- Incorporation of phase-partitioning relationships and transport capabilities for benzene, water, and SCC mixtures, using data from the literature;
- Incorporation of aqueous CO_2 solubility modules from module ECO2N (Pruess, 2005) and verifying its functionality against published data;
- Incorporation of aqueous H_2S solubilities from the model presented by Duan et al. (2007) and verification against published data.

Details on this code development effort are provided in Section 3.

In Section 4, TMVOC_REACT is used to simulate a hypothetical scenario in which an organic constituent (benzene) is mobilized by SCC injection into a deep saline reservoir, then transported through a preferential pathway into a shallow aquifer. The behavior of CO_2 plus benzene moving up a leakage pathway was investigated. Benzene was selected as an organic compound that could be mobilized, for reasons explained in Section 4.2. It is assumed in the simulations that a prescribed amount of benzene is initially present in the storage formation, both in the aqueous phase and tied to solid phases. Upon CO_2 injection, benzene preferentially partitions into SCC, and for this reason is depleted from the solid and aqueous phases. The main concern is then the transport of benzene in SCC, because SCC is buoyant in water and thus has the potential to migrate upward through a fault or another preferential pathway. Mutual solubilities of the components involved (CO_2, benzene, and water) change as a function of pressure and temperature, and therefore the partitioning behavior can change along the flow path. An extensive literature search was conducted to obtain reasonable initial conditions and define appropriate ranges for key parameters. Both 1-D and 2-D models were developed to

investigate the benzene leaching/transport scenario. The 1-D model was established to gain insight on the mobilization and transport of benzene at depth in the modeled CO_2 reservoir formation. The objective here was to test the capability of the simulator and to identify sensitive transport and chemical input parameters by sensitivity analyses at a relatively low computing cost. A vertical 2-D model was subsequently set up for the hypothetical leak scenario.

Section 5 describes simulations conducted for the case of H_2S co-injection with CO_2. The fate of H_2S in the storage formation and its behavior along a potential leakage pathway are controlled by chromatographic partitioning between the gas (CO_2) and the aqueous phase (brine). The component with lower solubility in the aqueous phase is preferentially enriched into the gas phase and vice versa. Three different 2-D models were set up to evaluate the potential for groundwater contamination. The first model includes the storage formation and a sealing cap rock. This model was established to assess the fate of H_2S within the storage formation (Section 5.1). A second model similar to that used for the benzene transport case was developed to investigate how H_2S might migrate along a leakage pathway (Section 5.2). A third model was used to evaluate the potential consequences of CO_2 plus H_2S leaking into a hypothetical shallow groundwater aquifer (Section 5.3). The setup of this third model, including hydrogeologic properties, initial chemical composition of groundwater, and chemical reaction network, is described in Section 5.3.1 and is similar to that adopted in the first part of this project (Birkholzer et al., 2008; Zheng et al., 2009). The differences from the previous model setup are: (1) a mixture of 95% CO_2 and 5% H_2S instead of pure CO_2 is considered; and (2) arsenic sulfides (orpiment, As_2S_3, and realgar, As_4S_4) are added to the list of potentially forming secondary phases.

3. Development of New Modeling Capabilities

This section describes the model development work undertaken to provide simulation capabilities for (1) the mobilization and reactive transport of organic compounds in deep saline aquifers affected by CO_2 injection, and (2) the potential geochemical effects of H_2S co-injection with CO_2. As mentioned earlier, this requires consideration of a significant number of complex thermal, physical and chemical processes, which poses a challenge to existing simulators. We describe in this section how we have modified and coupled two existing simulators, TMVOC (Pruess and Battistelli, 2002) and TOUGHREACT (Xu et al., 2006), to develop a new modeling tool for the purpose at hand.

3.1. Coupling TMVOC with TOUGHREACT

3.1.1. *The Existing TMVOC Simulator*

TMVOC (Pruess and Battistelli, 2002) is a numerical simulator for three-phase nonisothermal flows of multicomponent hydrocarbon mixtures in variably saturated heterogeneous media. TMVOC was initially designed for studying subsurface contamination by volatile organic compounds (VOCs), such as hydrocarbon fuels and industrial solvents. It can model the one-, two-, or three-dimensional migration of nonaqueous phase liquids (NAPLs) through the unsaturated and saturated zones, the formation of an oil lens on the water table, the dissolution and subsequent transport of VOCs in groundwater, as well as the vaporization and migration of VOCs in the interstitial air of the unsaturated zone, and the reversible sorption of VOCs on the rock matrix of a porous medium. TMVOC accounts for differences in aqueous solubility and volatility of different VOCs that may be present in a NAPL. Thermal remediation treatments such as steam injection or electric resistance heating and associated phase change and flow effects can also be modeled.

In the TMVOC formulation, the multiphase system is assumed to be composed of water, noncondensable gases (NCGs), and water-soluble volatile organic chemicals (VOCs). The number and nature of NCGs and VOCs can be specified by the user. NCGs may be selected by the user from a data bank provided in TMVOC; currently available choices include O_2, N_2, CO_2, CH_4, ethane, ethylene, acetylene, and air (a pseudo-component treated with properties averaged from N_2 and O_2). In most TMVOC applications, just a single NCG, air, will be present. Thermophysical property data for VOCs must be provided by the user. The fluid components may partition (volatilize and/or dissolve) among gaseous, aqueous, and NAPL phases. Any combination of the three phases may be present, and phases may appear and disappear in the course of a simulation. In addition, VOCs may be adsorbed by the porous medium, and may biodegrade according to a simple half-life model. TMVOC is implemented as a specialized module in the framework of the general multipurpose simulator TOUGH2, and it retains the general process capabilities and user features of TOUGH2 (Pruess et al., 1999).

3.1.2. *The Existing TOUGHREACT Simulator*

TOUGHREACT (Xu et al., 2006) is a numerical simulation program for chemically reactive nonisothermal flows of multiphase fluids in porous and fractured media. The program was written in Fortran 77 and developed by introducing reactive chemistry into the multiphase fluid and heat flow simulator TOUGH2. A variety of subsurface thermo-physical-chemical-biological processes are considered under a wide range of conditions of pressure, temperature, water saturation, ionic strength, and pH and Eh. Reactions among aqueous species and interactions between mineral assemblages and fluids can occur under local equilibrium or via kinetically controlled rates. The gas phase can be chemically active. Precipitation and dissolution reactions can change formation porosity and permeability. Intra-aqueous kinetics, biodegradation, and surface complexation have recently been incorporated (Xu and Pruess, 2008; Zheng et al., 2009). The program can be applied to one-, two- or three-dimensional porous and fractured media with physical and chemical heterogeneity. It can accommodate any number of chemical species present in liquid, gas and solid phases. TOUGHREACT can be applied to many geologic systems and environmental problems, including subsurface storage of nuclear waste and CO_2, geothermal systems, diagenetic and weathering processes, acid mine drainage remediation, contaminant transport, and groundwater quality. The methods and approaches used in TOUGHREACT have been extensively published over the last decade (Spycher et al., 2003; Sonnenthal et al., 2005; Xu et al., 2006 and 2010; Xu and Pruess, 2008; and Zheng et al., 2009).

3.1.3. *The New TMVOC_REACT Simulator*

TMVOC was initially linked to TOUGHREACT in 2007 (unpublished) by replacing the fluid and heat flow part, TOUGH2 V2, in TOUGHREACT with TMVOC. Gas partial pressures and fugacity coefficients computed from the flow module (TMVOC) are passed to the geochemical module (-REACT) for calculating dissolved concentrations in water. The routine GASEOS (Reagan and Oldenburg, 2006; Moridis et al., 2008) was also incorporated into TMVOC_REACT for computation of gas-phase properties and fugacity coefficients in gas mixtures. This routine incorporates several standard cubic equations of state such as Redlich-Kwong (RK), Peng-Robinson (PR), and Soave-Redlich-Kwong (SRK) (e.g., Orbey and Sandler, 1998). Consumption or production of components from the solid phase is coupled back to fluid flow, but lagging one time step to avoid time-consuming computation of partial derivatives (explicit coupling). This approach preserves the accuracy of mass balances and is accurate enough for most simulated problems. Changes in porosity and permeability due to mineral dissolution/precipitation computed by the chemical module are fed back to the flow module for next-time-step calculations (explicit as well). Once again, this explicit approach preserves the accuracy of mass balances and is accurate for most problems.

The first version of TMVOC_REACT was applied to a project sponsored by Japan Taisei Corporation, for the degassing and induced geochemical changes around Excavated Drifts at Horonobe Underground Research Laboratory (not reported publicly). In the simulation, water-gas-rock interaction and transport processes of three gas components

(CO_2, CH_4, and O_2), a number of aqueous species (such as H_2O, H^+, Na^+, K^+, Ca^{2+}, Mg^{2+}, Cl^-, HCO_3^-, SO_4^{2-}, and $Fe^{2+/3+}$), and minerals (such as amorphous silica, cristobalite, siderite, pyrite, calcite, and gypsum) were considered. Simulations included the degassing of CH_4 and CO_2 from surrounding groundwater in the sediment basin, as well as the diffusion of O_2 from shaft walls during shaft excavations, together with geochemical changes occurring in the aqueous phase as well as mineral dissolution and precipitation.

The initial version of TMVOC_REACT was further enhanced and tested to accommodate the specific requirements of this project. These additional enhancements are described in Sections 3.2 and 3.3 below.

3.2. Partitioning of Benzene between CO_2 and Water

For this report, benzene was selected as an organic compound likely to be present in deep aquifers and likely to be mobilized by supercritical CO_2 (SCC) (Section 4.2). Computing the potential mobilization of benzene by SCC requires computing the partitioning of benzene between SCC, solids and water. TMVOC_REACT was therefore expanded to incorporate such phase-partitioning capabilities.

The solubility of benzene in SCC (or compressed "gas" phase) is implemented by the equation of state for gas-mixtures (GASEOS) incorporated into TMVOC_REACT, making use of fundamental "critical" properties (i.e., critical pressure, critical temperature) and mixture-specific binary interaction parameters. Here, the Soave-Redlich-Kwong option of GASEOS is used, with binary interaction parameters for benzene and CO_2 from Kim et al. (1986). The solubility of benzene and CO_2 in water (or brine), on the other hand, is treated with pressure and temperature-dependent equilibrium constants (similar to Henry's coefficients) that rely on experimental data. For CO_2, aqueous solubilities rely on the solubility model of Spycher and Pruess (2005) (see Appendix A, Section A.1). For benzene, aqueous solubilities are derived using various published data as described in Appendix A, Sections A.2 and A.3. The partitioning of benzene between SCC and water is then directly derived from the computed solubilities of benzene in SCC and water.

To validate the benzene phase-partitioning calculations, an extensive literature search for phase equilibrium data on benzene+SCC+water mixtures was conducted. Unfortunately, these data are scarce. However, phase equilibrium data from binary systems of CO_2+benzene, benzene+water and CO_2+water have been extensively reported. For this reason, the simulator was first tested against data for the binary systems (Appendix A, Sections A.1-A.4), then against a few data available for the ternary system benzene+CO_2+water (Appendix A, Section A.5).

3.3. Calculating the Phase Behavior of the $H_2S + CO_2 + H_2O$ System

In Section 5, TMVOC_REACT is applied to investigate the co-injection of CO_2 and H_2S and transport of these gases along leakage pathways. To do so, the simulator must consider mutual solubilities in the CO_2-H_2S-H_2O system. As in the case of benzene-CO_2-H_2O mixtures (Section 3.2), the simulator relies on the GASEOS routine to compute gas-phase properties and fugacity coefficients for the CO_2-H_2S-H_2O system. The Soave-Redlich-Kwong option of GASEOS was used, with binary interaction parameters for H_2S and CO_2 from Walas (1985). The solubility of these gases in water are computed using equilibrium constants (i.e., Henry's law at infinite dilution) and activity coefficients using data from Spycher and Pruess (2005) for CO_2 and Duan et al. (2007) for H_2S.

To validate the phase-partitioning calculations in the H_2S-CO_2-H_2O system, model results were tested against various published data obtained for the binary systems H_2S+H_2O, CO_2+H_2O, and H_2S+CO_2. Phase-partitioning data for these systems and verification of computed mutual solubilities are provided in Appendix A, Sections A.1 and A.6. Unfortunately, no experimental data were found to directly validate the ternary system.

4. Mobilization and Transport of Organics

The solvent properties of SCC for organic compounds have long been recognized and are one of the reasons CO_2 flooding of hydrocarbon reservoirs has been practiced for years to enhance oil recovery (e.g. Bondor, 1992). SCC has also been lauded as an environmentally friendly solvent, and its use to decontaminate soils impacted by hazardous organic compound is regarded as a "green" cleanup technology (e.g., Anitescu and Tavlarides, 2006; Green and Akgerman, 1996; Hauthal, 2001; Smyth et al., 1999) because it avoids the use of other more hazardous solvents. Given these considerations, there are good reasons to evaluate the potential for mobilization of organics from deep storage reservoirs to overlying freshwater aquifers upon leakage from CCS operations. Therefore, TMVOC_REACT was used to assess the potential for SCC to (1) mobilize and transport organic compounds in deep geologic formations and (2) possibly contaminate potable groundwater if leakage occurred from depth into an overlying fresh water aquifer.

Section 4.1 describes the relevant processes at play and provides the conceptual understanding of the hypothetical simulation scenarios being considered. In Section 4.2, data on the occurrence of hazardous organic compounds in deep aquifers are reviewed. Several compounds of potential interest are identified, and a rationale is presented for selecting one of these compounds for further study by numerical modeling (benzene). Finally, simulations of a hypothetical CO_2 injection and leakage scenario, including mobilization of the selected organic compound (benzene), are presented in Section 4.3.

It should be noted that the inclusion of other organic compounds and/or mixtures of such compounds was not considered in these simulations. This is primarily because the calculation and validation of necessary thermodynamic data (including partition coefficients and mutual solubility data) against results of experimental studies for more than one compound was beyond the scope of this study.

Because organic compounds are likely to be associated with solid phases in deep saline aquifers (e.g., in kerogen and/or sorbed on surfaces of minerals, rather than in a residual oil phase), the assessment of organic compound mobilization and transport by SCC in deep aquifers also requires knowledge of the nature of phases associated with organics, as well as sediment sorption characteristics for these compounds. These properties are not only quite site specific, they are also mostly unknown. Therefore, any exploratory, generic, modeling, as done here, must rely on assumptions that are approximate at best, yielding results that should be regarded as more qualitative than quantitative, and highly dependent on those assumptions. For these reasons, the modeling goal is more to demonstrate simulation capabilities and processes at play than providing actual predictions for any particular system.

4.1. Relevant Processes and Conceptual Mobilization Scenario

The scenario being considered in our modeling study is that of injected SCC into a deep saline aquifer, mobilizing organic compounds potentially present in the storage formation. Because SCC is less dense than water, some SCC migration is expected upward along the dip of the storage formation, up to a point when the SCC plume would become immobilized by a structural trap (e.g., low-permeability/porosity cap rock) and/or by capillary trapping as the SCC liquid saturation drops below the threshold residual saturation (e.g., Doughty and Pruess, 2005; Silin et al., 2009). Because SCC is a well-known solvent for organics (e.g., Anitescu and Talvarides 2006), it is expected to dissolve organic compounds present in the storage formation and, to some extent, transport these compounds within the confined CO_2 reservoir. The main question being evaluated here is the extent of such mobilization in the event of leakage from the reservoir to shallower formations, for example through fault or fracture zones, or poorly plugged abandoned wells.

The mutual solubilities of the various phases involved, and their variation with temperature and pressure, are critical to evaluating the mobilization of organics and their transport by SCC. It is expected that organics remain preferentially soluble in SCC (relative to water) along the leakage flow path. If the aqueous solubility of an organic species migrating with SCC was higher than the aqueous solubility of CO_2, potential enrichment of organics in SCC could occur along the flow path. This is the case, for example, with benzene, which was selected for our modeling study (Section 4.2).

Given the large model and parameter uncertainties, our modeling study uses a relatively simple conceptual model setup in one and two dimensions. As discussed in more detail in Section 4.3, 1-D simulations are run to evaluate the mobilization and transport of one organic compound (benzene) within the storage formation. The benzene is assumed to originate from kerogen, with initial amounts estimated from limited data available for various deep aquifers. A 2-D model is then used to evaluate the transport of benzene in SCC from a deep reservoir to a shallower aquifer. In this case, benzene is leached at depth by SCC and subsequently transported along a vertical leakage pathway to a shallow water aquifer. No partitioning (sorption) in the solid phase is assumed to take place along the leakage pathway and in the shallow aquifer, thus maximizing aqueous concentrations. The pressure and temperature path followed along the vertical pathway are controlled by hydrostatic pressure and a typical geothermal gradient. It should be noted that code capabilities presently do not allow "flashing" from liquid CO_2 to gaseous CO_2 conditions. For this reason, pressure and temperature, although decreasing along the leakage pathway, are kept within the supercritical domain.

4.2. Organics of Concern, Properties, and Selection of Key Compound

The risk from potential mobilization of organic compounds by SCC can be evaluated using the following criteria:

- High probability of occurrence/abundance in deep storage formations
- Likely mobilization by SCC (determined by the solubility in CO_2, and partition coefficient between CO_2 and water, and partition coefficient between sediments and water)

- Significant solubility in water at conditions representing freshwater resources
- Significant environmental hazard (high toxicity)

Although the organic compounds present in deep saline aquifers are seldom reported, their composition in waters produced from oil fields have been extensively studied (e.g., RøeUtvik, 1999; Witter and Jones, 1999). RøeUtvik (1999) reviewed the chemical characteristics of produced water from fields in the North Sea, the Gulf of Mexico, and the coast of Canada, and indicated that dissolved hydrocarbons are dominated by benzene, toluene, ethylbenzene, and xylenes (BTEX). Also commonly found are polycyclic aromatic hydrocarbons (PAHs) and phenols. Table 4.1 shows some reported concentration of these compounds in production waters. Although other organic compounds have also been reported, BTEX, PAHs, and phenols appear to be most commonly reported. These compounds are toxic, as reflected by their low regulatory maximum contaminant levels (MCL). PAHs, which typically occur at small concentrations in produced water (Table 4.1), have the lowest MCL (i.e., are the most toxic).

Because the sediments of many deep saline aquifers typically undergo a burial and diagenesis history similar to that of oil field reservoirs, it is anticipated that organic compounds present in deep saline aquifers would be similar to those reported in oil-field brines, although occurring at much lower concentrations. For these reasons, and because of the toxicity of these compounds, BTEX, PAHs, and phenols are considered key candidates for further evaluation of potential mobilization by SCC. Obviously, many other organics could warrant attention. Such compounds include carboxylic acids, which are commonly present at much higher concentrations (up to 5,000 mg/L) in oil field brines (Kharaka and Hanor, 2007) and are also expected in deep saline aquifers. Although these compounds are essentially nontoxic, they are good ligands for metal complexation, and their mobilization could exacerbate the release of trace metals upon an SCC leakage into fresh water. However, in this limited study, focus on a few key toxic organic compounds was given first priority, keeping in mind that further study of other compounds should not be ruled out.

Table 4.1. Some reported BTEX, PAHs, and phenols concentration (mg/L) in production waters

	RøeUtvik (1999)	**Witter and Jones (1999)**	**Kharaka and Hanor (2007)**
BTEX	2.4-9.0	0.005-3.4	Up to 60
PAHs	0.93-1.6	Not reported	up to 10
Phenols	0.58-11.45	0.2-5.4	Up to 20

Table 4.2. MCLs for benzene, benzo(a)pyrene (a common PAH compound), and some phenols.

Organic compound	**MCL[1] (mg/L)**
Benzene	0.005
Benzo(a)pyrene	0.0002
Pentachlorophenol	0.001
Phenol	0.004[2]

[1] U.S. EPA Maximum Contaminant Level, unless indicated otherwise

[2] Canadian Environmental Quality Guidelines for the Protection of Aquatic Life (1999)

When considering the risk of groundwater contamination, we must consider the aqueous solubility of organic compounds of potential concern, in addition to their MCLs. PAHs, for example, have extremely low aqueous solubilities, whereas the solubility of benzene or phenol is much higher, as shown in Table 4.3. The very high solubility of phenol in water reflects the fact that phenol is hydrophilic, whereas benzene is hydrophobic. Obviously, the solubility of these compounds in SCC is also a critical property for evaluating their mobilization/transport by SCC. Benzene and PAH solubilities in SCC are also shown in Table 4.3, for conditions typical of CCS operations.

Based on their low solubility in SCC and water, it was decided not to consider PAHs further in this study, leaving benzene and phenol for further consideration. Additional data on the partitioning of benzene and phenol with SCC and SCC-water mixtures are presented below to help evaluate which of these two compounds should be retained for further evaluation in hypothetical leak scenarios.

At 373.15 K, benzene becomes completely miscible with carbon dioxide at 13–14 MPa, whereas phenol remains immiscible with SCC up to pressures as high as 30 MPa (Pfohl et al., 1997). The lower pressure and temperature requirement for full miscibility of benzene with SCC indicates that benzene may be a better candidate for further consideration. A literature search was conducted for additional solubility data for benzene and phenol in SCC at comparable temperatures and pressure. However, reported P-T ranges for benzene+CO_2 and phenol+CO_2 mixtures seldom overlap. Figures 4.1 through 4.3 show the measured solubility of benzene/phenol in supercritical CO_2 at 40°C, 60°C, and 100°C. At 40°C, Ohgaki and Katayama (1976) and Gupta et al. (1982) measured the solubility of benzene in CO_2 at pressure below 77 bar, while Van Leer and Paulaitis (1980) measured the solubility of phenol in CO_2 at pressure above 79 bar. At 77–79 bar, the solubility of these two compounds differ by a factor of 3 to 5, with benzene being more soluble.

Table 4.3. Comparison of solublities of benzene and some PAHs in supercritical CO_2 (400 bar and 50°C) and ambient water (25°C, 1 bar) unless shown otherwise

Compounds	Solubility in SCC (g/kg)	Solubility in water (g/kg)
benzene	miscible	1.8
phenol	~95[a]	82000[b]
naphthalene	120	3.2×10^{-4}
phenanthrene	11	1.3×10^{-3}
pyrene	1.2	1.4×10^{-4}
chrysene	0.02	2×10^{-6}
perylene	0.005	4×10^{-7}
benzo[a]perylene	0.002	3×10^{-7}

[a]Phenol solubility in SCC is from Van Leer and Paulaitis (1980) at 60°C and ~240 bar. [b]Phenol aqueous solubility is from Poling (2007). Other data are from (Hawthorne and Miller, 2003), adapted from Bartle et al. (1991), Miller et al. (1996), and Mackay and Shiu (1977).

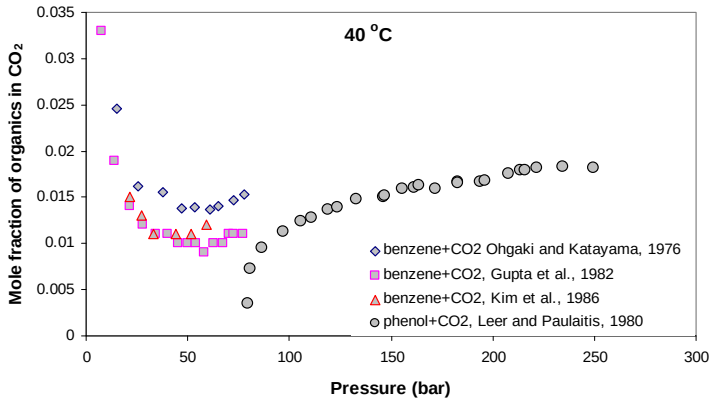

Figure 4.1. Solubility of benzene/phenol in SCC at 40°C as a function of pressure. The solubilities of benzene in SCC are taken from Ohgaki and Katayama (1976), Gupta et al. (1982), Kim et al. (1986) while those for phenol are from Leer and Paulaitis (1980).

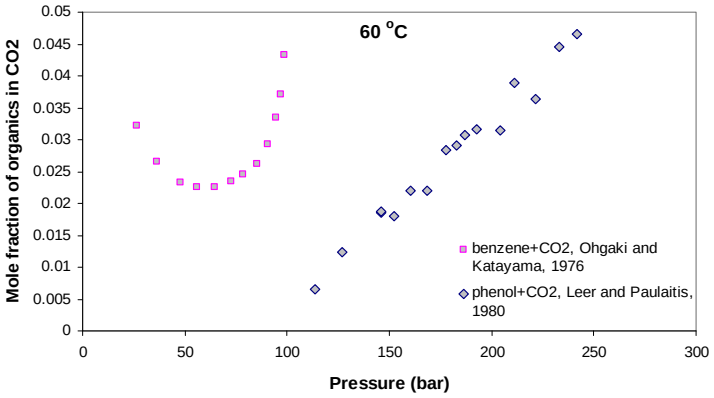

Figure 4.2. Solubility of benzene/phenol in SCC at 60°C as a function of pressure. The solubilities of benzene in SCC are taken from Ohgaki and Katayama (1976), while those for phenol are from Van Leer and Paulaitis (1980).

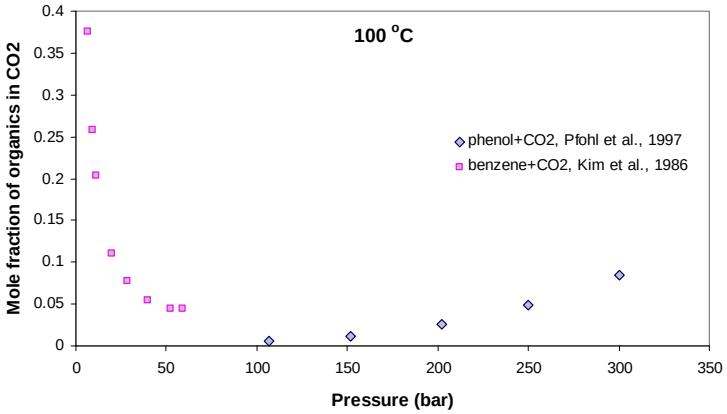

Figure 4.3. Solubility of benzene/phenol in SCC at 100°C as a function of pressure. The solubilities of benzene in SCC are taken from Kim et al. (1986), while those for phenol are from Pfohl et al. (1997).

Table 4.4. Published partition coefficients of phenol between CO_2 and water.

Temperature (K)	Pressure (bar)	K_i	Reference:
308	131	0.83	(Green and Akgerman, 1996)
308	145	0.96	
308	190	1.25	
308	197	1.03	
318	128	0.91	
318	152	1.06	
318	193	1.08	
318	221	1.19	
313	81	0.56	(Brudi et al., 1996)
313	104	0.87	
313	158	0.99	
313	203	1.03	
313	255	1.04	
313	8.3	0.22	
313	10.4	0.43	
313	15.1	0.88	
313	20.1	1.07	
313	25.0	1.21	
313	30.0	1.30	
333	8.0	0.31	
333	10.5	0.22	
333	15.2	0.74	
333	20.0	1.02	
333	24.9	1.25	
333	30.0	1.39	
313	96.5	0.46	(Ghonasgi et al., 1991)
313	110.25	1.12	
313	124.04	1.27	
313	155.1	1.54	
313	172.3	1.73	
323	96.5	0.34	
323	110.25	0.36	
323	124.04	0.77	
323	155.1	1.31	
323	172.3	1.66	

The partitioning of benzene and PAH's in SCC+water mixtures must also be evaluated. For this purpose, the partition coefficient *K* can be defined as the ratio of the mole fraction of an organic compound in CO_2 to the mole fraction of that compound in water (Green and Akgerman, 1996). The SCC-H_2O partition coefficient for benzene ranges from 1000 to 4000 (Ghonasgi et al., 1991) (see Appendix A, Sections A.2-A.4). The partition coefficient of phenol, as shown in Table 4.4, is much lower. This is expected because benzene displays a higher solubility in SCC and lower solubility in water compared to phenol. These data suggest that benzene is more prone to extraction/mobilization by SCC than phenols.

Given the review of these data, benzene was selected for further investigation in this study because of: (1) its relatively low MCL (similar to phenol but higher than PAH), (2) its high solubility in SCC (3-5 times higher than phenol and 2-5 orders of magnitude higher than PAHs), (3) its relatively high solubility in water (lower than phenol but higher than PAHs), and (4) its high partition coefficient between SCC and water.

4.3. Mobilization of Benzene by Supercritical CO_2 in a Deep Saline Formation

This section starts with a discussion of the possible inventory of benzene in deep saline formations, both in the aqueous and solid phases. Results of a 1-D model are presented in Section 4.3.4. This model aims at testing the ability of the code to simulate the leaching of benzene by SCC in a deep storage formation, and at identifying the key chemical and transport processes affecting the mobilization. Finally, a 2-D model is presented, simulating the mobilization of benzene by SCC from a deep storage formation and its migration via a leakage pathway to an overlying aquifer.

4.3.1. *Benzene Content in Aqueous and Solid Phases in Deep Saline Aquifers*

Benzene in the subsurface is usually associated with gasoline contamination and/or the presence of oil (Slaine and Barker, 1990). Benzene concentrations in water produced from oil fields have been extensively reported (RøeUtvik, 1999; Witter and Jones, 1999), in some cases with BTEX concentrations as high as 60 mg/L (Kharaka and Hanor, 2007). Usually, the concentrations of hydrocarbons such as benzene dissolved in oil field brines have been studied with the objectives of (1) determining if the hydrocarbon content of the sampled brine can be used to determine whether an exploratory well is close to a petroleum accumulation, and (2) providing information to help answer more fundamental questions concerning the origin, migration, and accumulation of petroleum (McAuliffe, 1969). It has been found that the concentrations of dissolved hydrocarbons increase with depth (Buckley et al., 1958) and decrease with the distance from a petroleum reservoir (Zarrella et al., 1967). McAuliffe (1969) analyzed the dissolved hydrocarbon content of typical subsurface brines recovered by conventional drill-stem tests in exploratory wells (though the location of these wells is not indicated in the paper), revealing a wide range of values, from 0.86×10^{-3} to 8.65 mg/L.

The study by Zarrella et al. (1967) provides additional data to evaluate the range of benzene concentration in oil field brines (Tables 4.5, 4.6 and 4.7). These authors investigated the concentration of benzene in formation brines from development and wildcat wells at various distances from petroleum reservoirs and at various depths, covering barren and producing horizons. Their study shows that benzene concentrations decrease away from reservoirs (Table 4.6), and away from producing horizons (Table 4.7). These authors also observed that brine from a unit separated by only 90 ft of shale from an oil pool contained only traces (less than 0.02 ppm) of benzene. Sirivedhin and Dallbauman (2004) confirmed this observation in a study of benzene concentration from the Osage-Skiatook Petroleum Environmental Research site, Osage County, Oklahoma. In their study, the maximum concentration of benzene in produced water was found to be

0.53 mg/L, whereas the concentration of benzene in shallow groundwater above the production zone was only 0.001 mg/L.

Table 4.5. Benzene content of brines co-produced with crude oil (Zarrella et al., 1967)

Field	Area	Formation	Type of Production	Benzene Content of Brine (ppm)
1. Gwinville	Mississippi	Eagle Ford	Condensate	18.6
2. Bough	Lea Co., New Mexico	Pennsylvanian	Crude oil	10.7
3. Golden Spike	Alberta, Canada	Basal Quartz	Crude oil	7.1
4. Lampman	Saskatchewan, Can.	Frobisher-Alida	Crude oil	7.0
5. Keystone	Crane Co., Texas	Holt	Crude oil	5.6 - 4.7
6. Stettler	Alberta, Canada	Leduc	Crude oil	6.0 - 4.8
7. Stettler	Alberta, Canada	Nisku	Crude oil	6.0 - 4.9
8. Darst Cr.	Texas	Edwards Ls.	Crude oil	0.21
9. Braeburn	Alberta, Canada	Permo Penn	Gas	0.0
10. Hereford	Alberta, Canada	Viking	Gas	0.0

Table 4.6. Variation of benzene concentrations in formation brines with distance from production (Zarrella et al., 1967).

Area	Formation	Benzene Content of Brine (ppm)	Distance to production in equivalent zone (miles)
1. New Mexico	Pennsylvanian	10.7 6.5	0 2
2. Saskatchewan, Canada	Frobisher-Alida	7.0 4.5 3.4 2.2 1.6 1.0	0 1 ¾ 1 ¾ 1 ½ 5 ½
3. Alberta, Canada	Leduc	6.0 - 4.8 3.4 2.2 1.8 1.6	0 ½ 1 ½ 2 ¾ 2 ¾
4. West Texas	Wolfcamp	2.5 1.2 1.3 0.9 0.0	0 ¾ 2 ½ 5 16

Table 4.7. Benzene content in brines from wells in multiple test zones (Zarrella et al., 1967).

Area	Interval Tested (ft)	Formation	Benzene Content of Brine (ppm)	Distance to production in equivalent zone (miles)
1. Saskatchewan	2950-2980	Viking	0.0	None
	3265-3436	Blairmore	0.0	None
	3415-3436	Blairmore	0.0	None
	3510-3530	Blairmore	0.0	None
	3858-3875	Jurassic	0.0	None
	3993-4002	Jurassic	0.0	None
	4645-4655	Frobisher-Aldia	(oil)	0 mile
2. Saskatchewan	2929-2969	Blairmore	0.0	None
	3649-3685	U. Shaunavon	0.0	None
	3739-3760	L. Shaunavon	0.0	None
	4220-4230	Frobisher-Alida	(oil)	0 mile
3. Saskatchewan	4419-4459	Midale	6.8	½ mile
	4490-4502	Frobisher-Alida	trace	

Based on these investigations, and the fact that this modeling study considers CO_2 injection into a deep saline formation that is not in the vicinity of an oil reservoir, an initial benzene concentration of 0.001 mg/L is assumed in the target aquifer. This value is higher than most observed concentrations in deep saline aquifers. Most injection targets are in sedimentary basins where oil and gas fields (some may be depleted) are present in the vicinity, so the value of 0.001 mg/L is conservatively quite low with respect to computed amounts of benzene potentially mobilized by SCC. Note that this value is 5 times smaller than the EPA-regulated Maximum Contaminant Level for benzene (0.005 mg/L, 5 ppb) in drinking water.

Other important parameters constraining the total amount of benzene that could be leached from a storage formation are the amount of organic matter in the sediments, and the amount of benzene associated with the organic matter. Kraemer and Reid (1984) mentioned that the bulk of organic matter in Gulf Coast sediments is contained within shale in generally low amounts (0.31–1.0 wt.% total organic carbon). Organic matter in sandstones is typically much less. In the current study, we conservatively assume that the deep saline aquifer is an impure sandstone containing 1.0 wt.% of organic matter as a generic "kerogen" phase. The amount of benzene in the kerogen is assumed to be 0.01 ppm, which corresponds to 1×10^{-4} ppm benzene in the sediment.

4.3.2. *Release of Benzene from Sediments*

Mobilization of benzene by SCC in a deep saline aquifer involves not only the partition of benzene between aqueous and CO_2 phases, but also the mass transfer of benzene between the solid and the aqueous phase. As discussed in the previous section, benzene is

assumed to be associated with solid organic matter, which could be viewed as some kind of a generic "kerogen" phase. This phase is treated in the model like a mineral, allowed to dissolve at a certain rate to mimic the decomposition (or maturation) of kerogen. This dissolution rate is so slow, however (e.g., Freund and Kelemen, 1989) that benzene release from actual decomposition of kerogen is not considered further. Instead, it is assumed that benzene is associated with the "kerogen" phase via sorption, which is computed using a coefficient expressing the distribution of benzene between the aqueous and a solid "kerogen" phase. The estimation of this distribution coefficient for implementation into the numerical model is presented in Appendix A, Section A.8.

4.3.3. *1-D Model*

A 1-D model is established to evaluate the mobilization of benzene by SCC in a deep saline aquifer, from an area where the sediments contain benzene, to a downstream region that is initially benzene free. The objective of these simulations is to test the code's capability to simulate the transport of organic compounds, and to identify the transport and chemical processes that control the mobilization of benzene by CO_2.

4.3.3.1. Model Setup

Figure 4.4 shows the setup of the 1-D model. The simulation domain is 100 m long and evenly discretized into 50 gridblocks. Each gridblock has a volume of 40 m^3. The gridblock on the right boundary is assigned a large volume representing a fixed boundary condition.

Benzene is present in the sediments within the first five gridblocks, and the initial concentration of benzene therein is 1.28×10^{-8} molal (~0.001 mg/L) (see Figure 4.5). CO_2 is injected into the gridblock on the left boundary. The injection rate is 5×10^{-4} kg/s.

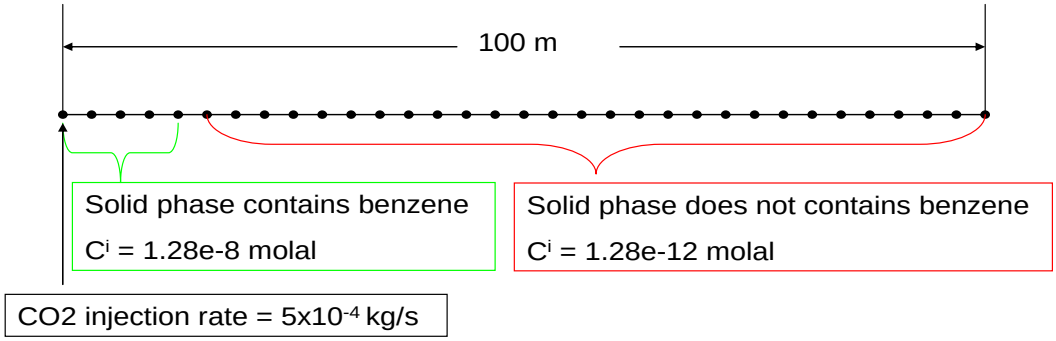

Figure 4.4. Schematic representation of 1-D model, not to scale.

The simulation is conducted for 10 years. Initial pressure is 200 bar and initial temperature is 75°C, uniformly distributed over the entire simulation domain. Therefore, the injected CO_2 is in the supercritical phase. No CO_2 is present initially at time = 0. The simulation is isothermal.

4.3.3.2. Numerical Experiment Excluding SCC-Benzene Phase Partitioning

The processes that control the transport of benzene in SCC and in the aqueous phase include the partitioning of benzene between the sediments, SCC, and water; advection of SCC; the displacement of the aqueous phase by SCC; and advection and diffusion of both CO_2 and benzene in the aqueous phase. To better understand the leaching of benzene by SCC, we ran a numerical experiment in which the partitioning of benzene between SCC and water is turned off (i.e., SCC does not extract benzene from the aqueous phase, serving only as a fluid that displaces the aqueous solution). As soon as CO_2 is injected at the left boundary, a two-phase zone (SCC and water) develops and gradually expands towards the right model boundary (Figure 4.5). The two-phase zone develops starting in the area where benzene is initially present. As a result, benzene-bearing water is displaced towards the right boundary by the injected CO_2 (Figure 4.6).

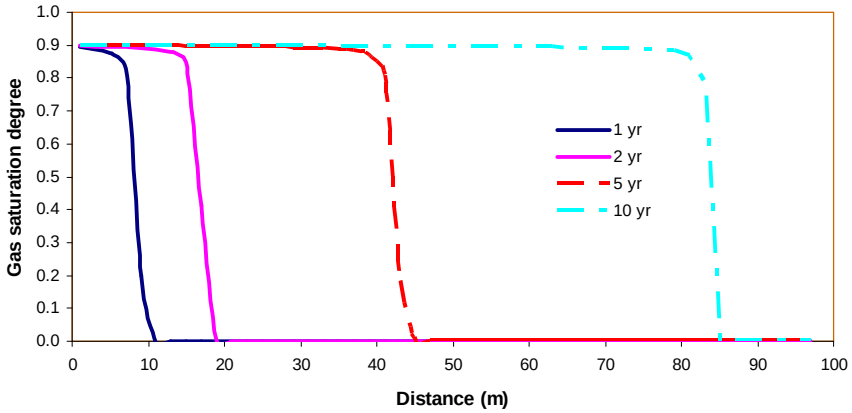

Figure 4.5. Computed distribution of SCC "liquid" saturation as a function of distance at different times, for a case when the partitioning of benzene into SCC is suppressed.

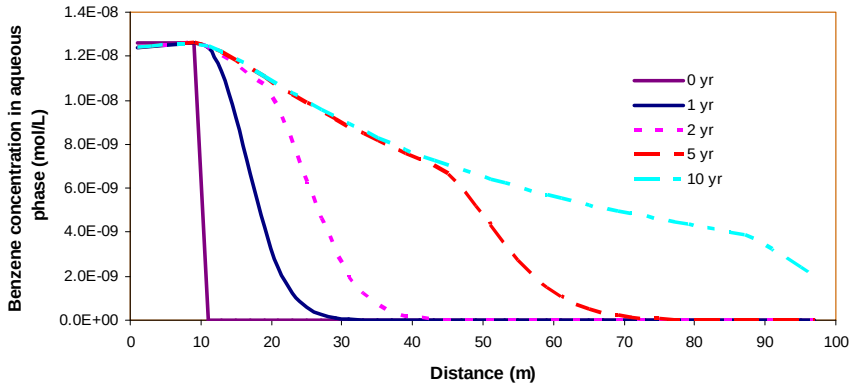

Figure 4.6. Computed benzene concentration in the aqueous phase as a function of distance at different times, for a case when the partitioning of benzene into SCC is suppressed.

4.3.3.3. Base-Case Model Including SCC-Benzene Phase Partitioning

Benzene is initially present in the system as a compound dissolved into the aqueous phase and sorbed onto organic matter (kerogen) in the sediments. The mass of benzene associated with the sediments (solid-phase benzene) accounts for a dominant portion of the total benzene mass. The injection of CO_2 into the aquifer initiates a redistribution of benzene between the different phases. Figure 4.7 shows the time evolution of benzene mass in SCC, the aqueous phase, and in the sediments expressed as a ratio of "total mass". Initially, adsorbed benzene accounts for 47% of the total benzene mass, whereas benzene in the aqueous phase accounts for the remaining 53%. The appearance of CO_2 leads to preferential partitioning of benzene into the CO_2 phase, which reduces the aqueous benzene concentration and also releases benzene from the solid phase. As a result, solid-phase benzene is soon depleted. The proportion of benzene total mass in SCC gradually increases to about 90% after 10 years.

Figure 4.8 shows the spatial distribution of benzene mass in the SCC phase. Benzene is extracted from the aqueous and solid phases in the left side of the domain. The front tip of the SCC plume displays the highest mass fraction of benzene. As the SCC front moves out of the area initially containing benzene, the mass fraction of benzene in SCC decreases gradually, even as the total mass of benzene in SCC increases.

Figure 4.9 shows the spatial distribution of benzene concentration in the aqueous phase. CO_2 displaces the aqueous solution and pushes it downstream towards the right boundary. CO_2 extracts benzene from the aqueous phase and thereby strongly reduces the initial aqueous concentration in the left side of the domain. The interplay of these two processes, together with diffusion in the aqueous phase, leads to a bell-shaped spatial distribution. The peak concentration of aqueous benzene occurs in the single-phase zone.

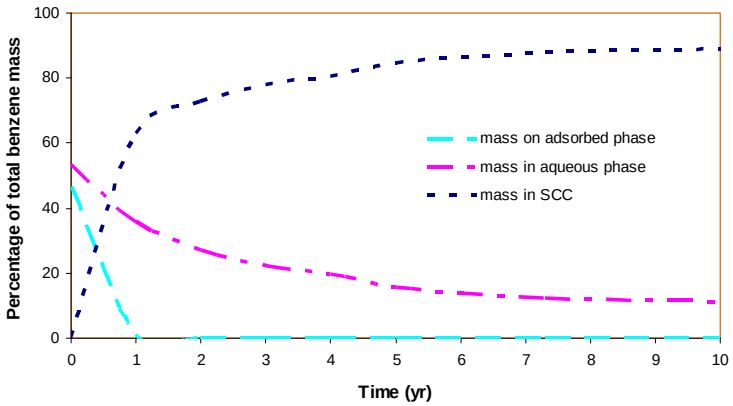

Figure 4.7. Computed time evolution of benzene mass distribution in water (aqueous), SCC ("gas" phase) and sediments (adsorbed phase), as a percentage of total benzene mass.

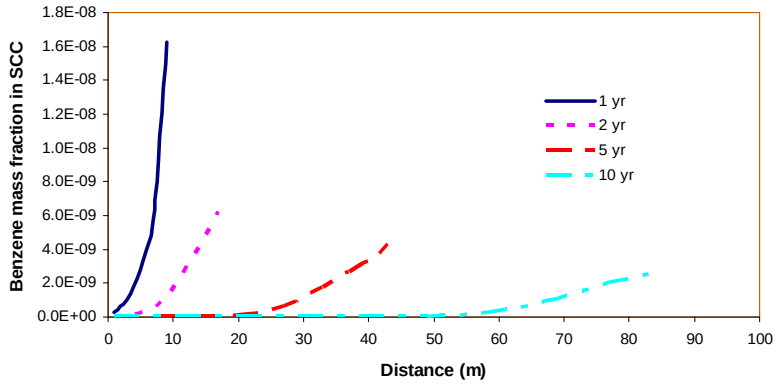

Figure 4.8. Computed mass fraction of benzene in SCC at as a function of distance from the injection point, at different times.

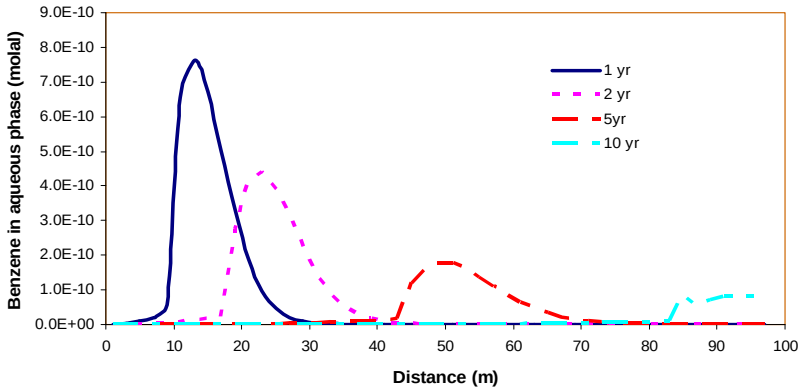

Figure 4.9. Computed benzene concentration profiles in the aqueous phase as a function of distance from the injection point, at different times.

4.3.3.4. Case with Lower Initial Benzene Total Mass

In the base-case model, the total initial amount of solid-phase benzene corresponds to a (sorbed) benzene concentration, initially 1.23×10^{-8} mol/kg$_{water}$ ($\sim1\times10^{-4}$ ppm in the sediments), which accounts for almost half the benzene mass that can be mobilized by CO_2. A sensitivity run is conducted with an initial (sorbed) benzene mass two orders of magnitude smaller. As a result, the mass fraction of benzene in the SCC phase is lower by about 50% (see Figure 4.10), and the benzene concentration in the aqueous phase is slightly reduced (Figure 4.11).

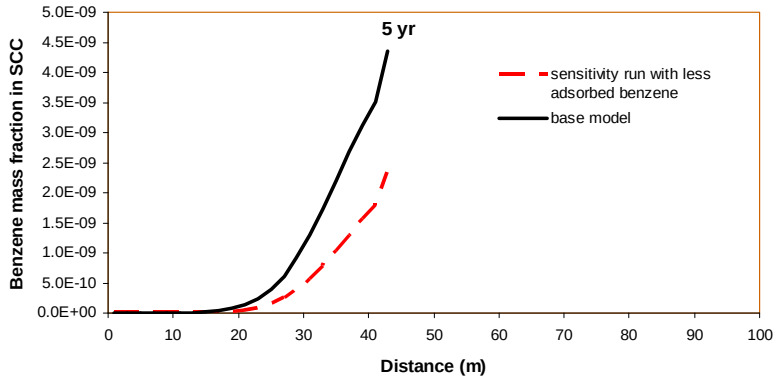

Figure 4.10. Computed mass fraction of benzene in SCC at 5 years, as a function of distance from the injection point: base case and case with smaller initial total benzene mass.

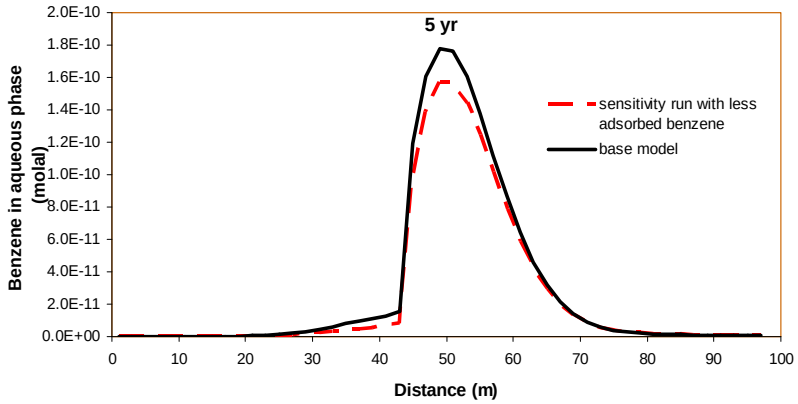

Figure 4.11. Computed benzene concentration profiles in the aqueous phase at 5 years, as a function of distance from the injection point: base case and case with smaller initial total benzene mass.

4.3.3.5. Simulation with Lower Initial Concentration of Aqueous Benzene

As discussed in Section 4.3.2, the concentration of aqueous benzene in a deep saline aquifer is rarely reported unless the aquifer is near an oil field. The research work by Zarrella et al. (1967) indicates that the concentration of aqueous benzene may be very low away from oil-producing zones. In this sensitivity run, we assume that the initial concentration of aqueous benzene is 2.56×10^{-9} molal, five times lower than that in the base-case model. This lower concentration is adopted, keeping the sorption characteristics unchanged for the solid phase (Appendix A, Section A.8). Therefore, with a five-times-lower initial benzene aqueous concentration, the computed amount of sorbed benzene is smaller as well, also by a factor about 5. Figures 4.12 and 4.13 show that under these conditions, the mass fraction of benzene in SCC and the concentrations of aqueous benzene are only about $1/10^{th}$ of those obtained in the base-case simulation.

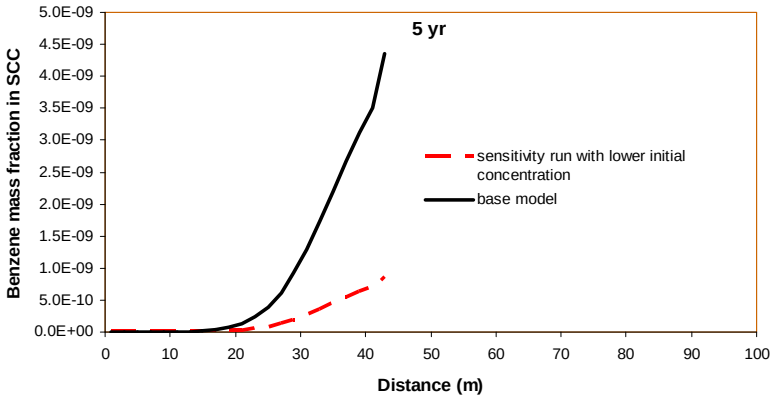

Figure 4.12. Computed mass fraction of benzene in SCC at 5 years, as a function of distance from the injection point: base case and case with 5x smaller initial benzene aqueous concentration.

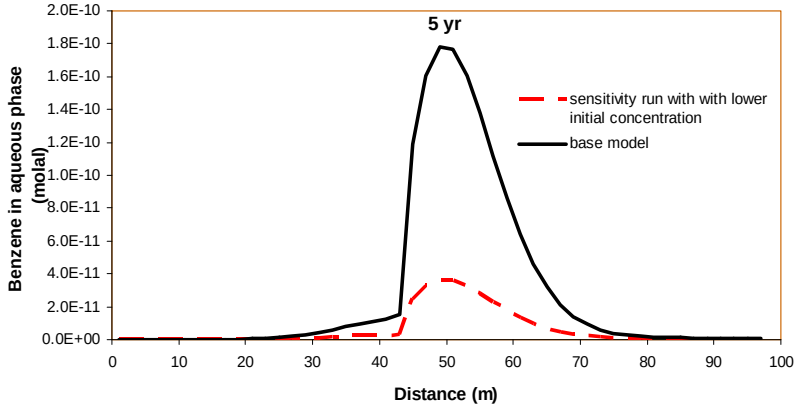

Figure 4.13. Computed benzene concentration profiles in the aqueous phase at 5 years, as a function of distance from the injection point: base case and case with 5x smaller initial aqueous benzene concentration.

4.3.4. *2-D Model*

A 2-D model was set up to investigate the transport of benzene by SCC in the case of hypothetical leakage from a storage formation where benzene is present to an overlying "clean" aquifer via some preferential pathway. The objective, here, is to evaluate, in a semi-quantitative manner, whether benzene in sediments at depth could be leached by SCC, transported through a leakage pathway, then dissolved into an aquifer overlying the storage formation.

4.3.4.1. Model Setup

Figure 4.14 shows a schematic representation of the model setup including initial and boundary conditions, and Figure 4.15 shows the numerical discretization mesh. The 2-D cross section includes a deep storage formation, an overlying aquifer, and a leakage pathway that connects the two aquifers. The leakage pathway is simulated as a zone of high permeability. Aquitards are included in the model between the storage formation

and the overlying aquifer, as well as above this aquifer. Pressures on left and right (vertical) boundaries are fixed. A 1/100 gradient is applied on the flow field with a regional gradient direction from left to right. CO_2 is injected at a rate of 0.1 kg/s (~3.2 kt/y) in a well located 200 m from the left boundary, and perforated through the entire storage formation (with the well modeled as stack of model gridblocks). The bottom of the vertical leakage pathway, which could be a fracture zone or a poorly abandoned well, is located 100 m downgradient of the injection point (300 m from the left model boundary). Hydrostatic pressure conditions are assumed initially for vertical direction. Table 4.8 lists the hydrogeologic properties for the model. The fracture zone is 6 m in width, and given the same properties as the storage formation, except for the permeability, which is one order of magnitude higher.

Table 4.8. Hydrogeologic properties for the base model

Properties	**Values for deep storage formation, overlying aquifer**	**Values for aquitard**
Permeability (m^2)	1.0×10^{-13}	1.0×10^{-19}
Porosity	0.20	0.05
Capillary pressure	Van Genuchten function with m=0.46, $\alpha=5.0\times10^{-5}$	Van Genuchten function with m=0.46, $\alpha=5.0\times10^{-7}$
Relative permeability	Corey's curve with zero residual gas saturation	Corey's curve with zero residual gas saturation
Residual water saturation	0.3	0.3

Figure 4.16 shows the initial (regional) pressure distribution. The pressure at the top of the model domain is around 20 bar, and that at the bottom is about 200 bar. The temperature is 21°C at the top and 75°C at the bottom (see Figure 4.18), assuming a thermal gradient of 30 °C/1000 m.

The total simulated time period is 3.5 years. At this point, the injected CO_2 in the storage formation has migrated into the fracture zone, moved upwards via buoyancy forces and vertical pressure gradient, and spread out within the overlying aquifer, eventually reaching the left boundary of the model domain. When extending the simulation to longer times (up to 6 years), the model results become strongly affected by the conditions assumed at the left model boundary (constant pressure) resulting in underestimated plume size and benzene concentrations in aqueous and SCC phases. Therefore, in the following sections, we concentrate on model results for the first 3.5 years.

As in the 1-D model, the initial benzene concentration in the aqueous phase is assumed to be 1.28×10^{-8} molal (~ 0.001 mg/L) in the storage formation, and is set to a very small number (1.28×10^{-12} molal) in areas outside the storage formation. Solid-phase (sorbed) benzene is only present within the storage formation, at a concentration of 1×10^{-4} ppm in the sediments (and 0.01 ppm in kerogen, using a 1 wt% volume faction of kerogen in sediments). Relative to the amount of water present, this corresponds to a concentration of solid-phase benzene of 1.23×10^{-8} mol/kg_{water}.

The amount of benzene assumed initially present in the storage formation is one of the most critical factors affecting predicted benzene concentrations after transport by SCC to the shallow aquifer. The factors that have been considered when choosing the above values include: (1) CO_2 injection is assumed to occur into a deep saline formation which is not in the vicinity of an oil reservoir, and (2) while considering that our simulation are generic in nature, some measured data for such formations exist and have been used here as reference values in a conservative way (i.e., yielding rather elevated aqueous benzene concentrations). Detailed discussion on how and why we choose the initial benzene concentration in the solid and aqueous phases is given in Section 4.3.1 and 4.3.2.

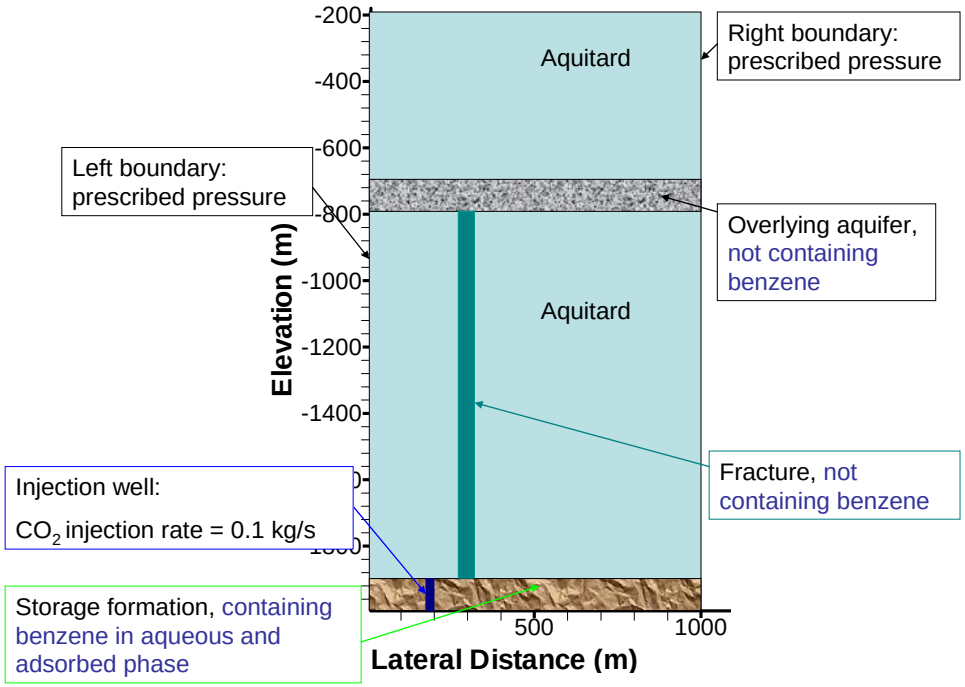

Figure 4.14. Schematic representation of hypothetical 2-D simulation scenario.

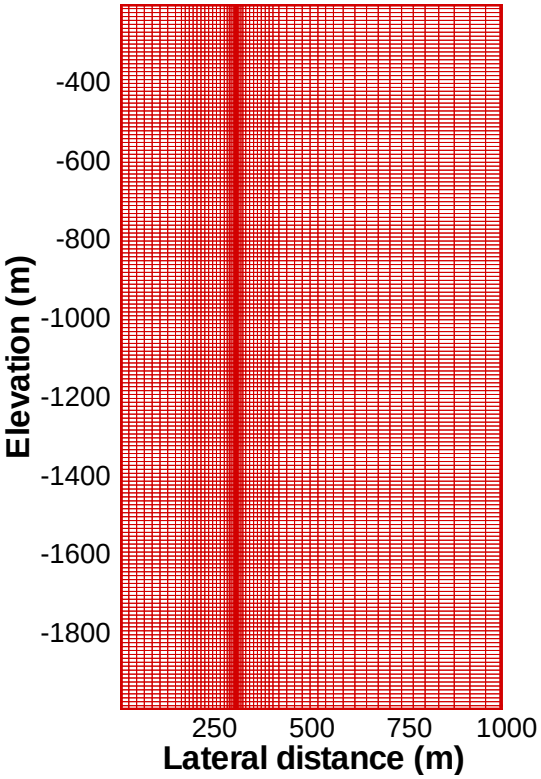

Figure 4.15. Numerical mesh for the vertical 2-D model

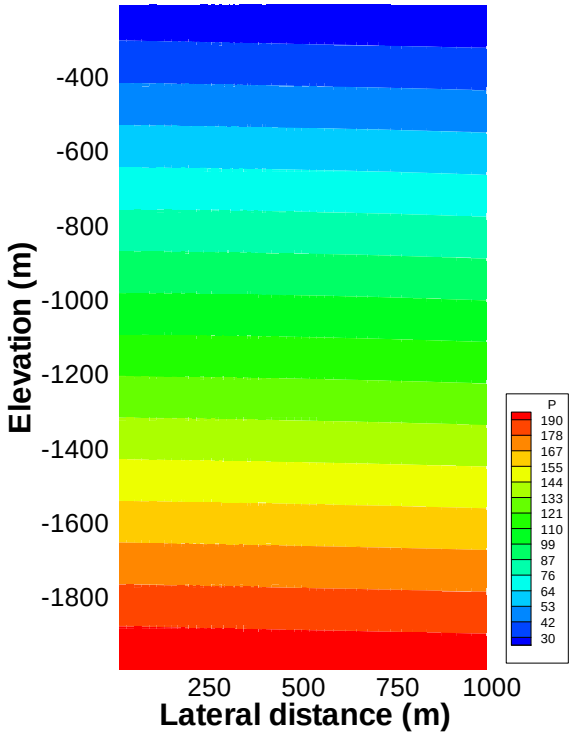

Figure 4.16. Computed initial (regional) pressure distribution (bar).

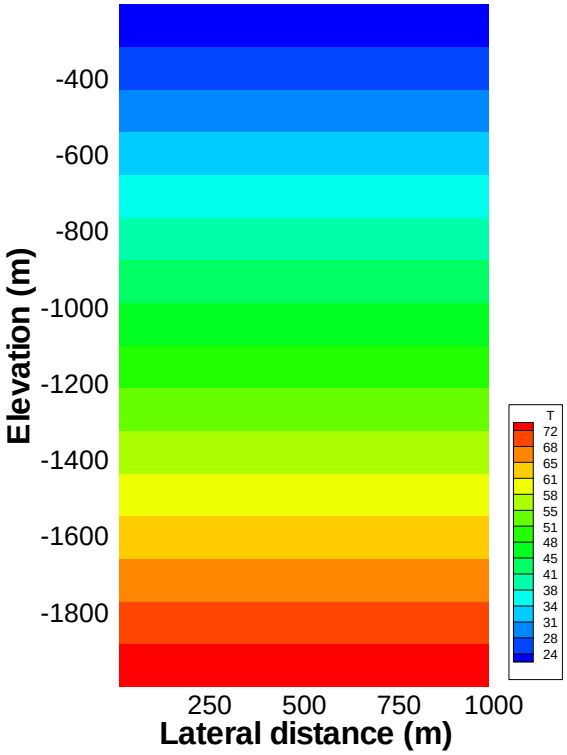

Figure 4.17. Computed initial (regional) temperature distribution (°C).

4.3.4.2. Model Results

Figure 4.18 shows the spatial distribution of pressure after 3.5 years. Pressure buildup (the difference between the pressure at a given time and the initial pressure) is observed in the overlying aquifer centering on the fracture zone. This buildup is caused by the inflow of CO_2 from depth and its accumulation at the top of the aquifer. While the flow of aqueous phase in the fracture zone is driven by the pressure buildup with a flow rate about 7×10^{-4} kg/s, the flow of gas is mainly driven by buoyancy force, having a flow rate about 3.3×10^{-2} kg/s at the bottom of the fracture zone at 3.5 years. Figure 4.19 shows the spatial distribution of SCC ("liquid") saturation. The injected CO_2 accumulates at the top of the storage formation and then moves horizontally both up and down gradient. When CO_2 encounters the fracture, it migrates upward and eventually enters the overlying aquifer. The pressure buildup changes the flow field in the overlying aquifer (see Figure 4.18), and consequently CO_2 spreads laterally in both directions, towards the left and right boundaries.

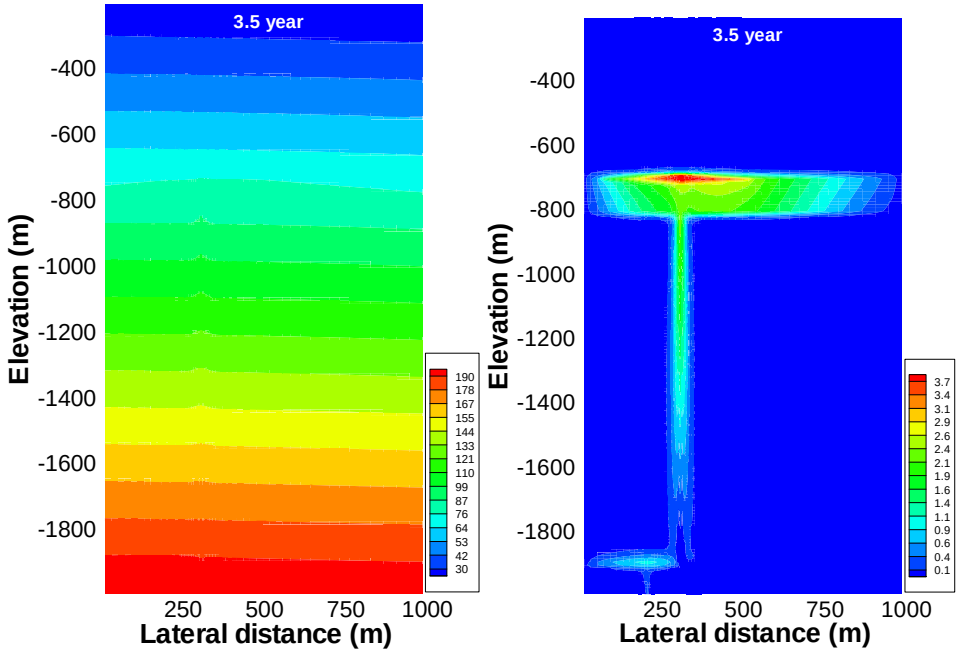

Figure 4.18. Computed spatial pressure distribution (left) and pressure buildup (the difference between the pressure at a given time and initial pressure) (right) after 3.5 years.

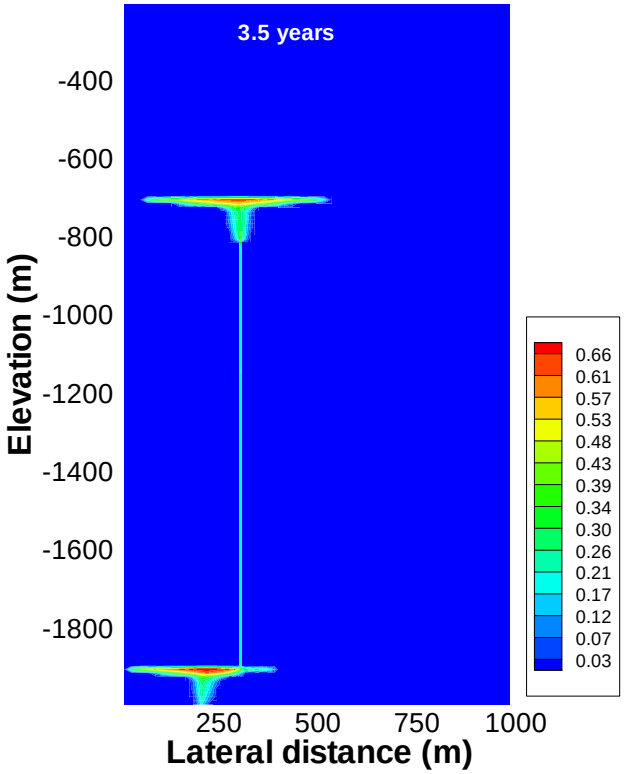

Figure 4.19. Computed spatial distribution of SCC ("liquid") saturation after 3.5 years.

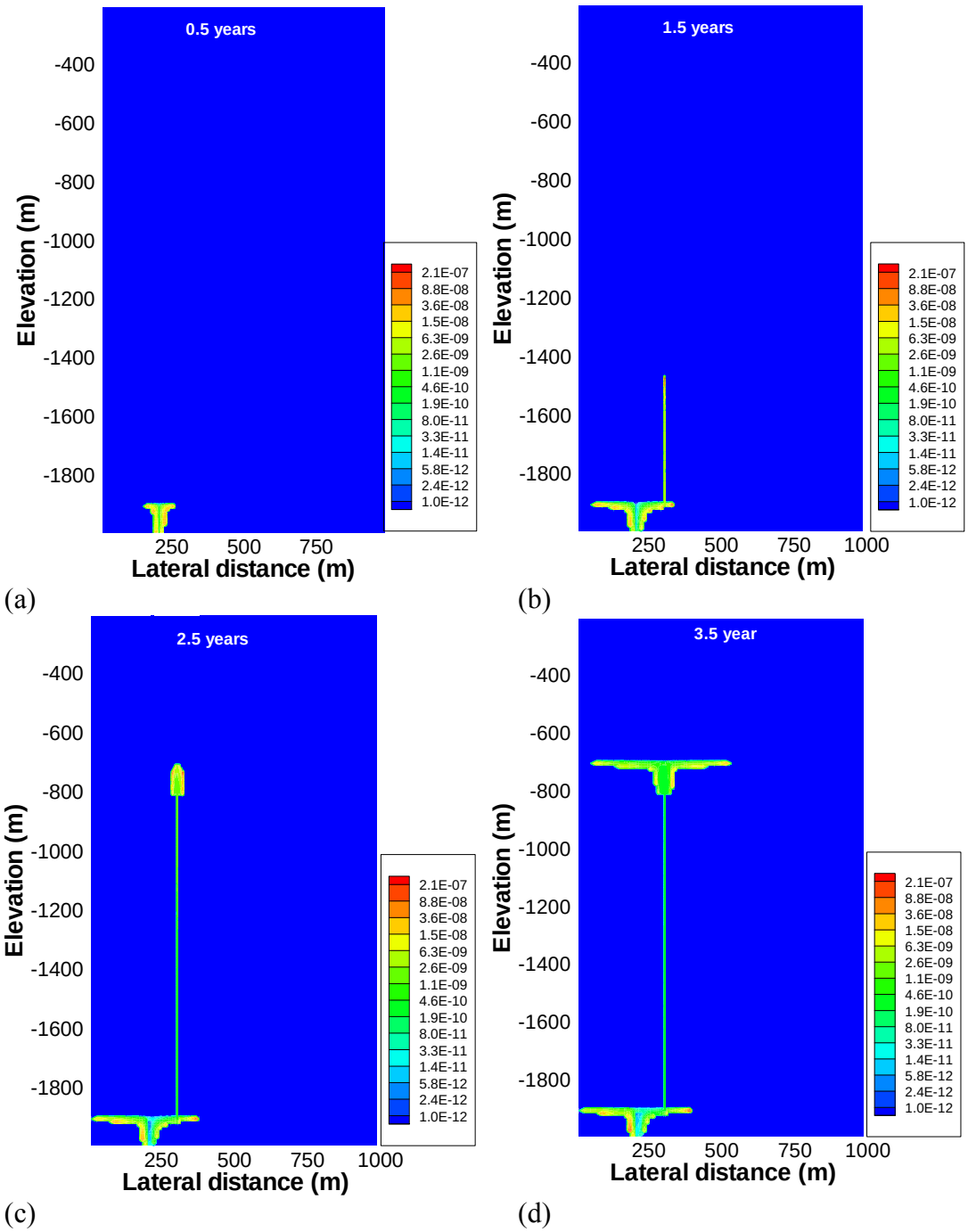

Figure 4.20. Spatial distribution of benzene mass fraction in the compressed "gas" phase at 0.5 (a), 1.5 (b), 2.5 (c) and 3.5 years (d).

Figure 4.20 shows the spatial distribution of the benzene mass fraction in SCC. Because of the preferential partitioning of benzene into SCC, benzene in the storage formation (aqueous and sorbed) is leached by the SCC. Benzene is then carried with the migrating SCC to the overlying aquifer. Because the aqueous solubility of benzene in contact with SCC is lower than the aqueous solubility of CO_2, benzene is actually enriched in the SCC as the plume advances, with the tip of the plume showing the highest mass fraction of benzene. Figure 4.21 shows that benzene becomes depleted from the aqueous phase in

the storage formation as it is removed by SCC, and is then introduced into the overlying shallower aquifer when benzene-laden SCC comes into contact with that aquifer. The resulting benzene concentrations in the shallower aquifer after 3.5 years are on the same order of magnitude as initial concentrations in the storage formation, with values up to 4.2×10^{-8} molal (~ 0.003 mg/L). At later times, these levels decrease as they get spread out further into the shallower aquifer. The level of contamination in this aquifer (maximum concentration) depends in part on the amount of benzene in SCC, which depends on the amount of benzene assumed present at depth, in this case about 0.001 mg/L in water (one fifth of the MCL) and $\sim1\times10^{-4}$ ppm in the sediments. Note that sorption of benzene onto sediments (organic matter) in the shallower aquifer is not considered, here, and therefore computed benzene concentrations in the shallower aquifer are more likely to be overestimated than underestimated. Also, given the uncertainty of model input parameters and model assumptions, these results should not be seen as actual predictions applying to any particular site, but more as a confirmation that compounds such as benzene would likely be transported by SCC, should leakage occur, reaching levels in shallower aquifers that would be quite site specific.

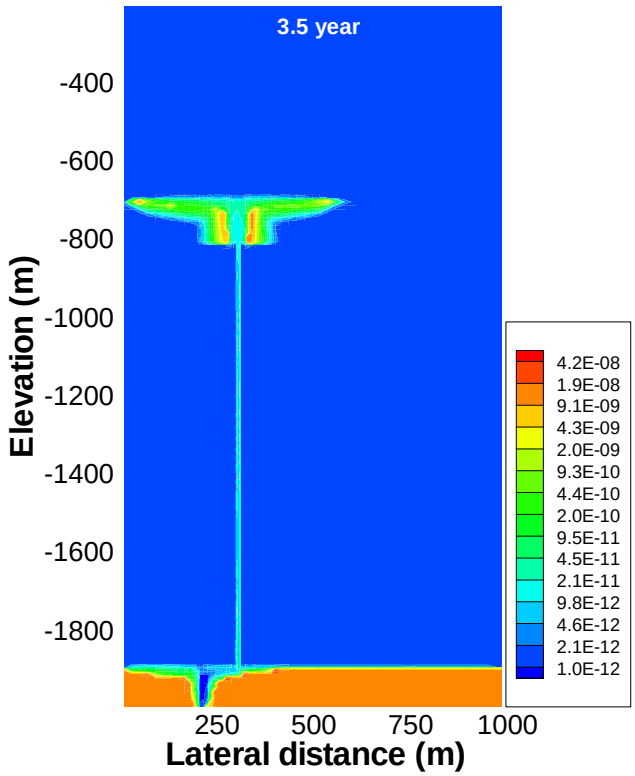

Figure 4.21. Spatial distribution of the concentration of aqueous benzene (molal) after 3.5 years

5. Impact of Co-Injection of CO_2 with H_2S

The co-injection of H_2S in CCS operations is being considered because the burning of fossil fuels can emit significant amounts of H_2S and SO_2 (which disproportionate into H_2S and H_2SO_4) in addition to CO_2. Because the separation of these gas impurities from power plant effluents is quite costly, and their release to the atmosphere is environmentally harmful, it may be advantageous to consider co-injecting these gases during CCS operations. For these reasons, in this section, we examine the impact of leakage from a deep saline aquifer into which H_2S is co-injected with CO_2.

The chemical interactions of reservoir rock with CO_2 and co-contaminants such as H_2S and SO_2 have been investigated by others through laboratory and modeling studies (e.g., Gunter et al., 2000 and 2005; Knauss et al., 2005; Palandri and Kharaka, 2005a,b; Xu et al., 2007; Bachu and Bennion, 2009; Murphy et al., 2010). Geochemical and reactive transport modeling studies so far have been directed primarily towards reservoir rock, focusing on CO_2 and H_2S sequestration reactions, as well as mineral alteration and pH buffering. These studies considered the mixing (Gunter et al., 2000, 2005; Palandri and Kharaka, 2005 and/or injection (Knauss et al., 2005; Xu et al., 2007) of water saturated with H_2S and CO_2 and subsequent chemical interactions with reservoir rock. Only Bachu and Bennion (2009) considered modeling the actual injection of supercritical H_2S+CO_2 mixtures, but without reactive chemistry. These authors observed the preferential dissolution of H_2S in water, compared to CO_2. However, the effect of this preferential dissolution on the fate of H_2S in storage formations and/or along a leakage pathway, and the resulting effects on water-rock interactions, remains mostly uninvestigated.

In contrast to earlier modeling work, the present study investigates the transport of CO_2-H_2S mixtures in a storage formation and along a hypothetical leakage pathway, and the potential effect of leakage on the quality of a freshwater aquifer overlying a storage formation. The focus is first on the development of a capability to simulate H_2S and CO_2 transport and partitioning in water (Section 5.1), then on the evaluation by numerical modeling of the H_2S fate after injection, including effects of preferential H_2S dissolution (over CO_2) in water (Section 5.2). The interaction of H_2S and CO_2 with metal-bearing sediments in a fresh water aquifer is also investigated, although to a limited extent and in a rather generic manner (i.e., non site-specific); this investigation can be compared with results of a previous generic study (Zheng et al., 2009) that considered injection of only CO_2.

5.1. Relevant Processes

The fate of co-injected H_2S in a storage formation is largely controlled by the partitioning of H_2S between the supercritical CO_2+H_2S mixture and the aqueous phase (brine), as well as by chemical reactions with rock minerals. These processes also affect the H_2S transport behavior along possible leakage pathways (such as a fault or a leaking wellbore) to shallow aquifers, and subsequent geochemical response to intrusion of the CO_2+H_2S mixture into shallow aquifers. As an introduction to the modeling studies presented in

Sections 5.2 and 5.3, we briefly discuss these processes below, and review the literature to provide ranges for relevant parameters used in the model.

5.1.1. *Phase Partitioning*

Laboratory work (Bachu and Bennion, 2009) has shown that gases contained in a CO_2 injection stream will chromatographically partition when in contact with the brine present in deep saline aquifers. As described in Bachu et al. (2009), chromatographic partitioning of various gases, when in contact with subsurface fluids, is not a new phenomenon. Actually, this phenomenon has been used extensively in the petroleum industry for inter-well tracer tests to determine the oil saturation and reservoir properties between injection and observation wells (e.g., Illiassov and Datta-Gupta, 2002; Tang, 2005), and also for the detection and estimation of nonaqueous phase liquids (NAPLs) present in the groundwater and in the vadose zone at contaminated sites (e.g., Deeds et al., 2000). Numerical models (Bachu et al., 2009) have shown that the preferential H_2S solubility in brine compared to that of CO_2 has a dominant effect on the chromatographic partitioning of these two gases, resulting in H_2S being stripped off at the leading edge of the advancing front of the CO_2+H_2S supercritical mixture. Specific attention was therefore paid to the solubility behavior of H_2S and CO_2 in the aqueous phase at varying subsurface pressure and temperature conditions. A detailed discussion of the partitioning of H_2S between CO_2 and water (brine) (as implemented in the simulator) is given in Appendix A, Section A.7.

5.1.2. *Chemical Processes in Response to H_2S+CO_2 Injection*

The specific chemical reactions involved in the injection of H_2S+CO_2 mixtures have been discussed in several modeling studies (e.g., Gunter et al., 2000 and 2005; Knauss et al., 2005; Palandri and Kharaka, 2005; Xu et al. (2007). As H_2S dissolves in water, one possible reaction is the reductive dissolution of ferric iron minerals (e.g., hematite) by sulfide according to the following reaction (Palandri and Kharaka, 2005):

$$4Fe_2O_{3\ (\text{hematite})} + 15H^+ + HS^- = 8Fe^{+2} + SO_4^{-2} + 8H_2O \qquad (5.1)$$

Subsequently, precipitation of iron sulfide (FeS) and pyrite could occur, as revealed in experimental (Jacquemet et al., 2008) and numerical (e.g., Xu et al., 2007) studies:

$$4Fe^{+2} + SO_4^{-2} + 7HS^- + H^+ = 4FeS_{2(\text{pyrite})} + 4H_2O \qquad (5.2)$$

The precipitation of amorphous FeS is favored kinetically (Palandri and Reed, 2001). However, amorphous FeS is typically replaced by pyrite if additional sulfide is available after all iron has precipitated as FeS (Palandri and Kharaka, 2005).

Although the deprotonation of H_2S tends to lower the pH of the solution, the reductive dissolution of hematite and the precipitation of pyrite consume hydrogen iron and consequently tend to buffer pH. Co-injection of H_2S has therefore a minor effect on pH (e.g., Xu et al., 2007), at least in an anoxic environment. The oxidation of H_2S to sulfuric

acid in oxic environments could have a profound effect on pH (e.g., Reed and Spycher, 1985). However, this case is not considered here because anoxic conditions are assumed to prevail at the depths considered for leakage.

Another possible reaction in response to the reductive dissolution of Fe(III) (hydr)oxides by sulfide is the precipitation of siderite (Palandri and Kharaka, 2005)

$$HCO_3^- + Fe^{+2} = FeCO_{3(siderite)} + H^+ \quad (5.3)$$

The precipitation of siderite could be important where sediments contain significant amounts of Fe(III) (hydr)oxides. The low pH conditions induced by the dissolution of CO_2 in water impede the precipitation of other carbonates. However, upon pH rise caused by reactions with formation minerals, calcite, ankerite, and dawsonite have been predicted to form and contribute to mineral trapping of CO_2 in the formation, if enough Ca-bearing minerals are present (Xu et al., 2007).

The possible precipitation of sulfate such as gypsum and anhydrite can also occur when sulfide is converted to sulfate during the reduction of ferric iron. In addition to these chemical reactions, co-injected H_2S can also trigger other reactions involving trace elements such as lead and arsenic, which are relevant for the risk assessment of leakage of CO_2 into shallow groundwater. Section 5.3 presents a detailed discussion of these reactions.

5.2. Fate of Co-injected H_2S in Deep Saline Aquifers

This section presents numerical simulations conducted to study (1) the fate of co-injected H_2S within the storage formation, and (2) the transport and breakthrough of H_2S into an overlying freshwater aquifer via a leakage pathway. The presence of a leakage pathway is assumed as a "what-if" risk assessment scenario, and the primary transport mechanism from depth to shallow formations is assumed to be the buoyancy- and pressure-driven co-migration of H_2S with SCC. We simulate the progressive partitioning of H_2S into the aqueous phase during transport in the storage formation and along the leakage pathway to evaluate the extent of H_2S removal from the buoyant CO_2+H_2S supercritical plume. Ultimately, we attempt to determine whether the preferential dissolution of H_2S (1) could retard the arrival of H_2S in a freshwater aquifer compared to the breakthrough of CO_2, and (2) might reduce the maximum concentrations of H_2S in the groundwater.

5.2.1. *H_2S Movement in the Storage Formation*

5.2.1.1. Model Setup

The model setup chosen to study the H_2S movement in a deep storage formation is rather simple (Figure 5.1). The model consists of a 2D vertical cross section through a reservoir and overlying aquitard. The storage formation is 100 m thick and extends 1000 m laterally. The horizontal discretization increases from Δx=5 m at the simulated well, to a maximum of Δx=40 m. Δz=10 m is used as vertical discretization. Pressure is fixed at the

left and right model boundaries, with pressure at 1 bar higher on the left boundary, which creates a flow from left to right under a hydraulic gradient of 1/100. Initially, static hydraulic pressures prevail throughout the entire model domain. The pressure at the top of the aquitard is ~180 bars; at the bottom of the aquifer it is ~200 bars.

Initially, the entire model domain includes only an aqueous phase. The aqueous phase consists of a 1-molal NaCl solution with dissolved CO_2 and H_2S at concentrations of 5.4×10^{-2} and 1.6×10^{-8} molal (corresponding to about 5% and 6×10^{-7}% of saturation concentrations, respectively, at initial pressures and temperatures). These values are taken from Xu et al. (2007), who obtained them on the basis of equilibrating a 1.0 molal NaCl solution with a typical mineral composition of the Texas Gulf Coast sediments (Xu et al., 2005) under a total pressure of 200 bar at a temperature of 75°C (yielding a CO_2 partial pressure ~ 0.1 bar at pH 6.7). The ionic strength of the aqueous phase is about 1 molal, and this effect of salinity on the solubility of CO_2 and H_2S is taken into account in the simulations (Appendix A, Section A.7).

A supercritical mixture of CO_2+H_2S is injected at a rate of 0.1 kg/s (~3,150 tons per year) in a stack of model gridblocks representing the injection well located 200 m away from the left boundary. The gas mixture contains 95% CO_2 and 5% H_2S (by mass). Simulations are run until the gas plume approaches the left model boundary, which is computed to take about 2 years.

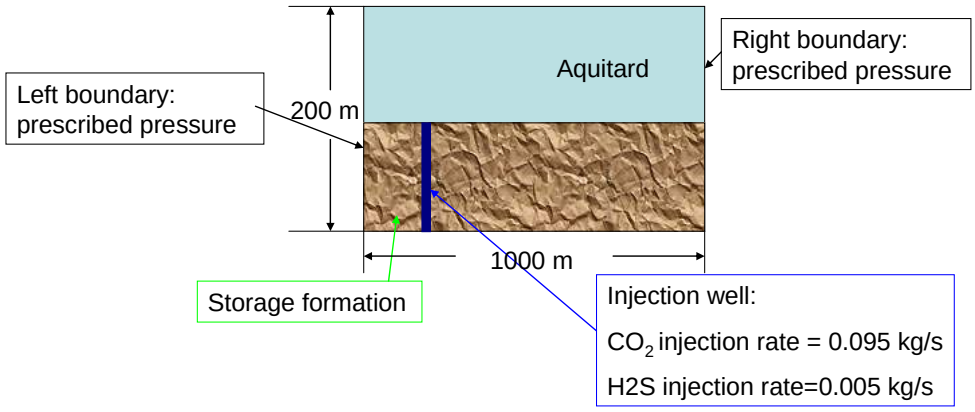

Figure 5.1. Schematic representation of the 2-D model used to simulate the movement of H_2S in a storage formation.

The hydrogeologic properties for aquifer and aquitard are the same as those used for the 2-D model for the simulation of benzene mobilization (see Table 4.9 in Section 4.3.4).

5.2.1.2. Model Results

Processes affecting the migration of SCC in the subsurface have been investigated in numerous modeling studies. As a result, parameters controlling the migration of SCC plumes have been identified. The sizes and shapes of SCC plumes may vary strongly,

depending on hydrogeological properties, subsurface heterogeneity, and the spatial and temporal scales considered. Figure 5.2 shows the spatial distribution of "gas" saturation computed for the case of a homogeneous formation, depicting a typical plume shape. The plume in this case consists of CO_2 and H_2S. It is concentrated along the top of the storage formation, as a result of buoyancy forces. The maximum fluid saturation is about 0.64. Because of the imposed flow gradient from left to right, the plume propagates slightly further towards the right model boundary. Note that this simulation is for a rather short time period of about 2 years, at which point the plume reaches the left model boundary and the simulation is stopped to avoid boundary effects.

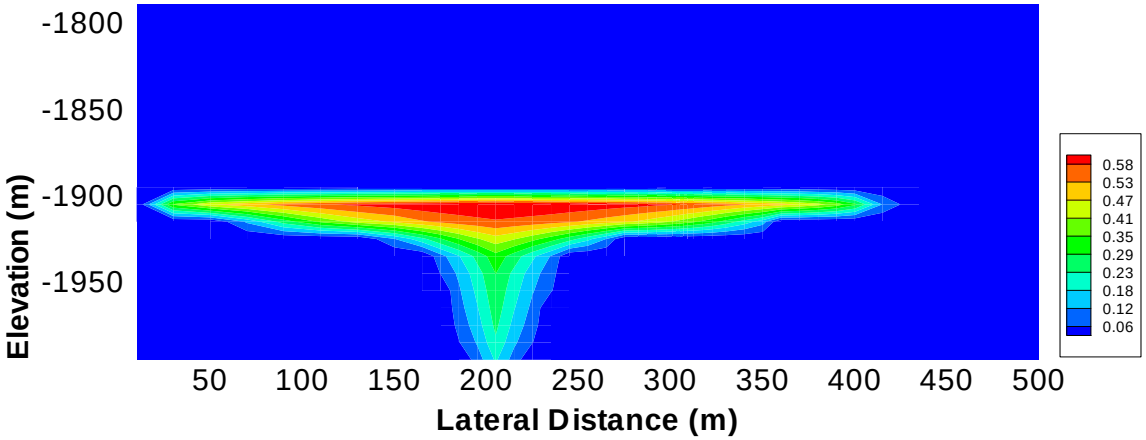

Figure 5.2. Contour of fluid saturation for the CO_2+H_2S supercritical mixture after 2 years of injection.

The mass fraction of CO_2 in the supercritical fluid gradually increases with lateral distance from the injection well (Figure 5.3), ranging from 0.95 to 0.99, with the maximum value at the tip of the plume (Figure 5.4). As the supercritical plume remains in contact with the aqueous phase, the component with higher solubility in the aqueous phase (i.e., H_2S) is preferentially extracted from the plume. Because CO_2 has lower solubility in water than H_2S, the CO_2 mass fraction in the supercritical fluid increases, while the H_2S mass fraction decreases. As seen in Figure 5.5 and 5.6, the H_2S mass fraction in the supercritical fluid phase decreases progressively with distance from the injection well, with much lower values obtained at the leading edge of the gas plume. These results are consistent with observation reported by Bachu and Bennion, (2009) and Bachu et al. (2009), i.e., that H_2S dissolves preferentially in brine, compared to CO_2. This chromatographic separation effect results in H_2S being stripped off at the leading edge of the advancing supercritical fluid.

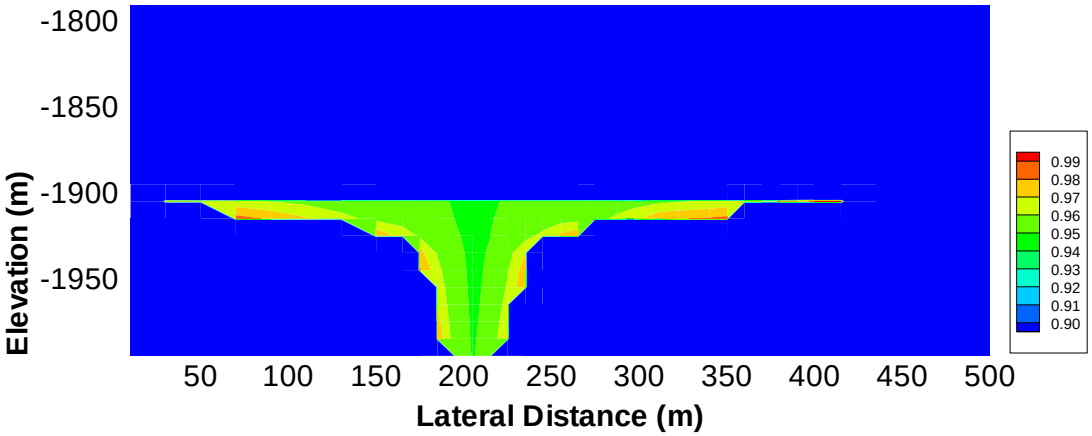

Figure 5.3. Contour of CO_2 mass fraction in the supercritical CO_2+H_2S supercritical mixture after 2 years of injection (the CO_2 mass fraction in the injected mixture is 0.95).

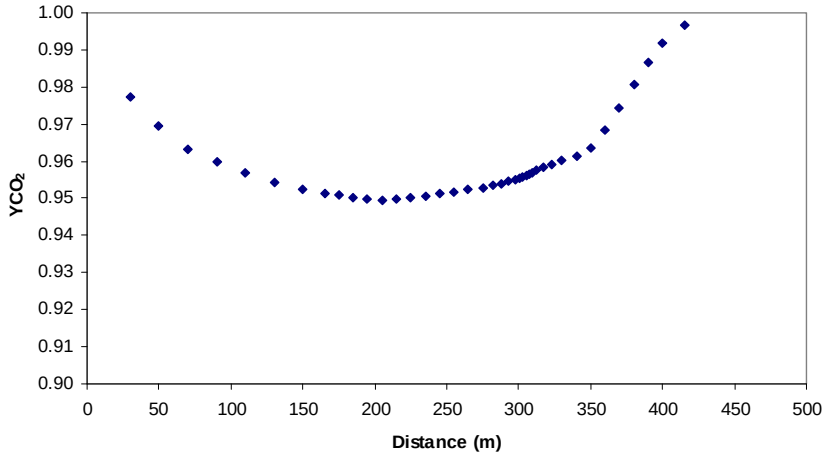

Figure 5.4. Profile of CO_2 mass fraction in the CO_2+H_2S supercritical mixture at z = -1900 (top of the storage formation) as a function of distance from the left model boundary after 2 years of injection (injection occurs at 200 m, with a CO_2 mass faction of 0.95).

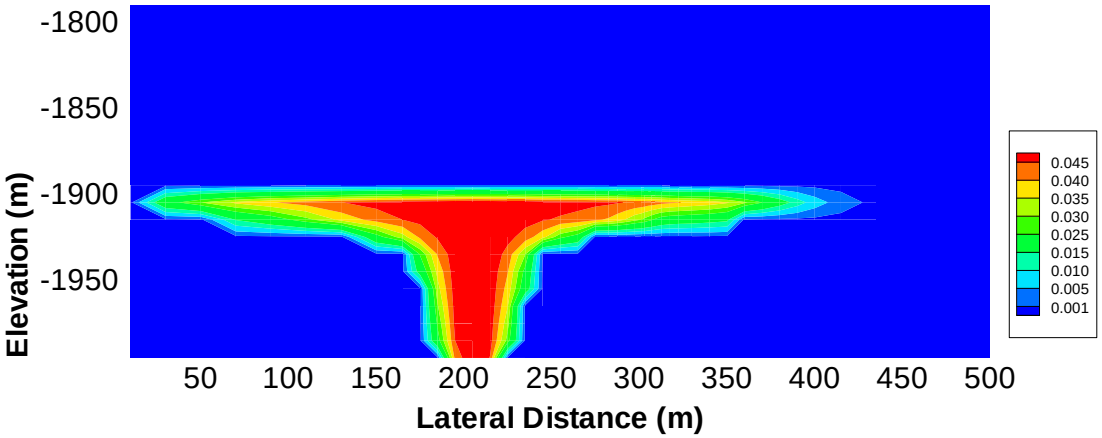

Figure 5.5. Contour of H_2S mass fraction in the CO_2+H_2S supercritical mixture after 2 years of injection (the H_2S mass fraction in the injected fluid is 0.05).

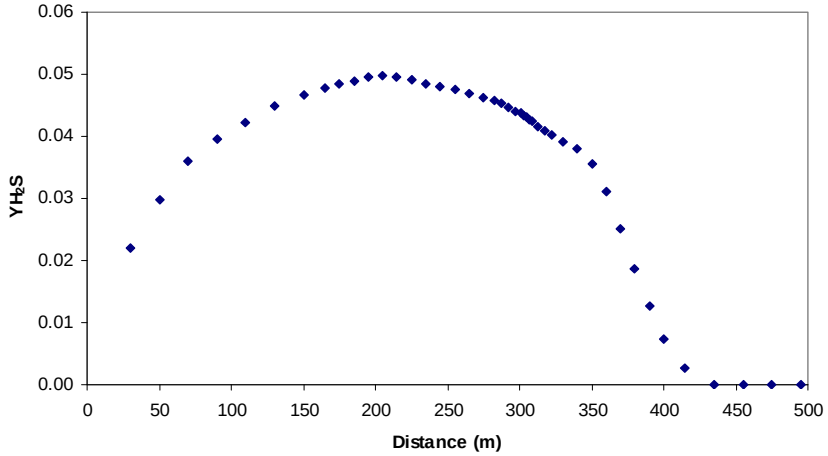

Figure 5.6. Profile of H_2S mass fraction in the CO_2+H_2S supercritical mixture at z = -1900 (top of the storage formation) as a function of distance from the left model boundary after 2 years of injection (injection occurs at 200 m, with a H_2S mass faction of 0.05).

The concentration of dissolved CO_2 in the aqueous phase inside the two-phase zone is controlled by the CO_2 partial pressure in the compressed gas (supercritical) plume (Figure 5.7). The higher CO_2 mass fraction at the leading edge of the plume, therefore, leads to a slightly higher concentration of dissolved CO_2 in the aqueous phase (Figure 5.8). Beyond the two-phase zone, the concentrations of aqueous CO_2 drop sharply. Small concentrations outside of the two-phase zone are caused mostly by diffusion. Similarly, the aqueous concentrations of H_2S are controlled by the H_2S partial pressure in the plume, and decrease gradually with travel distance away from the injection point (Figures 5.9 and 5.10).

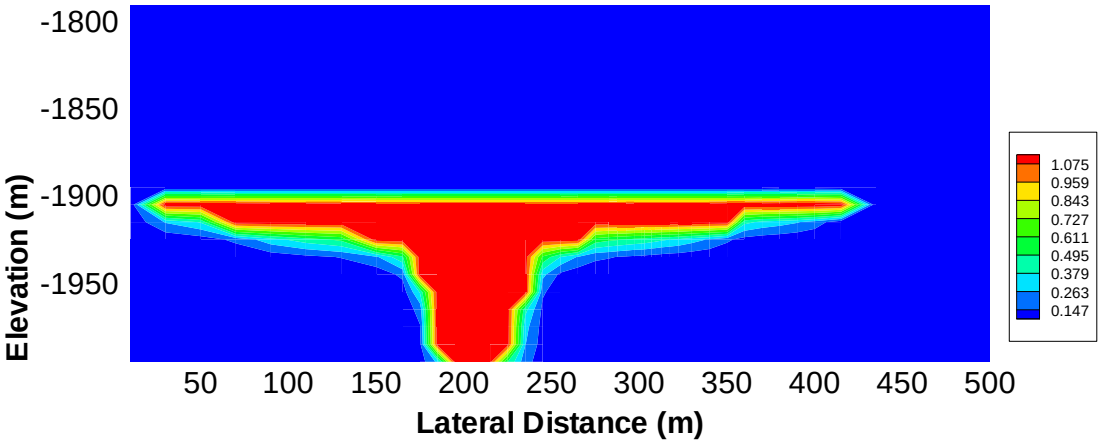

Figure 5.7. Contour of the concentration (molal) of dissolved CO_2 in the aqueous phase after 2 years of injection.

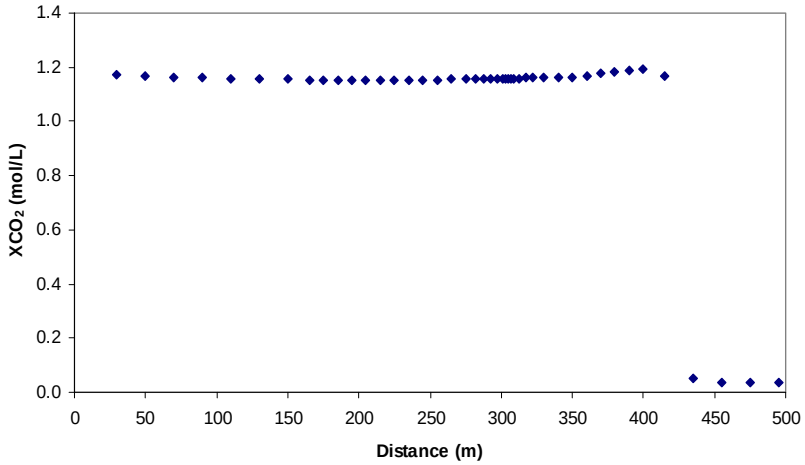

Figure 5.8. Profile of concentration (molal) of dissolved CO_2 in the aqueous phase at z = -1900 (top of the storage formation) as a function of distance from the left model boundary after 2 years of injection (injection occurs at 200 m).

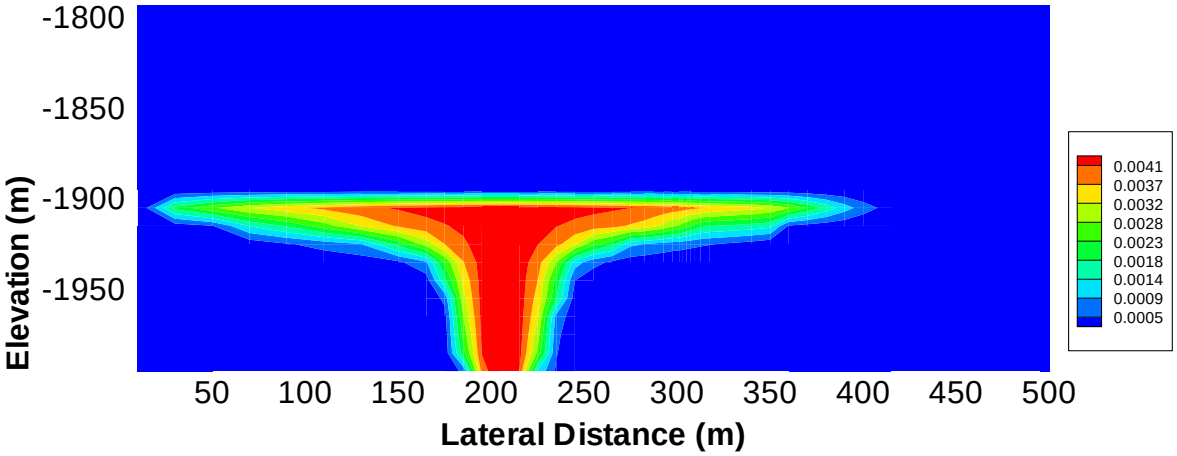

Figure 5.9. Contour of concentrations (molal) of dissolved H_2S in the aqueous phase after 2 years of injection.

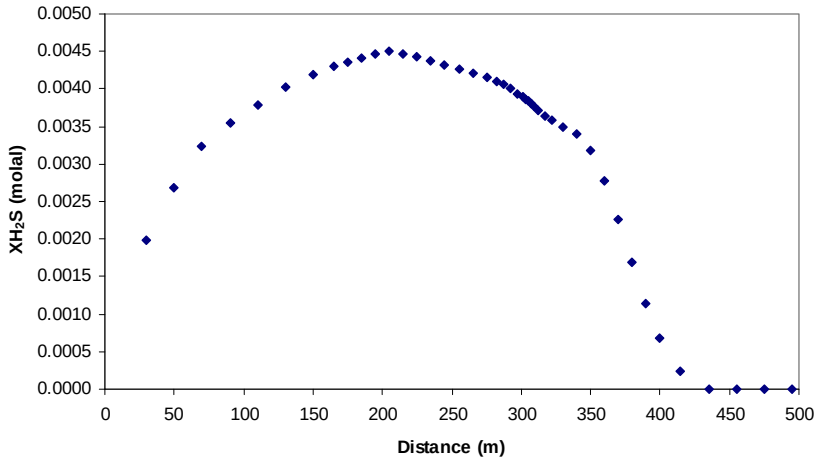

Figure 5.10. Profile of concentrations (molal) of dissolved H_2S in the aqueous phase at z = -1900 (top of the storage formation) as a function of distance from the left model boundary after 2 years of injection (injection occurs at 200 m).

5.2.2. *The Breakthrough of H_2S through a Leakage Pathway*

Studies of the breakthrough of H_2S in the CO_2 stream are relevant for understanding the fate of the injected CO_2 and associated H_2S in an injection stream, in devising monitoring procedures and protocols, and in developing emergency response plans in case of leakage of CO_2 and associated impurities. Bachu and Bennion (2009) discussed unpublished information suggesting breakthough of CO_2 ahead of H_2S at a producing well in a depleted gas reservoir. They subsequently confirmed this process by laboratory experiments (Bachu and Bennion, 2009) and numerical simulations (Bachu et al., 2009). Sensitivity studies conducted by these authors were helpful for identifying the factors that affect the breakthrough of H_2S. However, their experimental and modeling work was for column-scale systems. In addition, their column (coil) experiments and corresponding

numerical models were conducted under isothermal conditions and did not specifically address depth-dependent changes in pressure and temperature along a leakage pathway (e.g., a fracture zone or a fault). Assuming a hydrostatic pressure gradient and a geothermal gradient of 30°C/1,000 m, as shown in Figure 5.11, the difference between computed CO_2 and H_2S aqueous solubilities significantly narrows with decreasing depth (Figure 5.12). Therefore, the chromatographic separation effect observed by Bachu and Bannion is expected to decrease as the H_2S+CO_2 mixture ascends along a leakage pathway, which would be expected to fasten H_2S breakthough into a shallow aquifer. Given this observation, a larger-scale model of leakage along a preferential pathway (including declining pressures and temperatures along the flow path) is deemed best to investigate how the breakthrough of H_2S is delayed compared with that of CO_2 under conditions closer to an actual injection scenario. This is what is done here, as explained further below.

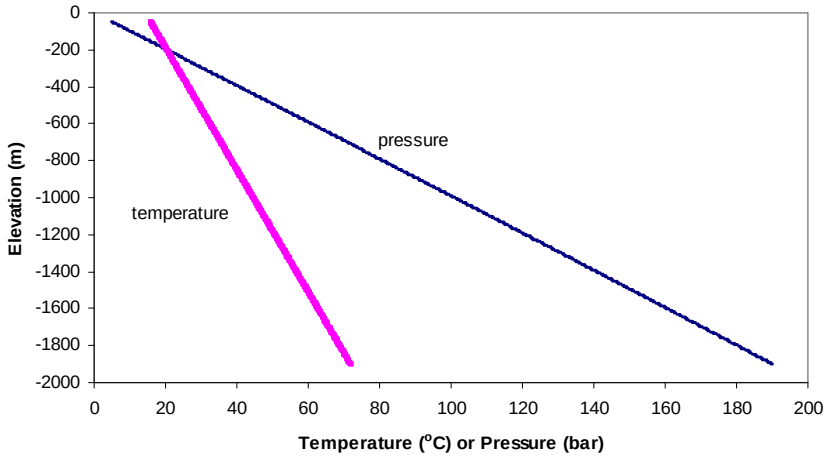

Figure 5.11. Profile of temperature (thin line) and pressure (thick line) with depth assuming a hydrostatic pressure gradient and a geothermal gradient of 30 °C/1,000 m (for use in computing the CO_2 and H_2S solubilities shown on Figure 5.12).

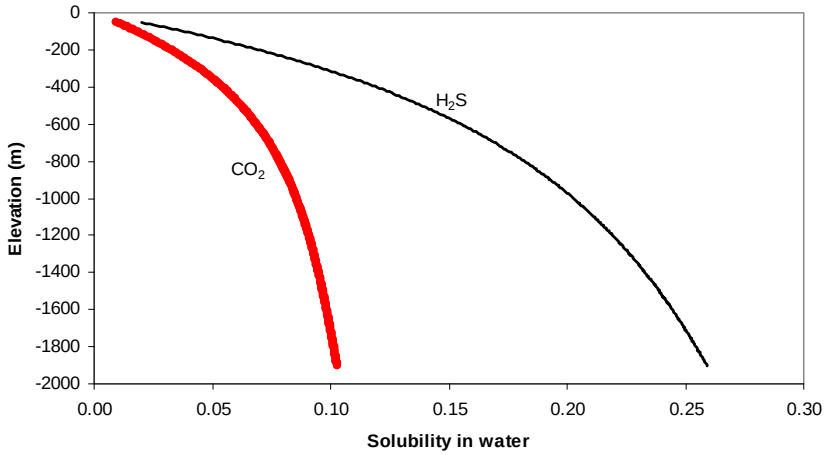

Figure 5.12. Computed solubilities (mass fraction) of CO_2 and H_2S in water as a function of depth, following temperature and pressure profiles shown on Figure 5.11.

Starting with the model setup presented in Section 5.2.1, we assume a hypothetical vertical preferential pathway (e.g., a fracture) located 100 m downstream of the injection well (300 m from the left model boundary). This "fracture" connects the deep storage reservoir with an overlying aquifer, as shown in Figure 5.13. The resulting model domain is the same as that discussed for benzene mobilization in Section 4.3. It consists of a vertical 2-D cross section, which includes the deep storage formation overlain by a reservoir "seal" formation (first aquitard), the overlying shallow aquifer, and another aquitard at the top of the model. Pressures on the left and right boundaries are fixed following a vertical hydrostatic gradient. A regional horizontal hydraulic gradient of 1/100 is applied over the domain, with a regional flow direction from left to right. As previously, a mixture of CO_2 and H_2S (95 and 5% by weight, respectively) is injected in a gridblock located 200 m from the left boundary, stacked across the entire formation thickness. The injection rate is 0.1 kg/s (3.2×10^3 tones/year). The pressure at the top of the model domain is around 20 bar and that at the bottom is about 200 bar. Temperature is 21°C at the top and 75°C at the bottom, assuming a geothermal gradient of 30^oC/1000 m. These initial conditions of temperature and pressure, as well as hydrologic properties, are the same as those described for the benzene mobilization simulations presented in Section 4.3.

The hydrogeologic properties chosen for the model are given in Table 4.9 (Section 4.3.4). The properties of the aquifers are typical of sedimentary formations suitable for CO_2 storage, with sufficient permeability and porosity. The properties of all sealing layers are representative of shale formations suitable for trapping CO_2, with small permeability and high capillary entry pressure. The permeability of the fracture zone is one order of magnitude higher than that of the aquifer, while other properties such as the retention curve and relative permeability are the same as those for the aquifer. The width of the fracture zone is 6 m.

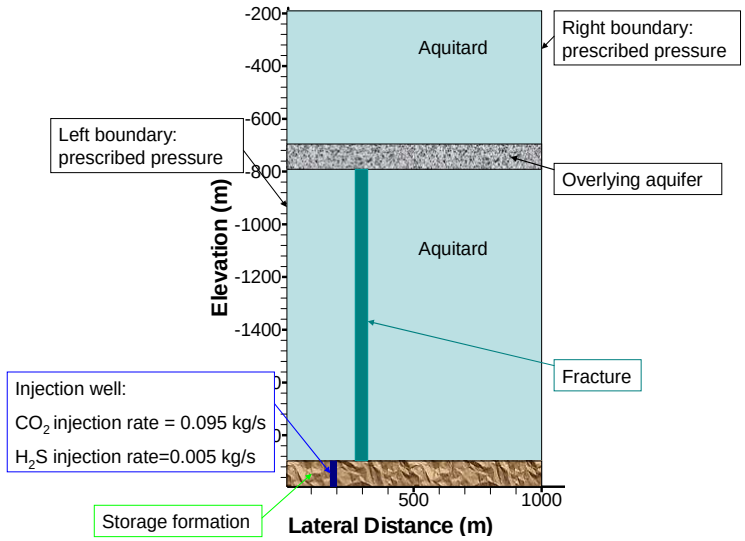

Figure 5.13. Schematic representation of the 2-D model used to simulate leakage of a CO_2+H_2S supercritical mixture.

The simulations are run for 3.5 years of CO_2+H_2S injection, until the plume reaches the left model boundary in the overlying aquifer. At this point, simulations are stopped to avoid boundary conditions affecting the model results. Figure 5.14 shows the spatial distribution of the "gas" plume fluid saturation at different times. After injection starts, the resulting plume accumulates at the top of the storage formation, moving both down- and upgradient from the injection point (Figure 5.15a). When it encounters the fracture zone, it migrates upward (Figure 5.14b), enters the overlying aquifer (Figure 5.14c), then spreads out laterally into the shallower aquifer (Figure 5.14d). The fracture zone also affects the migration of the CO_2+H_2S plume within the storage formation. As shown in Figure 5.14(b), once the plume encounters the fracture, its movement further downgradient within the storage formation is consequently delayed.

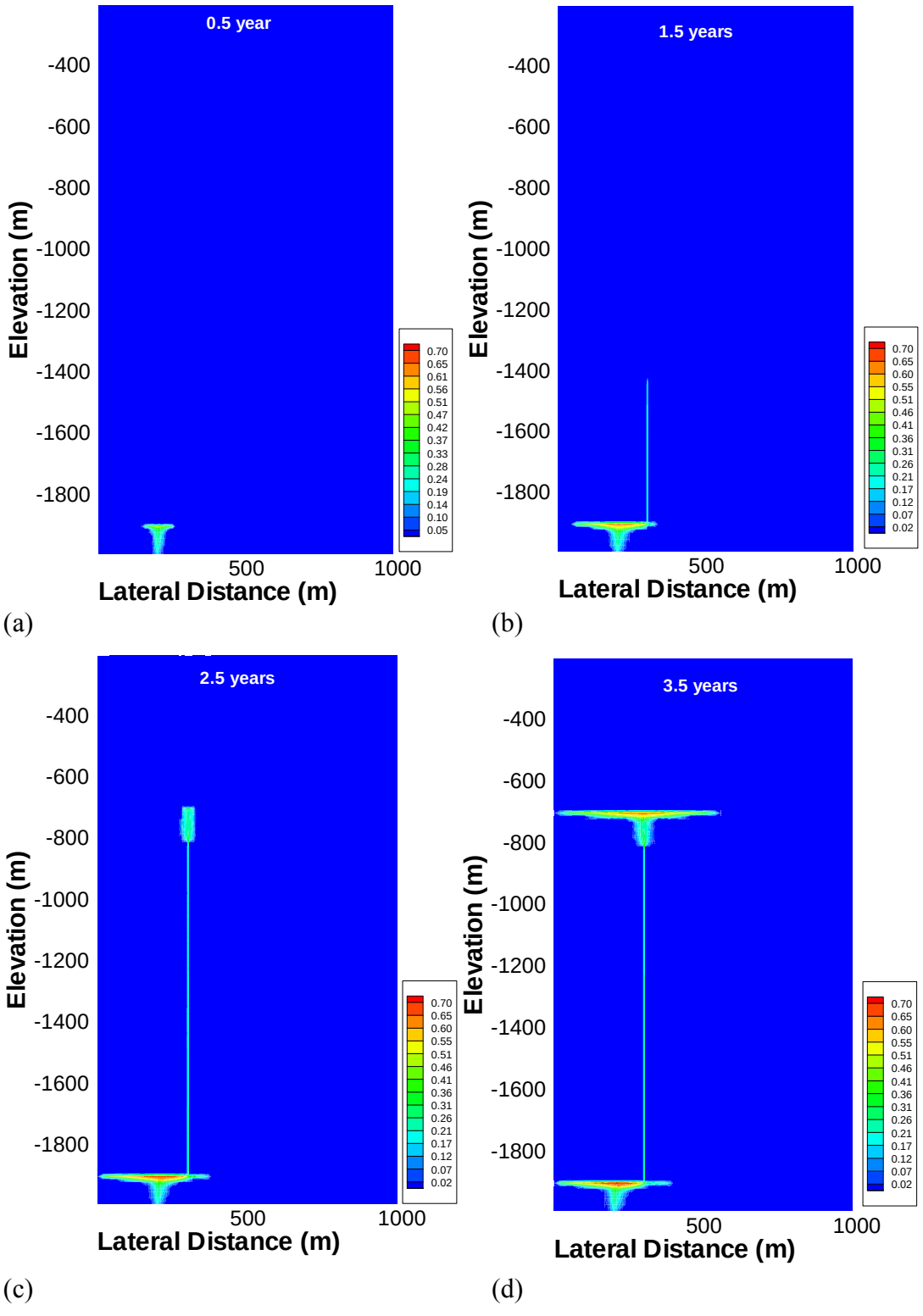

Figure 5.14. Snapshots of the "gas" plume fluid saturation at 0.5 (a), 1.5 (b), 2.5 (c), 3.5 (d) years.

Figure 5.15 shows the spatial distribution of pressure after 3.5 years. Figure 5.16 shows the pressure buildup (the pressure at a given time minus initial pressure) at different times. The injection of the CO_2+H_2S mixture increases the local pressure, and subsequently the pressure builds up in the fracture zone (the most permeable media in this simulation) and the shallow aquifer. As shown in Figure 5.16a, at early times, although the plume has spread over a rather small area around the injection well (Figure 5.14a), the pressure buildup has already spread to the overlying aquifer. As the plume advances into the fracture zone, the pressure buildup becomes largest in this zone. As the plume continues to spread out into the overlying aquifer, the pressure continues to build up, with the maximum values appearing at the top of the overlying aquifer.

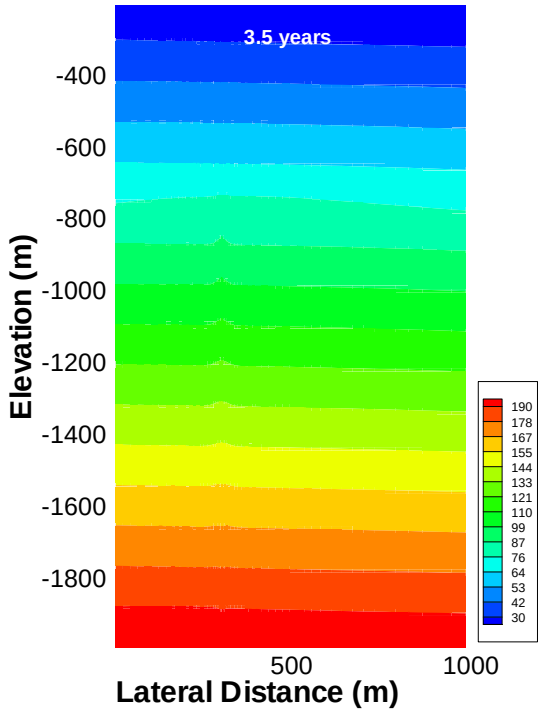

Figure 5.15. Spatial pressure (bar) distribution after 3.5 years

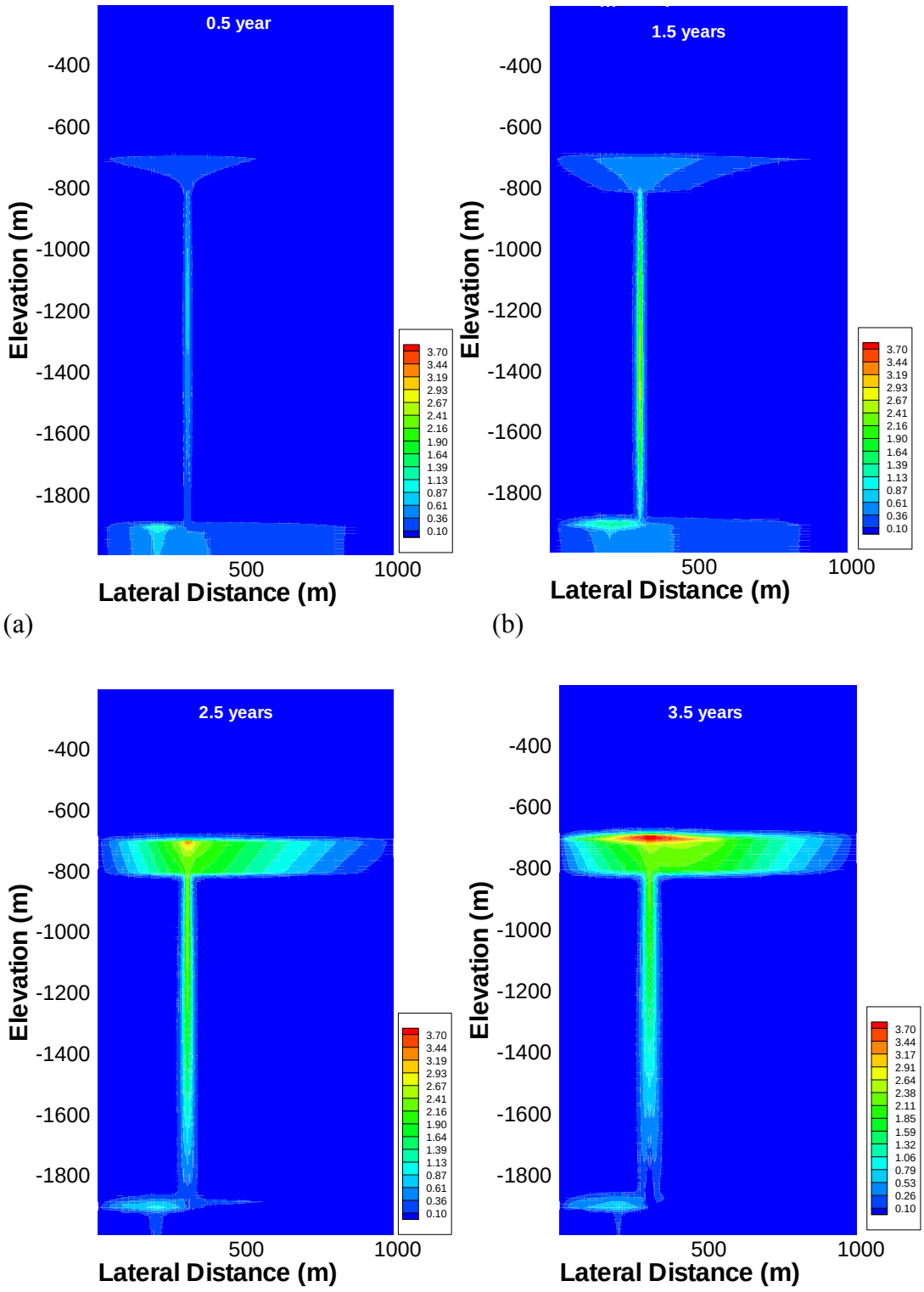

Figure 5.16. Snapshots of pressure buildup (pressure at a given time minus initial pressure) at 0.5 (a), 1.5 (b), 2.5 (c), 3.5 (d) years.

Figure 5.17 shows the spatial distribution of H_2S mass fraction in the compressed "gas" plume. The preferential dissolution of H_2S in solution strips H_2S from the edge of the advancing plume. Such preferential dissolution is more significant upgradient (left side of the plume), owing to the influx of H_2S-undersaturated water. Along the path from the injection point to the fracture zone where the plume continuously moves, the mass fraction of H_2S in the plume remains more or less constant and at the same value as the mass fraction at the injection point.

Figure 5.18 shows the profile of H_2S mass fraction in the plume along the x direction at the top of the storage formation. From the injection well location (at x=200 m) to the fracture zone (at x=300 m), the mass fraction of H_2S in the plume is almost the same as that in the injected mixture. This suggests that leakage could allow co-migration of CO_2+H_2S at concentrations close to the levels in the injected mixture. The profile of H_2S mass fraction in the gas phase along the x direction at the top of the overlying aquifer (Figure 5.19) is characterized by a smooth drop on each side of the point of influx where H_2S in the compressed "gas" phase is preferentially fractionated into the aqueous phase.

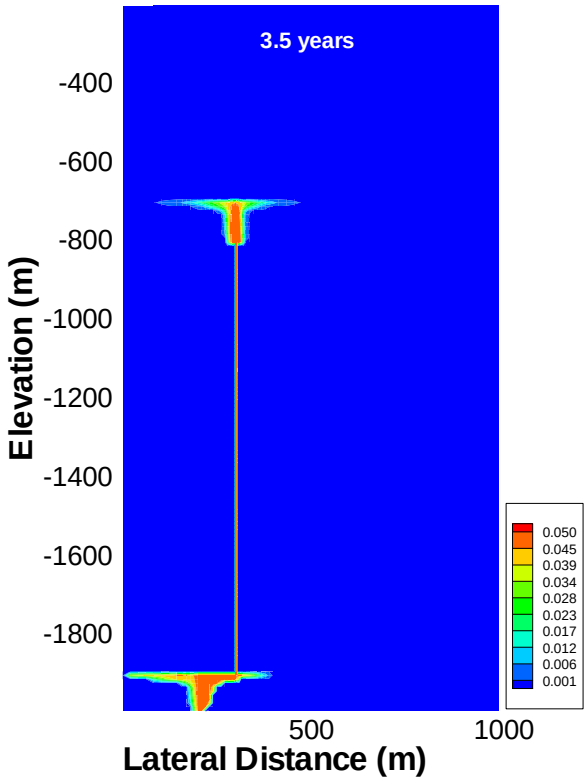

Figure 5.17. Spatial distribution of mass fraction of H_2S in the compressed "gas" plume after 3.5 years of injection.

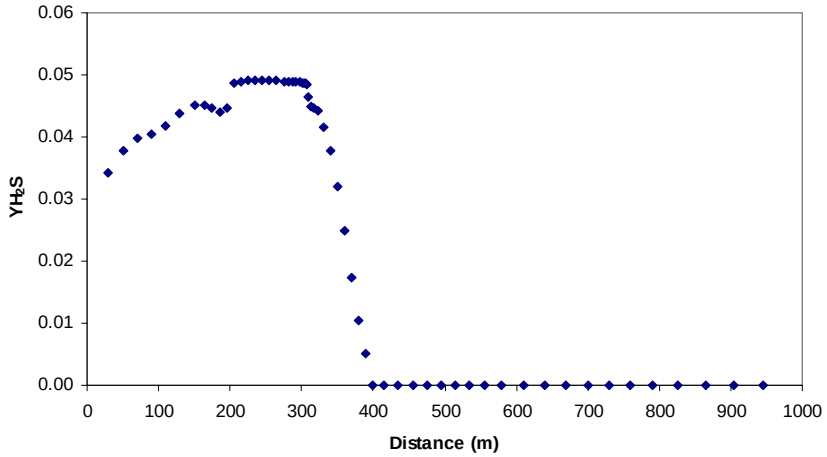

Figure 5.18. Profile of H_2S mass fraction in the compressed "gas" plume (YH_2S) at z = -1900 (top of the storage formation) as a function of distance from the left model boundary after 3.5 years of injection (injection occurs at 200 m).

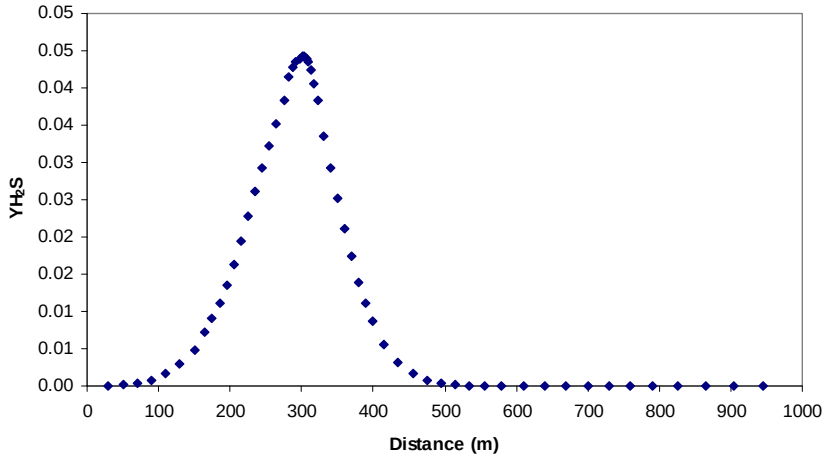

Figure 5.19. Profile of H_2S mass fraction in gas phase (YH_2S) at z = -700 (top of the overlying aquifer) as a function of distance from the left model boundary after 3.5 years of injection (leakage into the aquifer occurs at 300 m).

As the gaseous H_2S is stripped from the edge of the gas plume, the mass fraction of CO_2 in the gas phase increases correspondingly. Figure 5.20 shows the spatial distribution of CO_2 mass fraction in the plume after 3.5 years. The profile of these mass fractions along the x direction at the top of the storage formation (Figure 5.21) and at the top of the overlying aquifer (Figure 5.22) shows more clearly the enrichment of CO_2 in the gas phase (relative to H_2S) caused by the chromatographic partitioning.

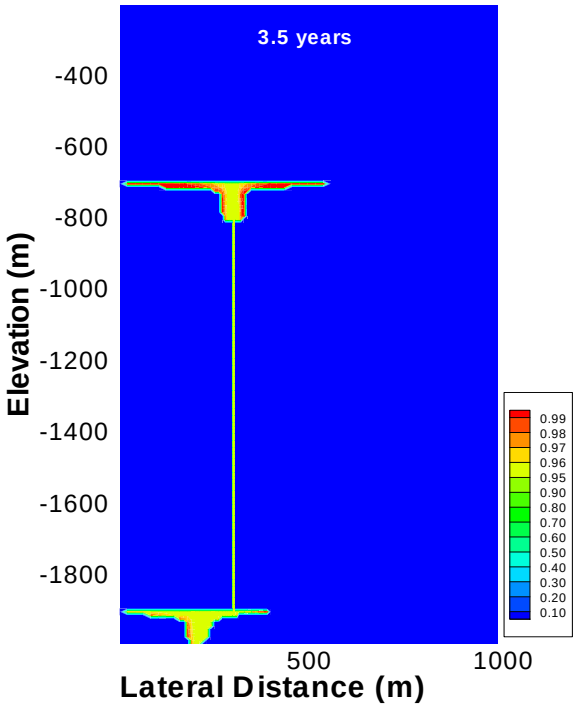

Figure 5.20. Spatial distribution of CO_2 mass fraction in the compressed "gas" phase after 3.5 years.

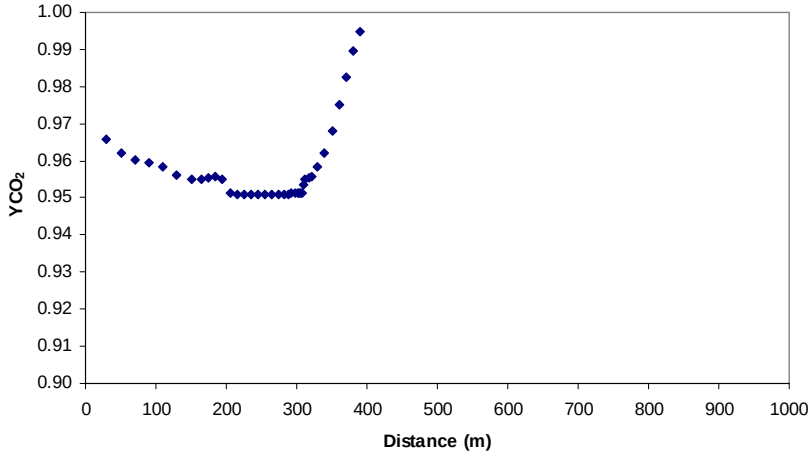

Figure 5.21. Profile of CO_2 mass fraction in the compressed "gas" plume (YCO_2) at z = -1900 (top of the storage formation) as a function of distance from the left model boundary after 3.5 years of injection (injection occurs at 200 m).

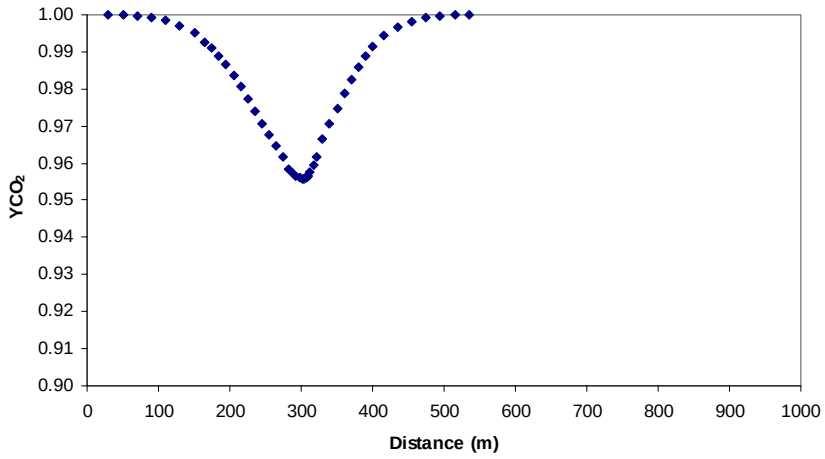

Figure 5.22. Profile of CO_2 mass fraction in the compressed "gas" plume (YCO_2) at z = -700 (top of the overlying aquifer) as a function of distance from the left model boundary after 3.5 years of injection (leakage into the aquifer occurs at 300 m).

A gas mixture of H_2S+CO_2 with the same proportion of each component as the injected mixture eventually migrates through the fracture and enters the overlying aquifer (Figures 5.21 and 5.22); however, the arrival of H_2S is delayed. Figure 5.23 shows the time evolution of the H_2S mass fraction in the plume at the bottom of the fracture zone where it connects to storage formation (point A), and at the top of the fracture zone where it connects to the overlying aquifer (point B). The plume arrives at point A after 0.84 years, migrates upward in the fracture, and arrives at point B after 2.05 years. The breakthrough curves of H_2S mass fraction shows different trend for points A and B. The breakthrough curve at point A is characterized by a sharp initial increment in mass fraction followed by a slow increase after the mass fraction of H_2S rises to about 0.04. The breakthrough curve at point B shows mass fractions that remain small at first, then sharply increase about 4 months after the plume first arrives, and eventually later reach a plateau value close to 0.05 (the mass fraction of H_2S in the injected stream). As seen from Figures 5.23 and 5.24, the breakthrough of H_2S is delayed, and the extent of delay depends on location (at point B, the plume contains nearly pure CO_2 for about 4 months).

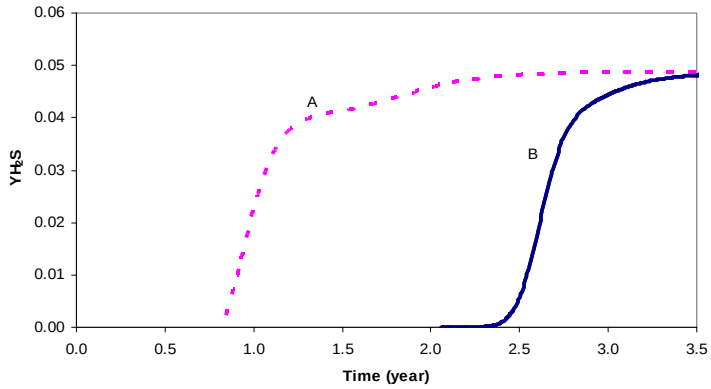

Figure 5.23. Time evolution of the H_2S mass fraction (YH_2S) in the compressed "gas" plume at the bottom of the fracture (A), where the fracture connects to the storage formation, and at the top of the fracture (B), where the fracture connects to the overlying aquifer.

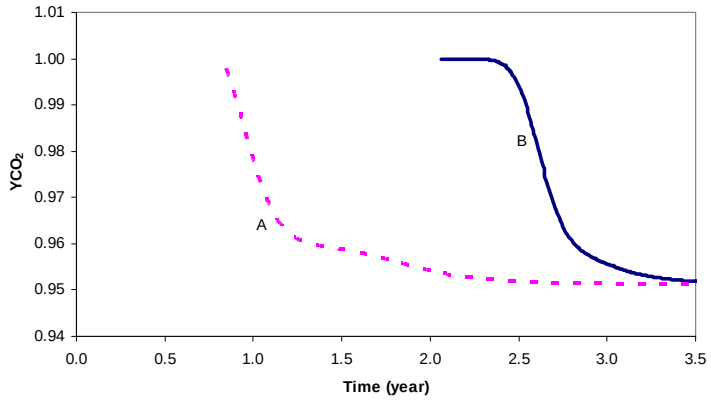

Figure 5.24. Time evolution of the CO_2 mass fraction (YCO_2) in the compressed "gas" plume at the bottom of the fracture (A), where the fracture connects to the storage formation, and at the top of the fracture (B), where the fracture connects to the overlying aquifer.

Because of diffusion, the plumes of CO_2 and H_2S in the aqueous phase spread beyond the extent of the compressed "gas" plume (Figure 5.25 and 5.28). In the two-phase zone, the concentrations of aqueous CO_2 and H_2S are controlled by the partial pressures (and thus mass fractions) of these gases in the compressed "gas" plume. Because the mass fraction of CO_2 in the compressed "gas" plume is higher at the plume edge than at the injection point, the concentration of CO_2 in the aqueous phase is higher at that location, and decreases away from the plume (Figures 5.24 and 5.27). The concentrations of aqueous H_2S are controlled by the same process. In this case, the H_2S mass fraction in the compressed "gas" plume is highest at the injection point, and as a result the profile of aqueous H_2S concentrations shows a continuously decreasing trend from the center towards the edge of the two-phase zone (Figures 5.29 and 5.30). Note that the concentration of aqueous H_2S and CO_2 are higher in the storage formation than those in the overlying aquifer (Figure 5.26 and 5.29), because of the solubility decrease with pressure and temperature.

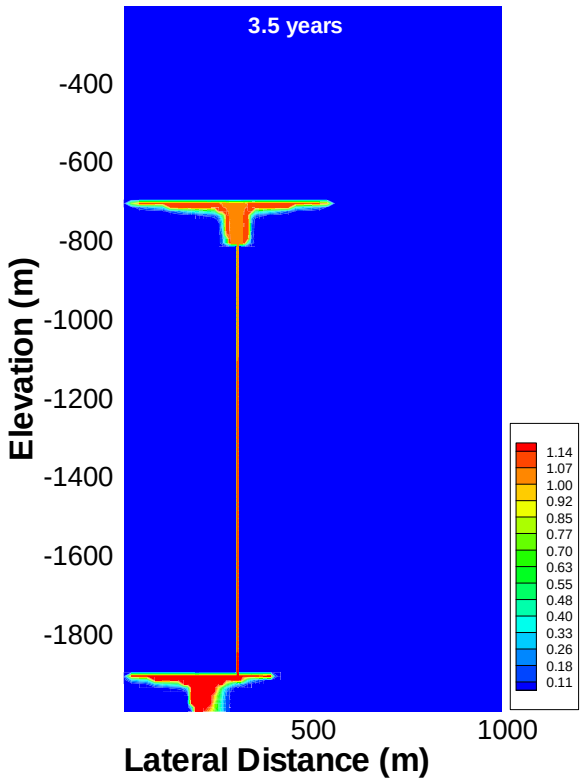

Figure 5.25. Spatial distribution of CO_2 concentration (molal) in the aqueous phase after 3.5 years of injection.

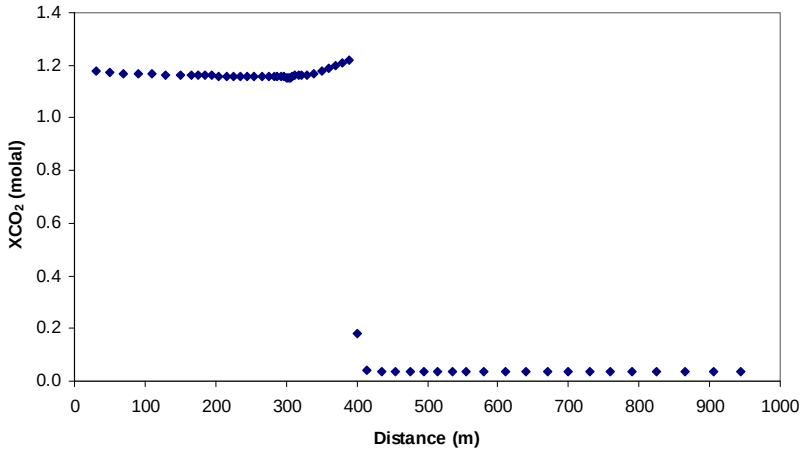

Figure 5.26. Profile of CO_2 concentration (XCO_2) in the aqueous phase at z = -1900 (top of the storage formation) as a function of distance from the left model boundary after 3.5 years of injection (injection occurs at 200 m).

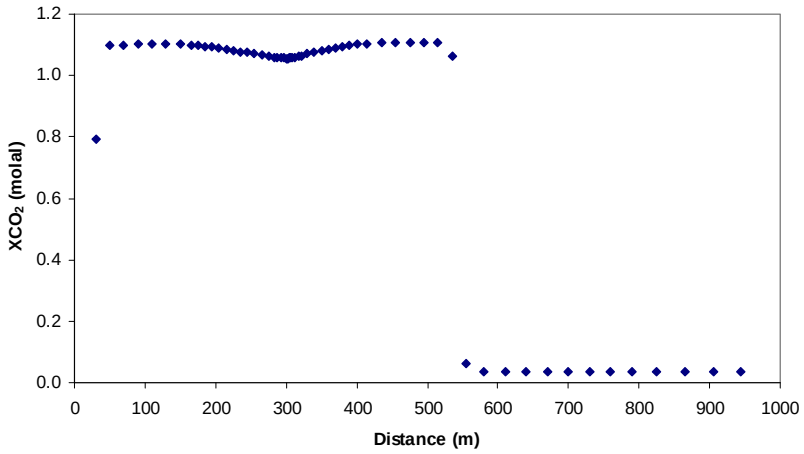

Figure 5.27. Profile of CO_2 concentration (molal) in the aqueous phase at z = -700 (top of the overlying aquifer) as a function of distance from the left model boundary after 3.5 years of injection (leakage into the aquifer occurs at 300 m).

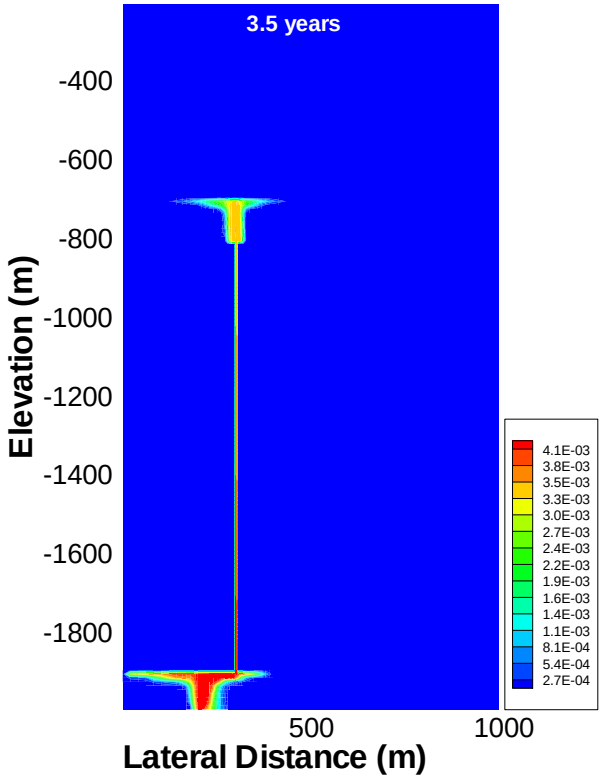

Figure 5.28. Spatial distribution of H_2S concentration (molal) in the aqueous phase after 6 years of injection.

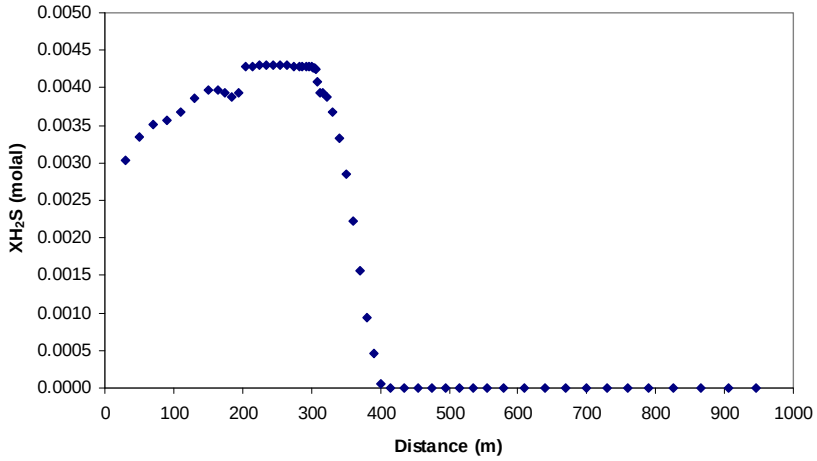

Figure 5.29. Profile of dissolved H_2S concentration (molal) in the aqueous phase at z = -1900 (top of the storage formation) as a function of distance from the left model boundary after 6 years of injection (injection occurs at 200 m).

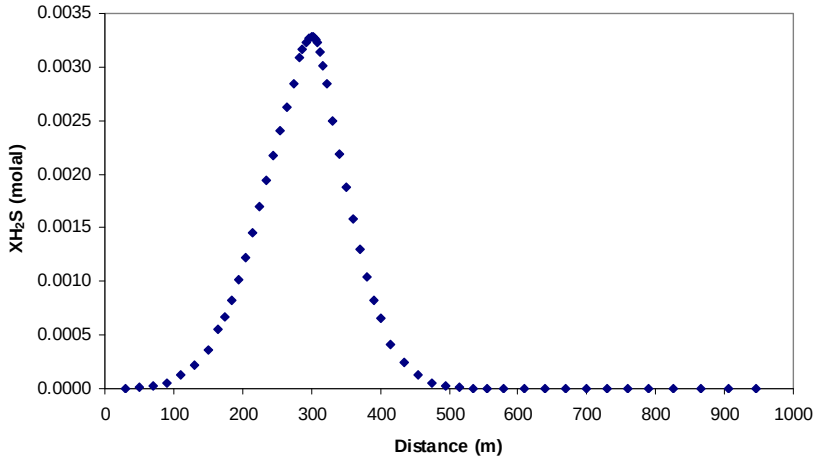

Figure 5.30. Profile of dissolved H_2S concentration (molal) in aqueous phase at z = -700 (top of the overlying aquifer)as a function of distance from the left model boundary after 6 years of injection (leakage into the aquifer occurs at 300 m).

5.3. Impact of co-injected H_2S on the quality of a fresh water aquifer

The model simulations presented in Section 5.2 indicate that the breakthrough of H_2S co-migrating with CO_2 along a preferential pathway may be delayed compared to the arrival of the bulk compressed "gas" phase. At some point in time, however, the ratio of H_2S to CO_2 in the leaking compressed "gas" reaching an overlying aquifer is expected to eventually approach the levels in the injected gas mixture. Therefore, the question raised is: to what extent does the intrusion of an H_2S+CO_2 mixture into a freshwater aquifer affect water quality? Simulations are conducted here to address this issue, focusing on the behavior of toxic metals such as lead and arsenic in an anoxic environment. Obviously,

the presence of H_2S in water itself is a water quality issue, because of its "rotten egg" odor and concentration. Although the odor and concentration of dissolved H_2S are not included in the contaminants list of EPA National Primary Drinking Water Regulations (the legally enforceable standards), they are specified in the contaminants list of the National Secondary Drinking Water Regulations (the non-enforceable guidelines regulating contaminants): the secondary standard for odor is three times the threshold odor number and that for sulfate is 250 mg/L (2.6×10^{-3} mol/L). Because the odor threshold for H_2S is very low, 8.1 ppb (Amoore and Hautala, 1983), the presence of H_2S in water can easily lead to odor that exceeds the National Secondary Drinking Water Regulations. If the H_2S is oxidized to sulfate, there is also a possibility that the concentration of sulfate might exceed the Secondary Drinking Water Regulations.

5.3.1. *Model Setup: Base Case*

The possible groundwater quality changes in response to the leakage of pure CO_2 have been studied systematically with generic numerical models by Zheng et al. (2009) and Apps et al. (2010). In this report, the same model setup is used as a base case, with the only difference being that a mixture of H_2S and CO_2 (instead of CO_2 alone) is assumed to intrude into the aquifer, consequently allowing direct comparison of model results for the base case (H_2S+CO_2) with earlier model results (CO_2 only). It should be noted that the assumed temperature and pressure conditions in the simulated aquifer in this case are 25°C and 5 bar, which differ from the conditions assumed in simulations presented earlier in this study.

The model is setup as shown in Figure 5.31. It consists of a horizontal 2D model with a given constant thickness Δz =10 m, with spatial discretization Δx =10 m and Δy = 10 m . The hydrogeologic properties, as given in Table 5.1, are homogeneous and constant in time. The initial chemical composition of groundwater is given in Table 5.2, which is taken from Zheng et al. (2009). The host mineralogy of the aquifer is similar to that used therein, except that orpiment (As_2S_3) and realgar (As_4S_4) are added to the list of potential secondary minerals that could form in cases of high sulfide concentrations. Equilibrium constants for these minerals are taken from Spycher and Reed (1989). Table 5.3 shows the kinetic data adopted for all the minerals included in the simulation. Kinetic rate parameters for most rock-forming minerals were taken from Palandri and Kharaka (2004), which are based mainly on experimental studies conducted under far-from-equilibrium conditions. The mineral reactive-surface areas were taken from Xu et al. (2007; 2006), based on the work of Sonnenthal et al. (2005). A thorough review and discussion of the kinetic rates for arsenian pyrite, pyrite, and galena was given in Zheng et al. (2009). The kinetic rates for orpiment and realgar were arbitrarily taken to be the same as those for arsenian pyrite. Sensitivity analyses were then conducted to evaluate the importance of these kinetic rates.

Chemical reactions considered in the model include aqueous complexation, mineral dissolution/precipitation, and adsorption/desorption via surface complexation. Tables 5.4 and 5.5 shows the surface complexation of lead and arsenic on different minerals.

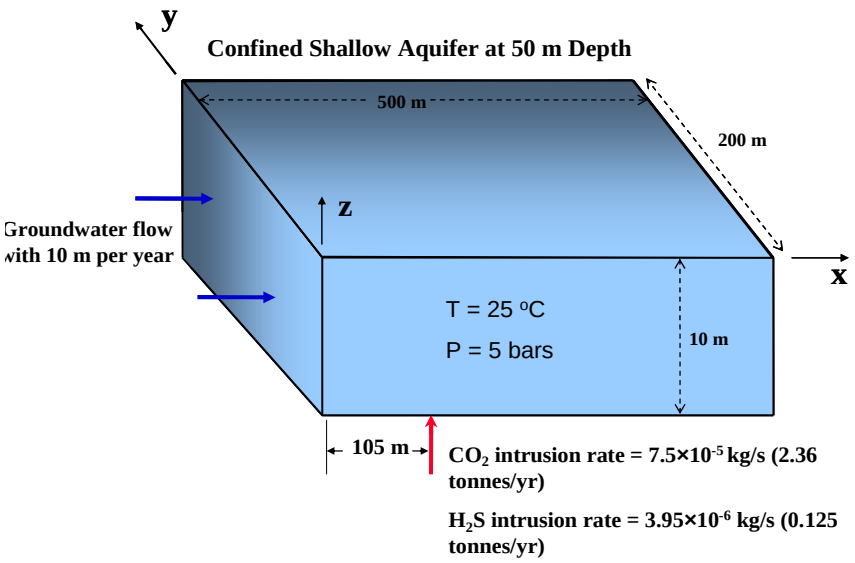

Figure 5.31. Schematic representation for the setup of the reactive transport model

Table 5.1. Hydrodynamic parameters.

Porosity	0.3
Intrinsic permeability	1×10^{-12} m^2 (hydraulic conductivity of ≈ 0.86 m/day)
Relative permeability (van Genuchten-Mualem model)	$k_{rl}=\sqrt{S^*}\left\{1-\left(1-\left[S^*\right]^{1/0.457}\right)^{0.457}\right\}^2$ with $S^*=(S_l-0.3)/(1.0-0.3)$ where S_l is the liquid saturation degree
Gas relative permeability	$k_{rg}=\left(1-\hat{S}\right)^2\left(1-\hat{S}^2\right)$ with $\hat{S}=\left(S_l-0.3\right)/\left(1-0.3-0.05\right)$
Capillary pressure function	$P_{cap}=-\frac{1}{5.1\times10^{-5}}\left(\left[S^*\right]^{-1/0.457}-1\right)^{1-0.457}$ with $S^*=S_l/0.999$ and subject to restriction $-10^7\le P_{cap}\le 0$
Molecular diffusion coefficient	10^{-9} m^2/s

Table 5.2. Initial total aqueous concentration of major constituents obtained by initial equilibrium run for the base model.

Species	Concentration (mol/L)	Species	Concentration (mol/L)
Ca	9×10^{-4}	TIC	3.3×10^{-3}
Mg	2.2×10^{-5}	SO_4^{-2}	1.9×10^{-4}
Na	2×10^{-3}	Cl	2.1×10^{-4}
K	2.7×10^{-4}	Pb	1.3×10^{-9}
Fe	5.6×10^{-6}	As	4.4×10^{-8}
Si	9.3×10^{-4}	ionic strength	0.0051

Table 5.3. Kinetic properties for minerals considered in the model (see text for data sources).

Mineral	A (cm^2/g)	Parameters for Kinetic Rate Law							
		Neutral Mechanism		Acid Mechanism			Base Mechanism		
		k_{25} ($mol/m^2/s$)	E_a (KJ /mol)	k_{25}	E_a	$n(H^+)$	k_{25}	E_a	$n(H^+)$
***Primary*:**									
Quartz	9.8	1.023×10^{-14}	87.7						
K-feldspar	9.8	3.89×10^{-13}	38	8.71×10^{-11}	51.7	0.5	6.31×10^{-12}	94.1	-0.823
Oligoclase	9.8	1.44×10^{-12}	69.8	2.13×10^{-10}	65	0.457			
Kaolinite	151.6	6.91×10^{-14}	22.2	4.89×10^{-12}	65.9	0.777	8.91×10^{-18}	17.9	-0.472
Smectite-Ca	151.6	1.66×10^{-13}	35	1.05×10^{-11}	23.6	0.34	3.02×10^{-17}	58.9	-0.4
Illite	151.6	1.66×10^{-13}	35	1.05×10^{-11}	23.6	0.34	3.02×10^{-17}	58.9	-0.4
Chlorite	9.8	3.02×10^{-13}	88	7.76×10^{-12}	88	0.5			
Kerogen-os	9.8	3.02×10^{-13}	88	7.76×10^{-12}	88	0.5			
Calcite	Assumed at equilibrium								
Goethite	12.9	2.52×10^{-12}	62.76						
Arsenian pyrite	12.9	2.52×10^{-12}	62.76						
Pyrite	12.9	2.52×10^{-12}	62.76						
Galena	12.9			2.34×10^{-7}	43.54	1			
Secondary:									
Dolomite	12.9	2.52×10^{-12}	62.76	2.34×10^{-7}	43.54	1			
Magnesite	9.8	4.57×10^{-10}	23.5	4.17×10^{-7}	14.4	1			
Ankerite	9.8	1.26×10^{-9}	62.76	6.46×10^{-4}	36.1	0.5			
Dawsonite	9.8	1.26×10^{-9}	62.76	6.46×10^{-4}	36.1	0.5			
Smectite-Na	151.6	1.66×10^{-13}	35	1.05×10^{-11}	23.6	0.34	3.02×10^{-17}	58.9	-0.4
Pyromorphite	12.9	2.52×10^{-12}	62.76	2.34×10^{-7}	43.54	1			
Ferroselite	12.9	2.52×10^{-12}	62.76	2.34×10^{-7}	43.54	1			
Orpiment	12.9	2.52×10^{-12}	62.76	2.34×10^{-7}	43.54	1			
Realgar	12.9	2.52×10^{-12}	62.76	2.34×10^{-7}	43.54	1			

Table 5.4. Surface complexation of lead on different minerals.

Adsorbent	Surface Complexes	Reactions	Log k_{int}	Reference
goethite	Goe_OPb^+	$Goe\_OPb^+ + H^+ = Goe\_OH + Pb^{+2}$	0.5	(Muller and Sigg, 1991)
goethite	$(Goe\_O)_2Pb$	$(Goe\_O)_2Pb+2H^+ = 2Goe\_OH + Pb^{+2}$	6.24	
kaolinite	Kao_OPb^+	$Kao\_OPb^+ + H^+ = Kao\_OH + Pb^{+2}$	-1.89	(Hizal and Apak, 2006)
illite	$Ill^s\_OPb^+$	$Ill^s\_OPb^+ + H^+ = Ill^s\_OH + Pb^{+2}$	-1.37	(Gu and Evans, 2007)
illite	$Ill^w\_OPb^+$	$Ill^w\_OPb^+ + H^+ = Ill^w\_OH + Pb^{+2}$	3.84	
smectite	$Sme^s\_OPb^+$	$Sme^s\_OPb^+ + H^+ = Sme^s\_OH + Pb^{+2}$	-1.12	(Bradbury and Baeyens, 2005)
smectite	$Sme^w\_OPb^+$	$Sme^w\_OPb^+ + H^+ = Sme^w\_OH + Pb^{+2}$	1.28	

Table 5.5. Surface complexation of arsenic on different minerals.

Adsorbent	**Surface Complexes**	**Reactions**	**Log k_{int}**	**Reference**
goethite	Goe $\_H_2AsO_3$	Goe $\_H_2AsO_3 + H_2O$ = Goe $\_OH + H_3AsO_3$	-5.19	(Dixit and Hering, 2003)
goethite	Goe $\_HAsO_3^-$	Goe $\_HAsO_3^- + H_2O + H^+$ = Goe$_OH + H_3AsO_3$	2.34	
kaolinite	Kao$_H_2AsO_3$	Kao $\_H_2AsO_3 + H_2O$ = Kao $\_OH + H_3AsO_3$	-8.23	(Manning and Goldberg, 1997)
kaolinite	Kao $\_HAsO_3^-$	Kao$_HAsO_3^- + H_2O + H$ = Kao $\_OH + H_3AsO_3$	0.664	
kaolinite	Kao $\_OAsO_3^{2-}$	Kao$_AsO_3^{2-} + H_2O + 2H^+$ = Kao $\_OH + H_3AsO_3$	13.67	
illite	Ill$_H_2AsO_3$	Ill $\_H_2AsO_3 + H_2O$ = Ill$_OH + H_3AsO_3$	-9.07	(Manning and Goldberg, 1997)
illite	Ill $\_HAsO_3^-$	Ill $\_HAsO_3^- + H_2O + H^+$ = Ill $\_OH + H_3AsO_3$	-3.0	
illite	Ill$_AsO_3^{2-}$	Ill$_AsO_3^{2-} + H_2O + 2H^+$ = Ill$_OH + H_3AsO_3$	10.3	
smectite	Sme $\_H_2AsO_3$	Sme $\_H_2AsO_3 + H_2O$ = Sme $\_OH + H_3AsO_3$	-8.89	(Manning and Goldberg, 1997)
smectite	Sme $\_HAsO_3^-$	Sme $\_HAsO_3^- + H_2O + H^+$ = Sme $\_OH + H_3AsO_3$	4.65	
smectite	Sme $\_AsO_3^{2-}$	Sme $\_AsO_3^{2-} + H_2O + 2H^+$ = Sme $\_OH + H_3AsO_3$	13.7	

5.3.2. *Results of Base-Case Model*

5.3.2.1. Gas Plume

As shown in Figure 5.32, the total mass of the CO_2+H_2S gas mixture intruding into the aquifer is 7.9×10^{-5} kg/s, 95% of which is CO_2 and 5% is H_2S. The total injection rate is slightly higher than the pure-CO_2 injection rate assumed in Zheng et al. (2009); however, the spatial distribution of the gas phase is almost identical to that obtained for the case with pure CO_2. A small two-phase zone appears near the intrusion location (x= 105, y= 0 m) and remains for the 100-year simulation time. At 100 years, CO_2 accounts for 97.5% of the total mass of the compressed "gas" phase present, whereas H_2S accounts for 2.5%, half the injected concentration. The reason for this difference is that H_2S is more soluble in water than CO_2.

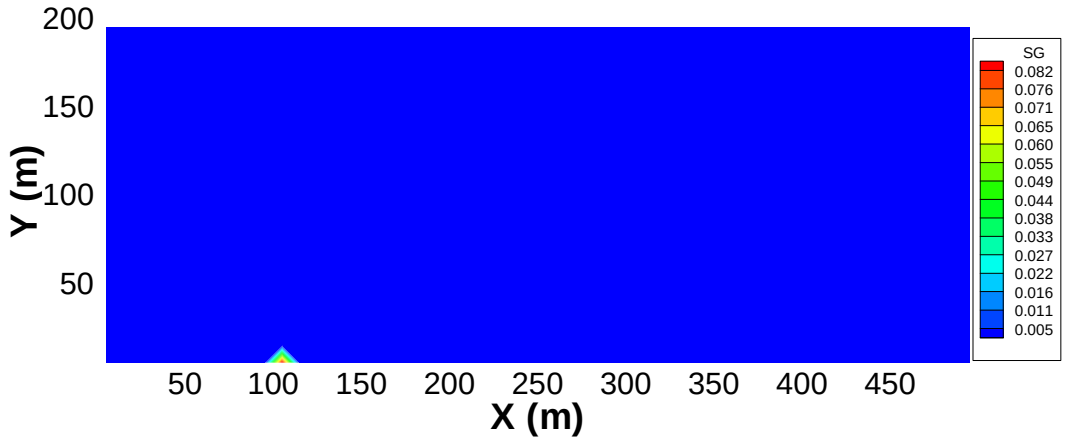

Figure 5.32. Spatial distribution of intruding CO_2+H_2S fluid saturation at 100 years

5.3.2.2. Dissolved Species

Our simulations address the question whether the presence of H_2S in the gas mixture could exacerbate CO_2 impact on shallow groundwater, as far as metal release from sediments. Although the dissolution of H_2S in water increases the acidity of the solution because of deprotonation, as revealed in the following reaction—

$$H_2S(g) = H^+ + HS^- \quad (5.4)$$

the hydrogen ion released is mostly consumed by the dissolution of Fe(III) (hydr)oxides and the precipitation of pyrite, as discussed earlier. As a result, the pH of the groundwater in case of the leakage of an H_2S+CO_2 mixture (Figure 5.33) is very similar to the case of a pure-CO_2 leak. This is consistent with the results presented by Xu et al. (2007).

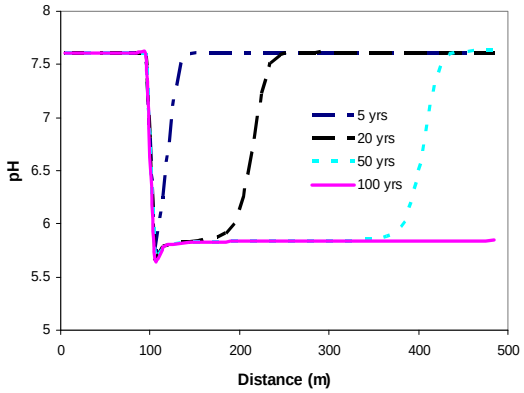

Figure 5.33. pH profile along x at y=0 at different times (the CO_2+H_2S mixture intrudes at x= 105 m)

Ferric iron, i.e., goethite in current simulations, is reduced by hydrogen sulfide as in the following reaction:

$$FeOOH(goethite) + 1.875H^{+} + 0.125HS^{-} = Fe^{+2} + 0.125SO_4^{2-} + 1.5H_2O \qquad (5.5)$$

Initially, the concentration of HS^- peaks (~7 millimolal, Figure 5.34) because of the higher effective rate of goethite dissolution. With time, the rate of reaction (5.5) decreases (as the reaction approaches equilibrium), which, together with the continuing influx of sulfide, results in a buildup of significant sulfide concentrations, although lower than the initial peak levels. Figure 5.35 shows the volume fraction change of goethite at different times as the result of this reaction (negative values indicate dissolution, whereas positive values are signs of precipitation). As would be expected, more goethite dissolution occurs near the intrusion location.

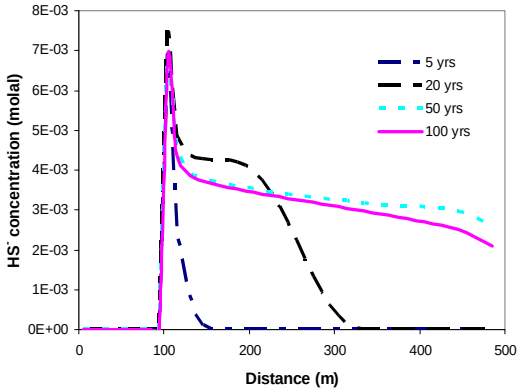

Figure 5.34. Total aqueous sulfide concentration profile (as HS^-) along x at y=0 at different times (the CO_2+H_2S mixture intrudes at x= 105 m).

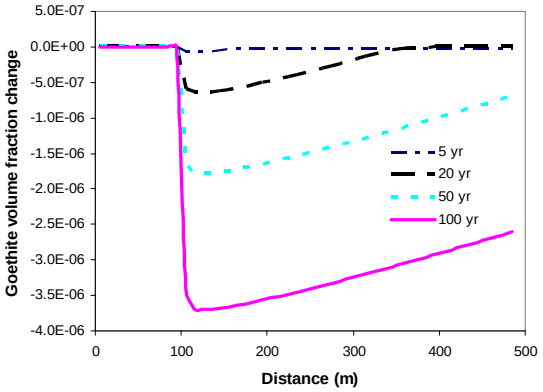

Figure 5.35. Profile of the goethite volume fraction change (dimensionless) along x at y=0 at different times (the CO_2+H_2S mixture intrudes at x= 105 m).

The increase in hydrogen sulfide concentration and production of Fe^{+2} through reaction (5.5) induces the precipitation of pyrite (Figure 5.36). The concentrations of Fe^{+2} are consequently depressed to very low values (Figure 5.37), even though the reduction of goethite supplies Fe^{+2}. This is because the effective dissolution rate of goethite is lower

than that of pyrite. Note that in these simulations, the precipitation of siderite is not observed, contrary to experimental and modeling findings by Palandri and Kharaka (2005). This is mainly because in their study, the abundance of iron oxides and hydroxides are much higher, and correspondingly the effective dissolution rates of these minerals are higher as well. Whether Fe^{+2} precipitates as pyrite preferentially to siderite directly depends on the relative precipitation rates of these minerals, and the rate of precipitation of these minerals relative to the goethite dissolution rate. A sensitivity study described later in this section shows that precipitation of siderite can be observed if the dissolution rate of goethite is increased. As noted earlier, the precipitation of amorphous iron sulfide (FeS) is favored kinetically, but is ignored here (for simplicity), since FeS would eventually be replaced by pyrite.

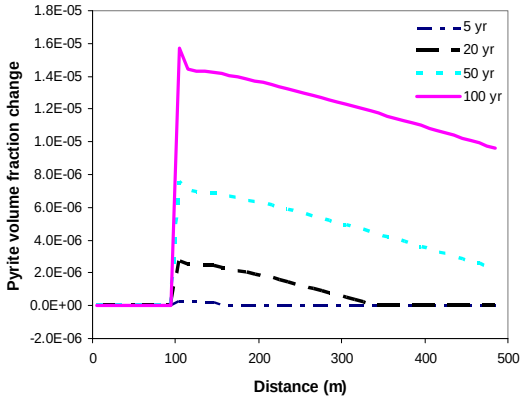

Figure 5.36. Profile of the pyrite volume fraction change (dimensionless) along x at y=0 at different times.

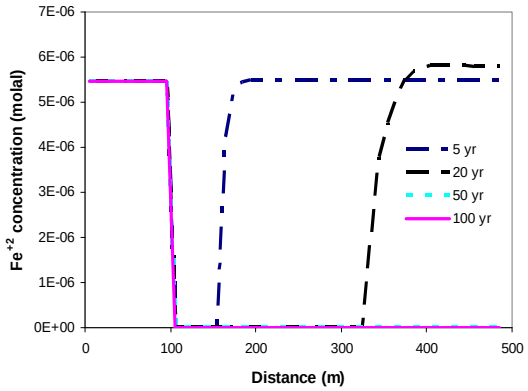

Figure 5.37. Profile of total ferrous iron concentration (as Fe^{+2}) along x at y=0 at different times.

Desorption of lead and the dissolution/precipitation of the lead-bearing mineral galena were found to be the two main chemical processes that control the evolution of lead concentrations in the aqueous phase (Zheng et al., 2009). For intrusion of pure CO_2 (Zheng et al., 2009), the increase in acidity is the main mechanism of lead desorption. For H_2S+CO_2 mixtures, the aqueous complexation of lead with sulfide turns out to be the dominant driving force for desorption of lead, although the increase in acidity still plays a

role. Table 5.6 compares the concentrations of lead aqueous complexes obtained in simulations for intrusion of pure CO_2 and for intrusion of H_2S+CO_2 mixtures. High concentrations of $Pb(HS)_2$(aq) and PbS(aq) observed in the latter case indicate that the aqueous complexation of lead with sulfide dominates over surface complexation. As shown in Figure 5.38, this effect leads to a strong desorption and rapidly depletes lead from all sorption sites.

Table 5.6. Computed speciation of aqueous lead for cases of intrusion of pure CO_2 ("pure CO_2") and H_2S+CO_2 mixture ("H_2S+CO_2") at 3.5 years.

Species	Concentration "Pure CO_2" (molal)	Concentration "H_2S+CO_2" (molal)
$PbCO_3$(aq)	4.4×10^{-9}	4.4×10^{-12}
$Pb(HS)_2$(aq)	1.2×10^{-14}	2.1×10^{-7}
$Pb(HS)_3^-$	1.3×10^{-22}	5.0×10^{-10}
$PbCl^+$	1.8×10^{-12}	7.4×10^{-16}
$PbCl_2$(aq)	9.2×10^{-16}	3.9×10^{-19}
$PbCl_3^-$	9.1×10^{-20}	3.8×10^{-23}
$PbCl_4^{-2}$	1.7×10^{-23}	7.0×10^{-27}
$PbOH^+$	5.8×10^{-12}	3.9×10^{-15}
$Pb(OH)_2$(aq)	9.2×10^{-16}	1.0×10^{-18}
$Pb(OH)_3^-$	6.6×10^{-21}	1.2×10^{-23}
$Pb(CO_3)_2^{-2}$	4.8×10^{-13}	1.2×10^{-15}
PbO(aq)	1.1×10^{-15}	1.2×10^{-18}
$PbHCO_3^+$	7.9×10^{-9}	4.9×10^{-12}
Pb^{+2}	6.1×10^{-10}	2.5×10^{-13}
$Pb(HSe)_2$(aq)	7.7×10^{-22}	1.2×10^{-18}
$Pb(HSe)_3^-$	1.5×10^{-36}	4.4×10^{-30}
PbS(aq)	2.8×10^{-8}	4.0×10^{-6}
PbSe(aq)	1.3×10^{-9}	1.7×10^{-9}

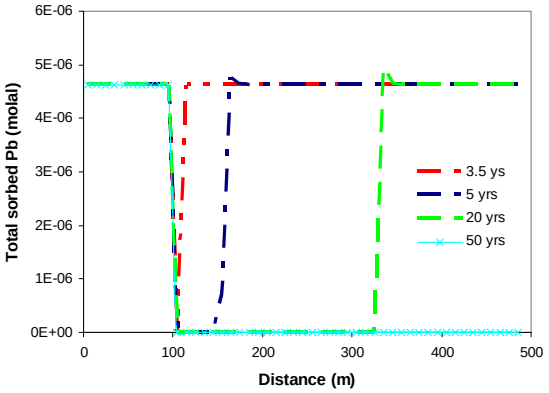

Figure 5.38. Profile of the total sorbed lead along x at y=0 at different times.

In the pure CO_2 intrusion simulation (Zheng et al., 2009), galena precipitation occurred under most simulation conditions due to the release of lead from sorption sites, whereas galena dissolution occurred only when the concentration of sorption sites was very low. In the simulations for H_2S+CO_2 mixtures, the possibility of galena dissolution is essentially ruled out, because the increase in hydrogen sulfide triggers the precipitation of galena regardless of whether lead is released from sorption sites. Figure 5.39 shows the spatial distribution of galena precipitation. Wherever the plume of elevated hydrogen sulfide passes by, galena precipitates.

Figure 5.40 shows the (total) aqueous concentration of lead at different times. The interplay of desorption (increasing aqueous lead concentration) and precipitation of galena (decreasing aqueous lead concentration) controls the spatial distribution of lead. A maximum peak concentration is observed at the intrusion location after 3.5 years, caused by fast (equilibrium) desorption coupled with slower precipitation under kinetic constraints. With time, as the plume of elevated hydrogen sulfide propagates downgradient, the concentrations of lead decrease again to very low values, owing to precipitation of galena with a more-than-sufficient supply of hydrogen sulfide. A peak continues to show only at the tip of the hydrogen sulfide plume, where the precipitation of galena is retarded compared to the fast release of lead from sorption sites. The intensity of this peak, however, decreases with travel distance, to a point at which the lead concentration after 50 or 100 years is just about twice that of the initial concentrations. In summary, the intrusion of H_2S leads to a migrating pulse of elevated lead concentration along the flow path, dynamically controlled by desorption of lead and the precipitation of galena. Model results shows that in the long term (after 50 years), the peak of lead concentration is much lower than the Maximum Contaminants Level (MCL), although it is significantly higher than MCL in the short term (for example, less than 20 years, as shown in Figure 5.40).

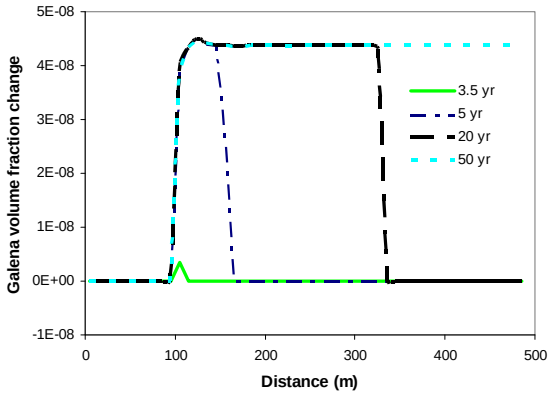

Figure 5.39. Profile of the galena volume fraction change (dimensionless) along x at y=0 at different times

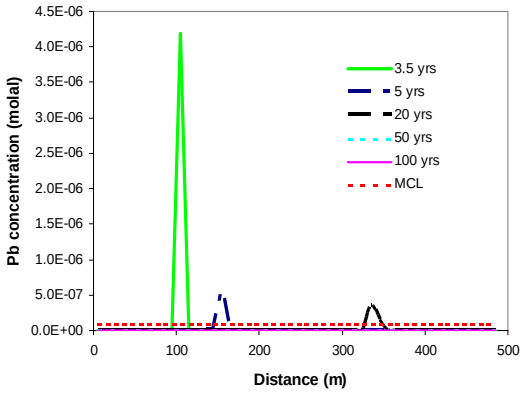

Figure 5.40. Profile of lead concentration along x at y=0 at different times, also shown is the Maximum Contaminants Level (MCL) of lead.

Similar to lead, the aqueous complexation of arsenic with sulfide (instead of the pH change) becomes the predominant driving force for desorption in the case of CO_2+H_2S leakage. Table 5.7 shows the initial mass distribution of Pb and As between solid and liquid phases. More than 99% percent of lead resides initially in mineral form (galena). In contrast, adsorbed arsenic accounts for about 63% of the total initial mass of arsenic, which implies that the desorption of arsenic could have more impact than that of lead. Table 5.8 lists the concentrations of arsenic aqueous complexes obtained in the simulation for CO_2 versus the H_2S+CO_2 mixture. The higher concentrations of $H_2As_3S_6^-$ and $HAs_3S_6^{-2}$ in the latter case indicate that a significant amount of arsenic can be released from sorption sites. Figure 5.41 shows the profile of total adsorbed arsenic concentration and its relative change as a function of time. The relative change in total adsorbed arsenic concentration (i.e., the sum of the concentrations of all arsenic surface complexes) is calculated as:

$$(S^t - S^{ini}) / S^{ini} \tag{5.6}$$

where S^t is the total arsenic concentration on adsorption sites at a given time *t*, and S^{ini} is the initial total arsenic concentration on adsorption sites (both expressed relative to the total amount of water present, in mol/kg_{water}).

As shown in Figure 5.41, desorption is most significant at the intrusion location. A substantial amount of arsenic is released into the aqueous phase and transported downgradient. As a result of the high arsenic concentrations and the elevated sulfide concentrations, both arsenian pyrite and orpiment precipitate (Figure 5.42 and 5.43). The prominent desorption of arsenic results in high concentrations of arsenic in the aqueous phase (Figure 5.44), despite the precipitation of arsenian pyrite and orpiment. However, in this case, orpiment (As_2S_3) is assumed to form at a rather slow rate (Table 5.3). Because elevated As concentration in sulfidic waters are typically limited by orpiment solubility, additional simulations assuming orpiment to form at equilibrium are presented later in this report (Section 5.3.3.2). These simulations show aqueous As concentrations about two orders of magnitude lower than in the present case, although still significantly

above MCL. Furthermore, the amount of metals released from the sediments, and therefore resulting aqueous concentrations, also largely depend on the initial concentration of metals in the sediments (Table 5.7). In the present case, sediments of the shallow aquifer are assumed to contain about 28 ppm of arsenic and 12 ppm of lead (Table 5.7). Average crustal abundance of arsenic and lead is about 2 and 14 ppm, respectively, as summarized in Birkholzer et al. (2008) based on an extensive literature review. Typical concentrations in rock from various areas of the United States were reviewed by Connor and Shacklette (1975), who list 1.1–4.3 ppm As and 5–17 ppm Pb in sandstones, and 6.4–9.0 ppm As and 11–24 ppm Pb in shales. Therefore, in the present study, the assumed abundance of arsenic in sediments is rather high, which would tend to exacerbate the overestimation of As concentrations upon mobilization by H_2S- and CO_2-laden waters.

Table 5.7. Mass distribution (% with respect to the total mass at t = 0) of Pb and As in solid form (in mineral or adsorbed on mineral surfaces) and in the aqueous phase at the start of simulations (initial t = 0)

	Aqueous Phase (%)	Mineral (%)	Adsorbed on goethite (%)	Adsorbed on kaolinite (%)	Adsorbed on illite (%)	Adsorbed on smectite (%)	Total Adsorbed (%)	Total mass (%)	Total sorbed in sediments (ppm)	Total in sediments (ppm)	time
Lead	0.0002	99.12	0.09	0.0002	0.79	0.004	0.89	100.000	0.11	11.6	t=0
Arsenic	0.0001	37.1238	0.08	0.03	55.29	7.48	62.88	100.000	27.6	28.2	t=0

Table 5.8. Computed arsenic speciation for cases of intrusion of pure CO_2 ("pure CO_2") and of a H_2S+CO_2 mixture (base case, "H_2S+CO_2") at 3.5 years.

Species	Concentration "Pure CO_2" (molal)	Concentration "H_2S+CO_2" (molal)
H_3AsO_3(aq)	1.21×10^{-7}	1.91×10^{-8}
$H_2AsO_3^-$	6.43×10^{-11}	1.63×10^{-11}
$H_2AsO_4^-$	1.37×10^{-8}	6.29×10^{-17}
H_3AsO_4(aq)	3.29×10^{-12}	9.45×10^{-21}
$HAsO_4^{-2}$	2.41×10^{-9}	1.76×10^{-17}
$H_3As_3S_6$(aq)	2.91×10^{-35}	5.75×10^{-5}
$H_2As_3S_6^-$	4.56×10^{-33}	3.02×10^{-4}
$HAs_3S_6^{-2}$	3.36×10^{-35}	8.15×10^{-5}

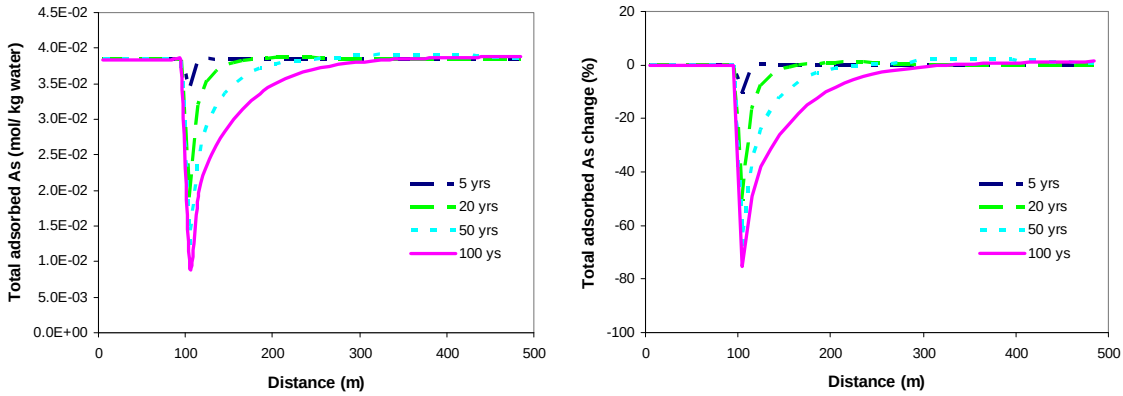

Figure 5.41. Profile of total sorbed arsenic concentrations (left) and relative change in these concentrations (right, see text) along x at y=0 at different times.

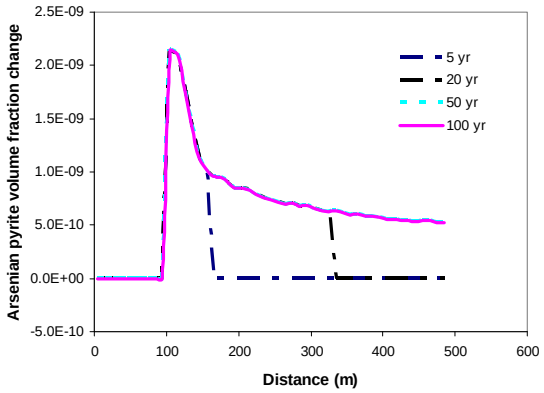

Figure 5.42. Profile of the arsenian pyrite volume fraction change (dimensionless) along x at y=0 at different times.

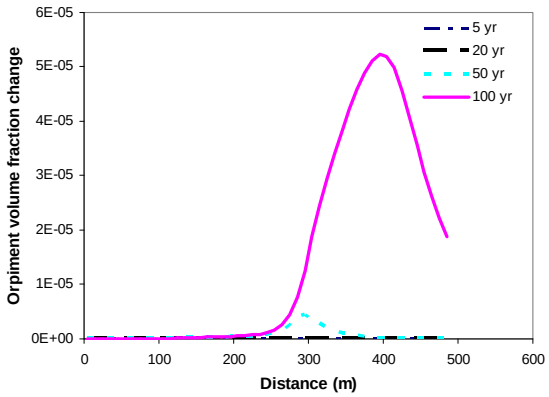

Figure 5.43. Profile of the orpiment volume fraction change (dimensionless) along x at y=0 at different times.

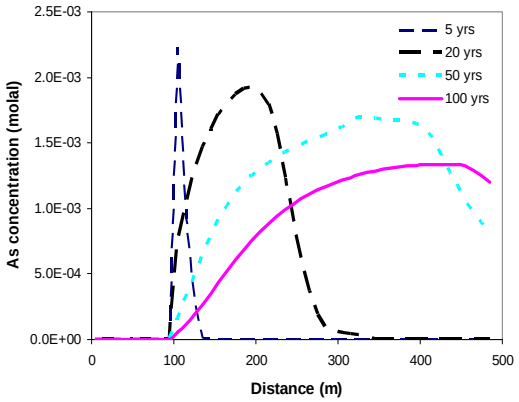

Figure 5.44. Profile of the arsenic concentration along x at y=0 at different times.

5.3.3. *Sensitivity Analysis*

5.3.3.1. Sensitivity to the Kinetic Rate of Goethite Dissolution

Siderite was observed to form in the experiments and geochemical simulations of Palandri and Kharaka (2005), whereas no precipitation of siderite is predicted in our simulations. Their model differs from our model in several aspects, including the pressure and temperature conditions, the abundance of ferric iron, the mineralogy, the composition of the gas mixture, and the mineral dissolution/precipitation kinetic-rate parameters. Most of their simulations were conducted under equilibrium assumptions or using a kinetic rate higher than the value used in the present simulations. Whether siderite precipitates depends on the supply of ferrous iron, which depends on the relative rates of Fe mineral dissolution and precipitation. In Palandri and Kharaka's study, the reduction of hematite (as opposed to goethite in the present study) provides the ferrous iron needed to precipitate siderite. A rate constant on the order of $10^{-9.39}$ mol $m^{-2}s^{-1}$ for hematite dissolution was chosen by these authors, based on Bruno et al. (1992) and Ruan and Gilkes (1995). Although our current simulation assumes goethite instead of hematite, the same kinetic constant is used here for goethite to test how the kinetic rate of iron (hydr)oxides may affect the precipitation of siderite. This corresponds to a rate-constant increase by a factor of almost 40 compared to the base case.

The amount of goethite that dissolves is directly proportional to the dissolution rate of goethite (Figure 5.45). Compared with the results of the base-case model, goethite dissolves at a rate almost two orders of magnitude higher. The precipitation of pyrite, constrained by the supply of Fe^{+2} in the base model, is much more significant in the sensitivity run (Figure 5.46), but more localized around the intrusion location. H_2S is sequestered by pyrite and the propagation of the elevated hydrogen sulfide plume is thus retarded (Figure 5.47). In contrast, Fe^{+2} is not entirely consumed by the precipitation of pyrite, and excess Fe^{+2} (Figure 5.48) precipitates as siderite downgradient (Figure 5.49). Note that the shape of the Fe^{+2} concentrations profiles (Figure 5.48) reflect the balance between the effective rates of Fe mineral dissolution and precipitation. In the base-case

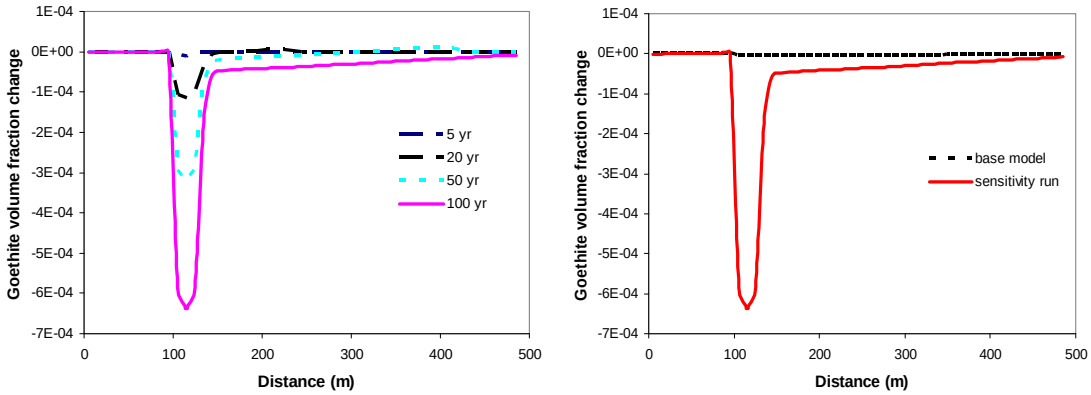

Figure 5.45. Profile of the goethite volume fraction change along x at y=0 at different times (left) and the comparison of the goethite volume fraction change at 100 years between the sensitivity run and base-case model (right).

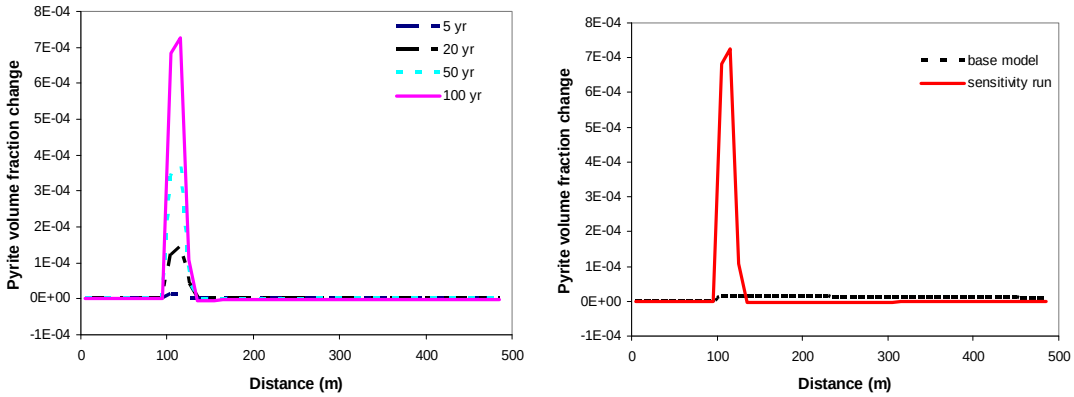

Figure 5.46. Profile of the pyrite volume fraction change along x at y=0 at different times (left) and the comparison of the pyrite volume fraction change at 100 years between the sensitivity run and base-case model (right).

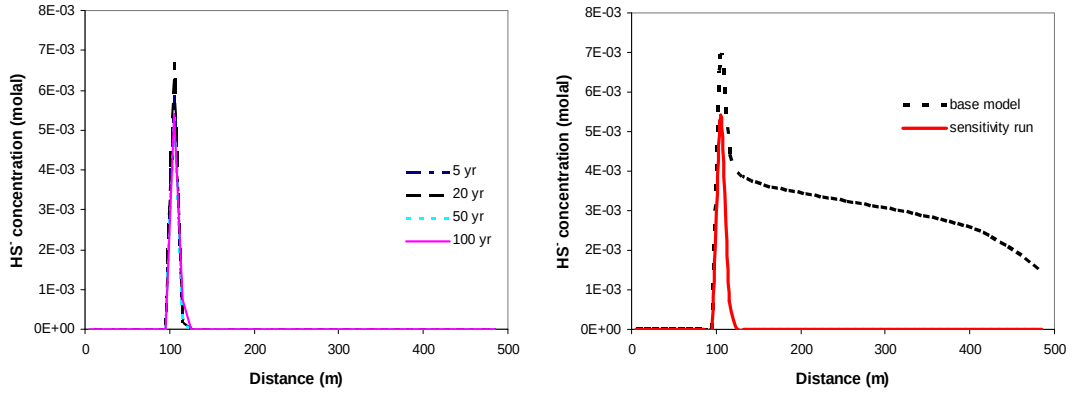

Figure 5.47. Profile of total aqueous sulfide concentration (as HS^-) along x at y=0 at different times (left) and comparison of the ferrous iron concentration at 100 years between the sensitivity run and base-case model (right).

model, the precipitation of pyrite controls the aqueous concentration of Fe^{+2}, whereas in the sensitivity run, the dissolution of goethite (at a higher rate than that in the base-case

model) and precipitation of pyrite concomitantly control the concentration of Fe^{+2} near the CO_2 intrusion location, and the precipitation of siderite controls the concentration of Fe^{+2} downgradient.

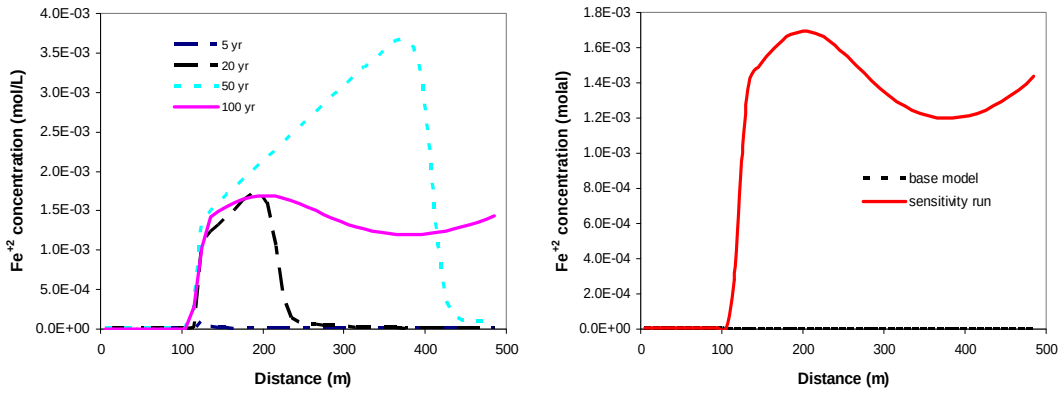

Figure 5.48. Profile of total ferrous iron concentration (as Fe^{+2}) along x at y=0 at different times (left) and the comparison of the ferrous iron concentration at 100 years between sensitivity run and base model (right).

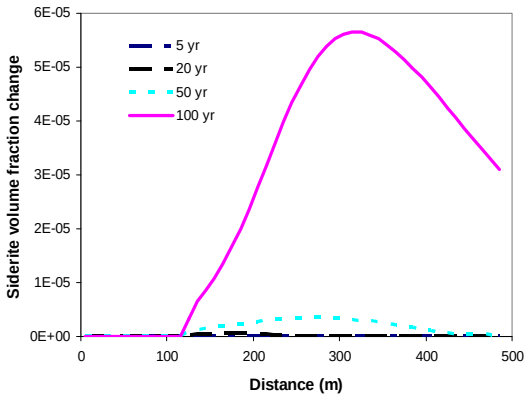

Figure 5.49. Profile of the siderite volume fraction change along x at y=0 at different times.

As revealed in the base-case model, the aqueous complexation of lead or arsenic with sulfide triggers desorption. Because elevated aqueous sulfide concentrations are limited by the precipitation of pyrite near the intrusion location, desorption of lead is also limited to that area (Figure 5.50). Part of the lead released from sorption sites precipitates out as galena (Figure 5.51) and part of it is transported downgradient. The lead transported downgradient partially adsorbs back to the sediment (see the increase of total adsorbed lead in the area adjacent to where desorption happens, in Figure 5.50). As a result, the profile of aqueous lead concentration (Figure 5.52) shows a very small peak in the area of elevated sulfide concentrations (around x=110 m) and a large peak further downgradient resulting from the desorption induced by the lower pH.

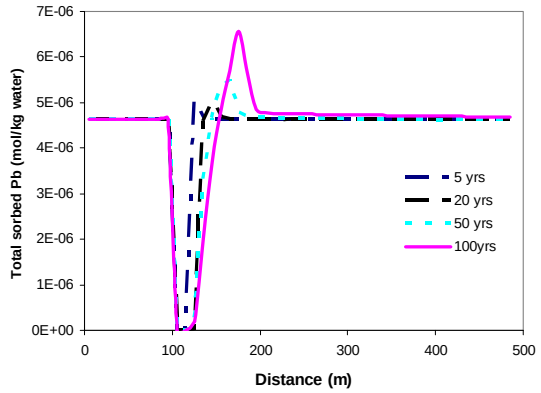

Figure 5.50. Profile of total sorbed lead along x at y=0 at different times.

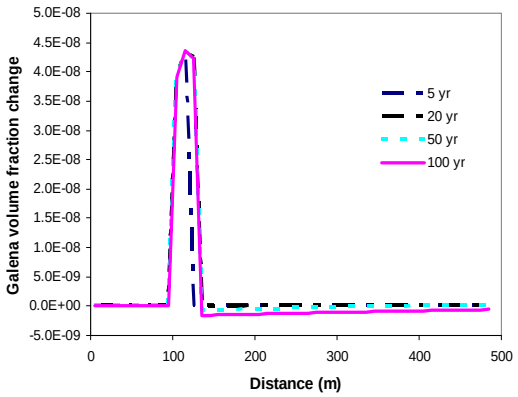

Figure 5.51. Profile of galena volume fraction change along x at y=0 at different times.

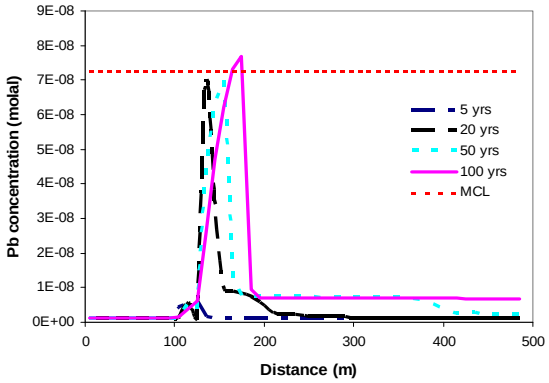

Figure 5.52. Profile of aqueous lead concentration along x at y=0 at different times.

The case with an increased goethite dissolution rate results in a shift in the trends of lead aqueous concentrations with distance, compared to the base case (Figure 5.53). In the base case, a pulse of high lead concentrations is predicted to occur at early times (at 20 years in Figure 5.53 left, with concentrations up to two orders of magnitude higher than MCL), then eventually fades out at later times, yielding rather low lead concentrations (about twice of the initial concentration) after 100 years (Figure 5.53 right). The trend in

the sensitivity run, on the other hand, never reaches a level as high in the base case model, although it remains relatively high (slightly higher than MCL) near the intrusion location, even after 100 years (Figure 5.55 right). This is because H_2S is sequestered by pyrite and the propagation of the elevated hydrogen sulfide plume is thus retarded; the desorption of lead is therefore changed spatially and temporally.

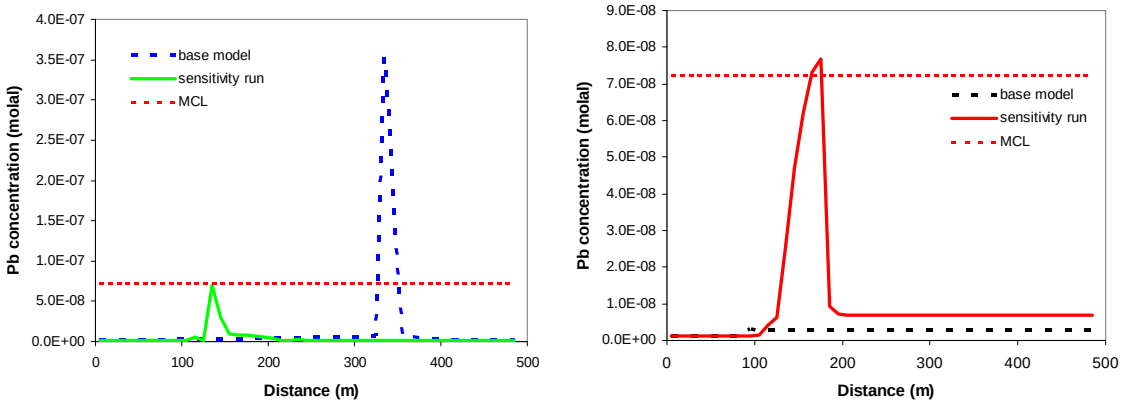

Figure 5.53. Comparison of lead concentration at 20 (left) and 100 years between sensitivity run and base model.

The increased dissolution rate of goethite has a similar effect on the resulting arsenic concentrations. Because elevated aqueous sulfide concentrations are limited to the area adjacent to the intrusion, the extent of arsenic desorption is also limited to this area (see Figure 5.54). While in the base-case run, about 80% of sorbed arsenic is predicted to be released by desorption, almost 100% is predicted to desorb in the sensitivity run (Figure 5.55). Desorption results in elevated arsenic concentrations early on (Figure 5.56), which become limited by the precipitation of arsenian pyrite (Figure 5.57) and decrease significantly over the long run. The aqueous concentrations of arsenic at 100 years are predicted to be about one order of magnitude lower in the sensitivity run compared to the base-case model (Figure 5.58), although arsenic concentrations in both cases are still much higher than the MCL (Figure 5.58, right). This is in part because much more arsenian pyrite precipitates earlier on (Figure 5.57) than in the base case (Figure 5.42), because of the increased supply of Fe^{+2}. Note that the two-peak pattern on the aqueous As concentration profile (Figure 5.58, right) reflects the precipitation of arsenian pyrite earlier on, replaced by the precipitation of orpiment later on. Obviously, these aqueous arsenic concentrations are also in large part dependent on the amount of As present in the sediments (Table 5.7), as well as the precipitation rates of possible As sinks (assumed in this case to consist only of arsenian pyrite and orpiment). As noted earlier, the initial As concentrations in the sediments may be untypically high (~ 28 ppm), and the precipitation rate of orpiment is untypically slow, thus resulting in aqueous As concentrations that are atypically elevated.

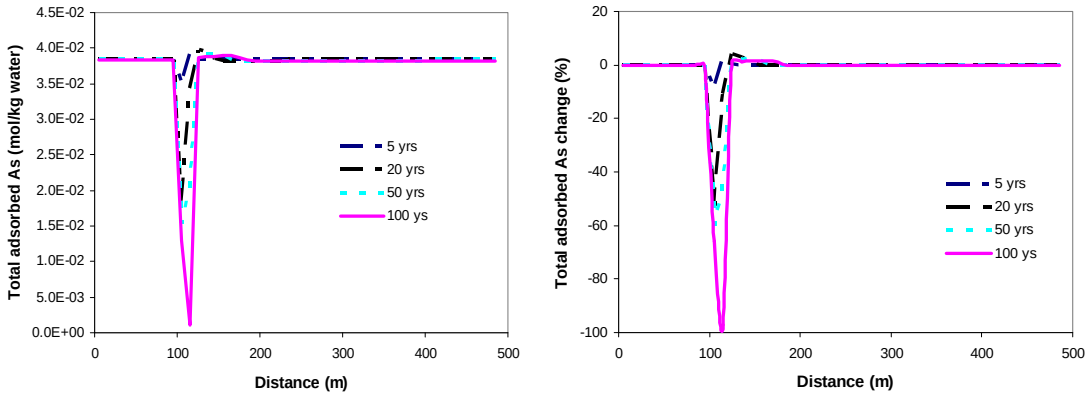

Figure 5.54. Profile of the total sorbed arsenic (left) and the relative change (right) along x at y=0 at different times

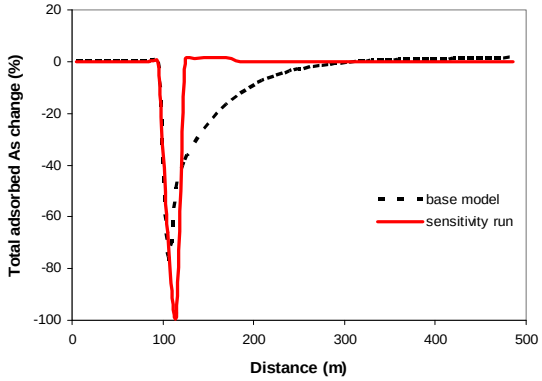

Figure 5.55. Comparison of total adsorbed arsenic change at 100 years for the sensitivity run and base-case model.

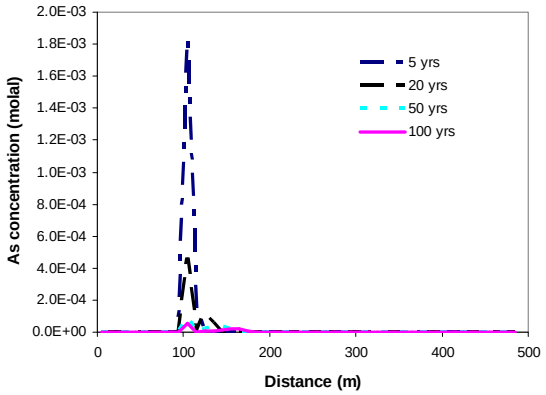

Figure 5.56. Profile of arsenic concentration along x at y=0 at different times.

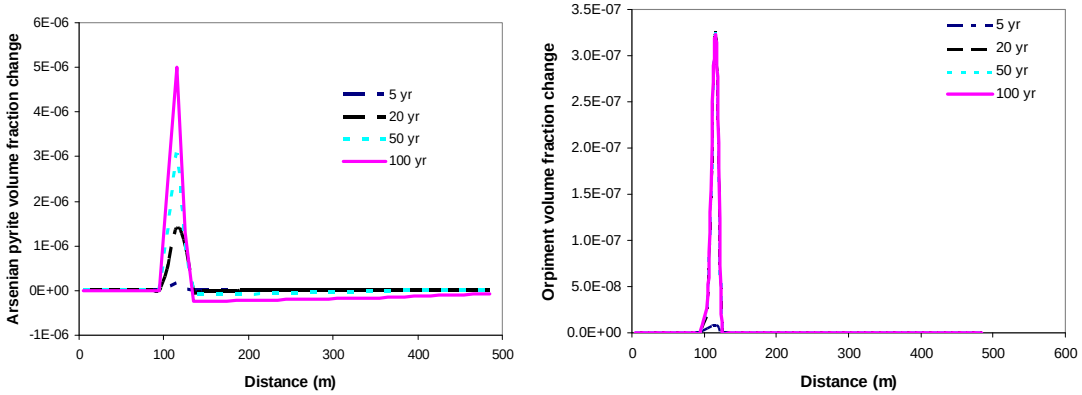

Figure 5.57. Profile of arsenian pyrite (left) and orpiment (right) volume fraction change along x at y=0 at different times.

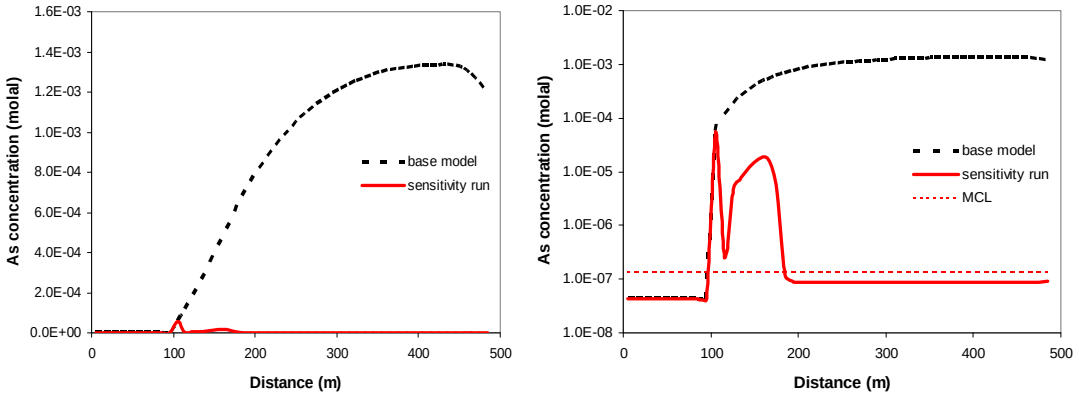

Figure 5.58. Comparison of the ferrous iron concentration at 100 years for the sensitivity run and base-case model. The Y axis on the left figure is linear, and the Y axis on the right figure is logarithmic. The MCL for arsenic is also shown in the right figure.

5.3.3.2. Sensitivity to the Kinetic Rate of Orpiment

The kinetic rates of chemical reactions, especially in complex systems, pose a great source of uncertainty for any geochemical model. Given these uncertainties, our current simulations are intended to provide a qualitative evaluation of the possible chemical processes undertaken during the intrusion of H_2S+CO_2 mixture; they cannot provide a quantitative prediction of mobilization of relevant chemical species. In the base-case model, a kinetic rate constant of 2.6×10^{-12} mol $m^{-2}s^{-1}$ is assumed for orpiment, which is rather slow given the fact that orpiment is typically observed to readily precipitate from natural sulfidic waters with elevated As concentrations (e.g., White, 1981; Ballantyne and Moore, 1988). Therefore, in this sensitivity run, orpiment is assumed to react at equilibrium, which represents the upper bound of reaction rate, to examine how the precipitation of orpiment affects the concentration of arsenic.

The assumption that orpiment reacts at equilibrium gives rise to a much larger amount of precipitated orpiment (Figure 5.59). As a result, a significant amount of H_2S is trapped in orpiment, and the downgradient transport of aqueous sulfide is retarded (Figure 5.60). Another consequence is that arsenic released from sorption sites is consumed by orpiment precipitation, which causes the aqueous concentration of arsenic to be much lower (Figure 5.61) than in the base case, although arsenic concentrations still remain significantly above the MCL.

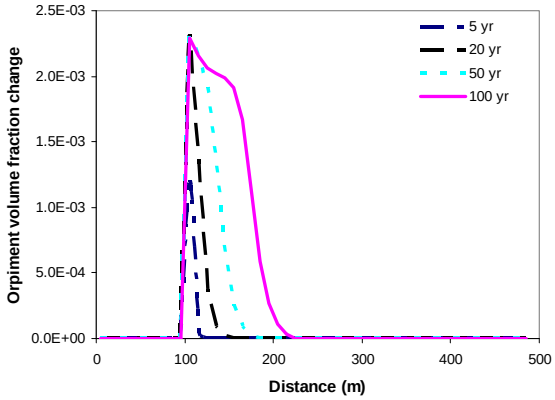

Figure 5.59. Profile of orpiment volume fraction change along x at y=0 at different times.

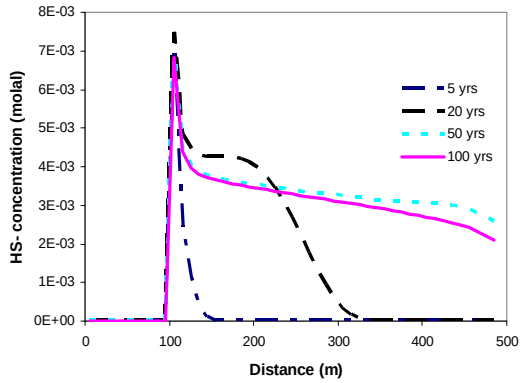

Figure 5.60. Profile of hydrogen sulfide concentration along x at y=0 at different times.

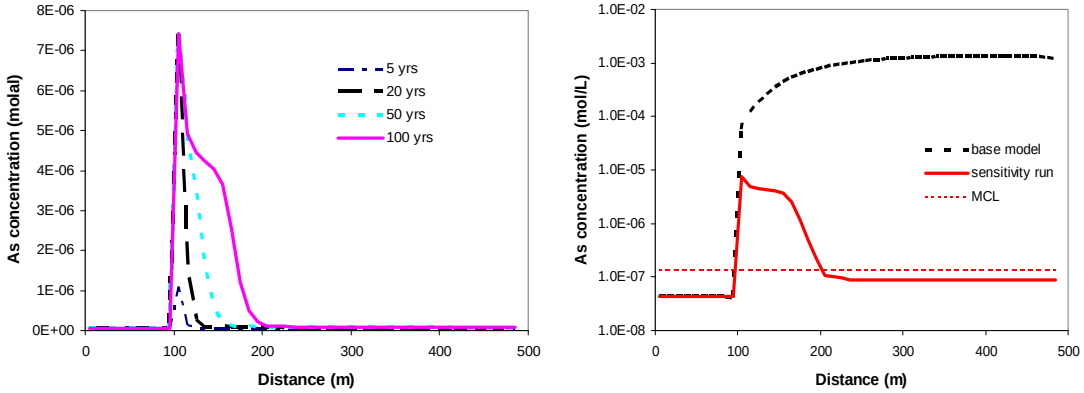

Figure 5.61. Profile of the arsenic concentration along x at y=0 at different times (left) and the comparison of the arsenic concentration at 100 years between the sensitivity run and base-case model (right); note that the Y axis on the left figure is linear, and the Y axis on the right figure is logarithmic.

5.3.3.3. Sensitivity to Intrusion Rate of H_2S

In the base-case model, the intrusion rate of H_2S gas is 3.95×10^{-6} kg/s, which accounts for 5% of the total mass of gas. Considering the fact that the mass of H_2S could vary significantly, we conducted a sensitivity run with an intrusion rate of 7.9×10^{-7} kg/s, five times smaller than in the base case and representing about 1% of the total mass intruded. The smaller H_2S gas intrusion rate results in roughly proportionally lower concentrations of dissolved H_2S. Figure 5.62 (right) shows the concentration of aqueous sulfide predicted in the sensitivity run and base-case model. The aqueous sulfide concentrations predicted in the sensitivity run are lower and more restricted in the lateral direction. Even though the concentration of sulfide drops, the aqueous complexation of lead with sulfide still induces enough desorption to significantly deplete lead from sorption sites (Figure 5.63). However, the area with depleted sorption sites is not as laterally extensive as in the base case. As discussed in Section 5.3.2, lead released from sorption sites mostly precipitates as galena, except directly adjacent to the downgradient edge of the desorption zone, where both aqueous sulfide and lead concentrations peak. A comparison of model results of lead concentration at 5 years (Figure 5.64) shows that the concentration peak in the sensitivity run is slightly higher and closer to the intrusion location.

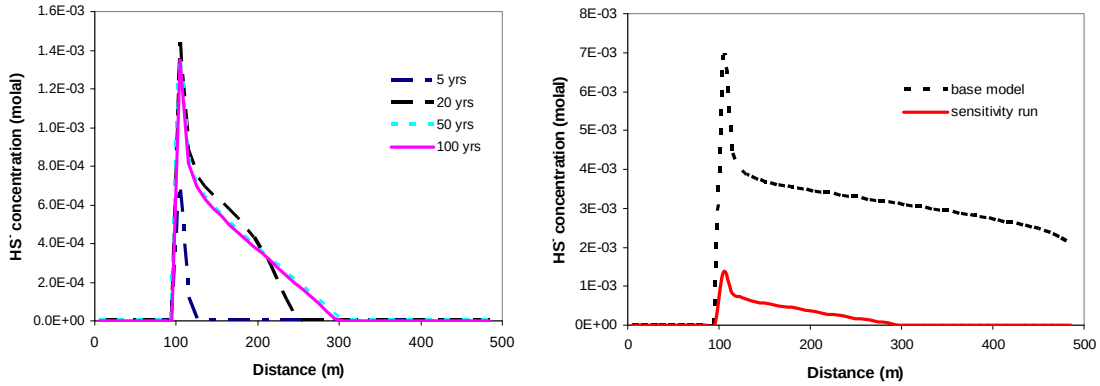

Figure 5.62. Profile of the hydrogen sulfide concentration along x at y=0 at different times (left) and the comparison of the hydrogen sulfide concentration at 100 years between sensitivity run and base model (right).

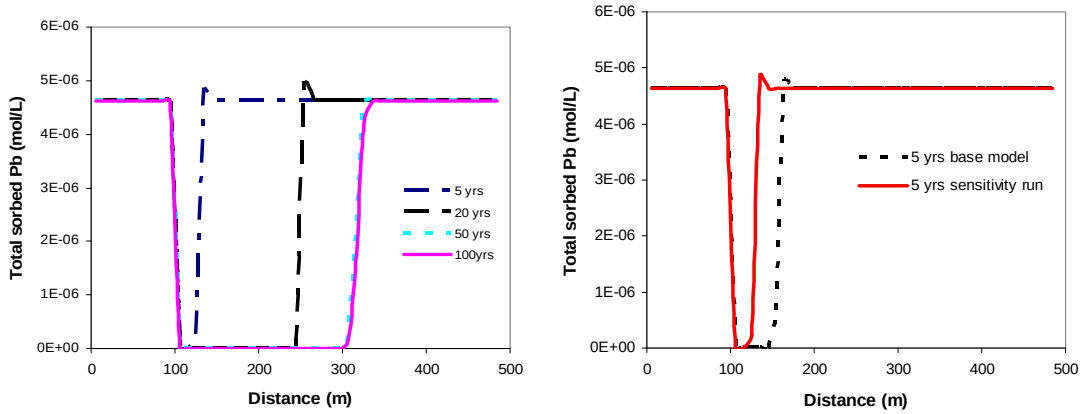

Figure 5.63. Profile of the total adsorbed lead along x at y=0 at different times (left) and comparison of the total adsorbed lead at 5 years between the sensitivity run and base-case model (right).

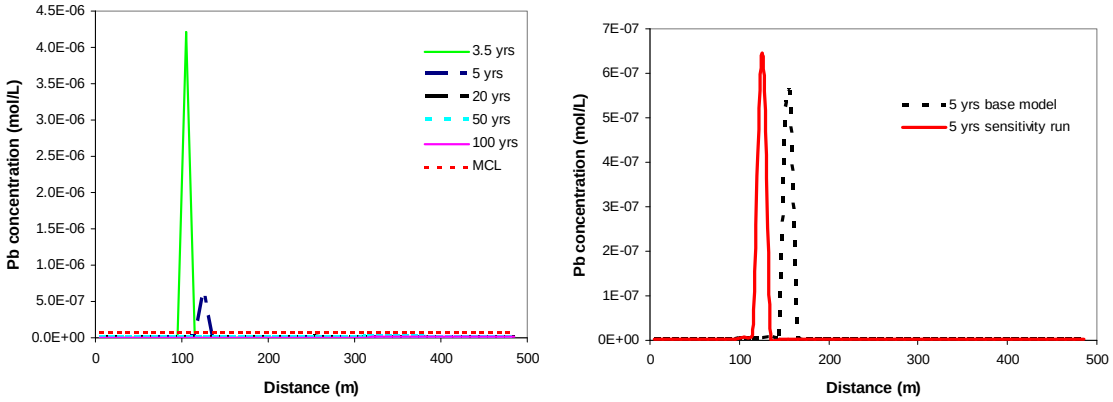

Figure 5.64. Profile of the lead concentration along x at y=0 at different times (left) and comparison of the lead concentration at 100 years between the sensitivity run and base-case model (right).

Contrary to what is predicted for lead (i.e., when lower sulfide concentrations do not significantly affect lead desorption), the lower sulfide concentrations do result in less arsenic desorption (Figure 5.65). In the sensitivity run, only 20% of sorbed arsenic is released after 100 years at the intrusion location, whereas in the base-case run, about 80% of sorbed arsenic is released (Figure 5.65, right). As a result, the aqueous concentration of arsenic is much lower in the sensitivity run (Figure 5.66). This occurs despite the fact that initial concentrations of adsorbed arsenic are much higher than those of adsorbed lead (Table 5.7), and results from the comparatively stronger surface complexation (relative to aqueous complexation with sulfide) for arsenic than for lead.

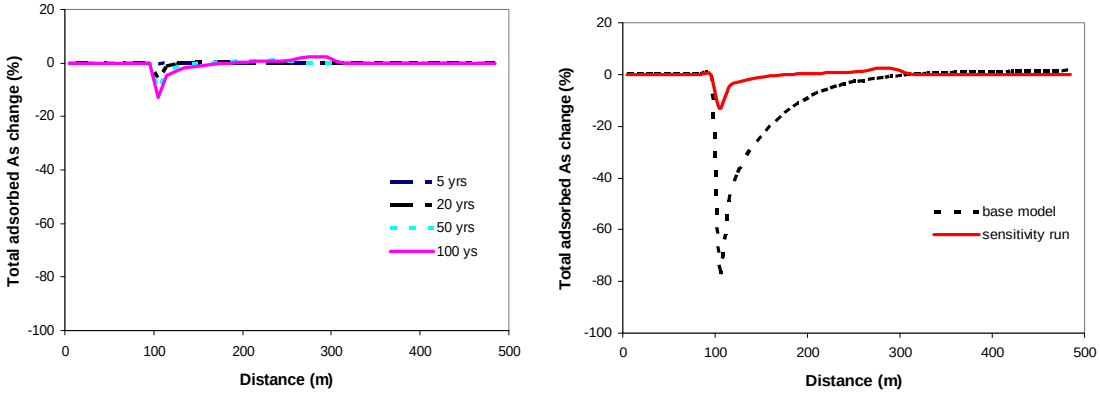

Figure 5.65. Profile of total adsorbed arsenic concentration change (%) along x at y=0 at different times (left) and comparison of the total adsorbed arsenic concentration change at 100 years between the sensitivity run and base-case model (right).

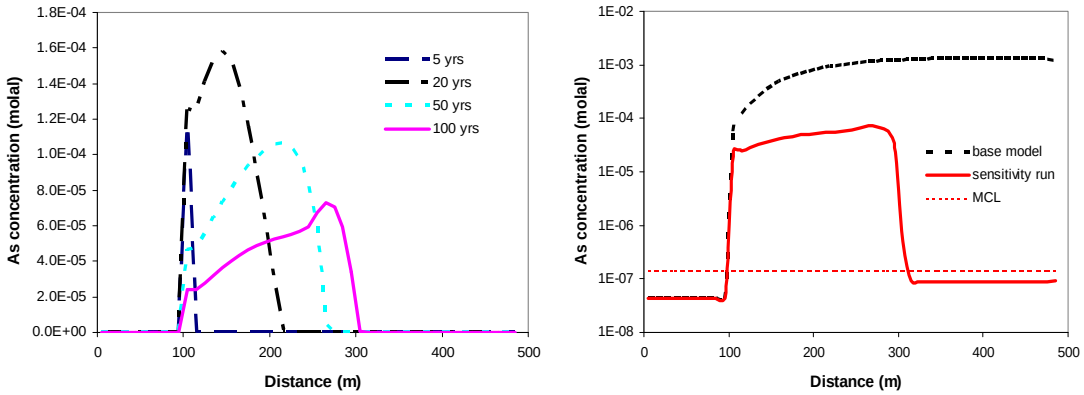

Figure 5.66. Profile of aqueous arsenic concentrations along x at y=0 at different times (left) and comparison of the total adsorbed arsenic change at 100 years between the sensitivity run and base model (right). Note that the Y axis on the left figure is linear, and the Y axis on the right figure is logarithmic.

6. Summary and Conclusions

In this study, reactive transport simulations were used to assess the mobilization and transport of organics with supercritical CO_2 (SCC), and the co-injection and transport of H_2S with SCC. These processes were evaluated at conditions of typical storage reservoirs, and for cases of hypothetical leakage from a reservoir to an overlying shallower fresh water aquifer. Modeling capabilities were developed to allow the simulation of multiphase flow and transport of H_2O, CO_2, H_2S, as well as specific organic compounds (benzene), coupled with multicomponent geochemical reaction and transport. This included the development of a new simulator, TMVOC-REACT, starting from existing modules of the TOUGH2 family of codes. This work also included an extensive literature review, calculation, and testing of phase-partitioning properties for mixtures of the phases considered.

The reactive transport simulations presented in this report are primarily intended to illustrate the capabilities of the new simulator. They are also intended to help evaluate and understand various processes at play, in a more qualitative than quantitative manner, and only for hypothetical scenarios. Therefore, model results are not intended as realistic assessments of groundwater quality changes for specific locations, and they certainly do not provide an exhaustive evaluation of all possible site conditions, especially given the large variability and uncertainty in hydrogeologic and geochemical parameter input into simulations.

The first step in evaluating the potential mobilization and transport of organics was the identification of compounds likely to be present in deep storage formations, and likely to negatively impact freshwater aquifers if mobilized by SCC. On the basis of a literature review related to the occurrence of these organic compounds, their solubility in water and SCC, and their toxicity (as reflected by their maximum contaminant levels MCL), benzene was selected as a key compound for inclusion into numerical simulations. Note that considering additional organic compounds and/or mixtures of such compounds in the simulations was beyond the scope of this study, because of the effort required to research, calculate, and validate the phase-partitioning data necessary for simulations.

The injection of CO_2 into a deep saline aquifer was simulated, followed by modeling the leaching of benzene by SCC and transport of benzene to an overlying aquifer along a hypothetical leakage pathway. One- and two-dimensional models were set up for this purpose. The target storage formation was assumed to initially contain about 10^{-4} ppm benzene. Model results indicate that:

1. SCC efficiently extracts benzene from the storage formation.
2. Assuming equilibrium, the content of benzene in SCC is proportional to the concentration of benzene in the aqueous and solid phases.
3. Benzene may co-migrate with CO_2 into overlying aquifers if a leakage pathway is present. Because the aqueous solubility of benzene in contact with CO_2 is lower

than the aqueous solubility of CO_2, benzene is actually enriched in the CO_2 phase as the plume advances.
4. For the case studied here, the resulting aqueous benzene concentration in the overlying aquifer is on the same order of magnitude as the initial concentration in the storage formation.

This generic modeling study illustrates, in a semi-quantitative manner, the possible mobilization of benzene by SCC. The extent to which the mobilization of this organic compound evolves temporally and spatially depends on a large number of controlling parameters and is largely site specific. Therefore, for more "truly" predictive work, further sensitivity studies should be conducted, and further modeling should be integrated with site-specific laboratory and/or field experimental data.

The co-injection of H_2S with CO_2 into a deep saline aquifer was also simulated. In addition, the model considered leakage of the supercritical CO_2+H_2S mixture along a preferential pathway to an overlying fresh-water aquifer, followed by reaction of the CO_2+H_2S mixture with that aquifer. A simple 2-D model that included a storage formation and a sealing aquitard was developed to simulate the movement of H_2S in a typical CO_2 storage formation. Model results indicate that H_2S is stripped off at the edge of the advancing supercritical plume, because of the H_2S preferential solubility in water compared to CO_2. The magnitude of H_2S preferential dissolution, however, decreases with decreasing temperature and pressure. To capture this behavior and evaluate the breakthrough of H_2S through a leakage pathway (from the deep storage formation to a shallower aquifer), another model was constructed, considering a storage formation, an overlying aquifer, and a vertical leakage pathway between them. Model results suggest that:

1. Leakage pathways may allow co-migration of CO_2+H_2S despite the preferential dissolution (stripping) of H_2S at the edge of the advancing CO_2+H_2S plume.
2. There is some delay between the CO_2 and H_2S times of arrival (into the shallow aquifer) caused by H_2S preferential dissolution, but this effect does not last very long.
3. Once this stripping effect ceases, H_2S co-migrating with CO_2 is predicted to enter the aquifer at about the same concentration as in the CO_2 stream injected into the deep formation.

Simulations have also been conducted to evaluate the possible geochemical evolution of a freshwater aquifer in response to the leakage of a H_2S+CO_2 mixture. In addition to the adverse effects of H_2S itself (i.e., odor and taste), the leakage of H_2S (in addition to CO_2) is likely to exacerbate impacts on shallow groundwater. Possible geochemical reactions induced by the leakage of a H_2S+CO_2 mixture are as follows:

1. Desorption of lead and arsenic, mainly due to aqueous complexation with sulfide, could lead to increased concentrations of aqueous lead and arsenic.
2. The precipitation of pyrite (and/or FeS) could partly mitigate elevated aqueous sulfide concentrations, or could even sequester a large portion of the injected

sulfide if there were a sufficient amount of ferrous iron supplied in the aquifer, either produced by the reduction of Fe(III) (hydr)oxides, or present in other minerals.

3. The reductive dissolution of Fe(III) (hydr)oxides could produce significant amounts of ferrous iron, and may therefore be critical for dampening the adverse effects of sulfide by precipitation of pyrite. However, the precipitation of siderite may compete with sulfide for ferrous iron. Whether siderite precipitates depends on the relative rates of Fe mineral dissolution and precipitation, and on other conditions such as temperature and pressure.
4. The desorption of arsenic is accompanied by the precipitation of arsenian pyrite and orpiment. The precipitation of these minerals dampens aqueous arsenic concentrations, although these concentrations remain fairly high in sulfidic waters.

Acknowledgment

We thank the US Environmental Protection Agency, Office of Water and Office of Air and Radiation, for funding this study under an Interagency Agreement with the U.S. Department of Energy at the Lawrence Berkeley National Laboratory, Contract No. DE-AC02-05CH11231.

References

Aiuppa, A., C. Federico, P. Allard, S. Gurrieri and M. Valenza, 2005. Trace metal modeling of groundwater-gas-rock inter-actions in a volcanic aquifer: Mount Vesuvius, Southern Italy. Chemical Geology, 216: 289-311.

Ambats, G., J.A. Apps, S. Beers, J.T. Birkholzer, K.S. Gullickson, W.N. Herkelrath, E. Kakouros, Y.K. Kharaka, L.H. Spangler, N. Spycher, J. Thordsen and L. Zheng, 2009. Groundwater chemistry changes as a result of CO_2 injec-tion at the ZERT field site in Bozeman, Montana. Project Report LBNL-2931E, Lawrence Berkeley National Laboratory.

Amoore J.E., and E. Hautala, 1983. Odor as an aid to chemical safety: Odor thresholds compared with threshold limit values and volatilities for 214 chemicals in air and water dilution. J. Appl. Toxicol. 3(6):272-290.

Anderson, F.E. and J.M. Prausnitz, 1986. Mutual solubilities and vapor pressure for binary and ternary aqueous systems containing benzene, toluene, m-xylene, thiophene and pyridine in the rigion 100-200 °C. Fluid Phase Equilibria, 32: 63-67.

Anitescu, G. and L.L. Tavlarides, 2006. Supercritical extraction of contaminants from soils and sediments. J. of Supercritical Fluids, 38: 167-180.

Appelo, C.A.J., M.J.J. Van Der Weiden, C. Tournassat and L. Charlet, 2002. Surface complexation of ferrous iron and carbonate on ferrihydrite and the mobilization of arsenic. Environ. Sci. Technol., 36(14): 3096-3103.

Apps, J. A., Zheng, L., Zhang, Y., Xu, T. and Birkholzer, J. T., 2010. Evaluation of groundwater quality changes in response to CO2 leakage from deep geological storage. Transport in Porous Media 82(1): 215-246.

Bachu, S., 2000. Sequestration of CO_2 in geological media: criteria and approach for site selection in response to climate change. Energy Conv. Manag., 42: 953–970.

Bachu, S. and D.B. Bennion, 2009. Chromatographic partitioning of impurities contained in a CO_2 stream injected into a deep saline aquifer: Part 1. Effects of gas composition and in situ conditions. International Journal Of Greenhouse Gas Control, 3(4): 458-467.

Bachu, S., M. Pooladi-Darvish and H.F. Hong, 2009. Chromatographic partitioning of impurities (H2S) contained in a CO_2 stream injected into a deep saline aquifer: Part 2. Effects of flow conditions. International Journal Of Greenhouse Gas Control 3(4): 468-473.

Baldi, F. and R. Bargagli, 1982. Chemical leaching and specific surface area measurements of marin sediments in the evaluation of mercury contaminations near cinnabar deposits. Marin Environmental Research.

Ballantyne, J.M. and J.N. Moore, 1988. Arsenic geochemistry in geothermal systems. Geochimica et Cosmochimica Acta, 52(2): 475-483

Bartle, K.D., A.A. Clifford, S.A. Jafar and G.F. Shilstone, 1991. Solubilities of solids and liquids of low volatility in supercritical carbon dioxide. J. Phys. Chem. Ref. Data 20(4): 713-756.

Bendale, P.G. and R.M. Enick, 1994. Use of carbon dioxide to shift benzenelacetonitrile and benzene/cyclohexane azeotropes. Fluid Phase Equilibria, 94: 227-253.

Benson, B.B. and D. Krause, 1976. Empirical laws for dilute aqueous solutions of nonpolar gases. J. Chem. Phys., 64: 689-709.

Bierlein, J.A. and W.B. Kay, 1953. Phase-equilibrium properties of system carbon dioxide-hydrogen Sulfide. Ind. Eng. Chem., 45: 618-624.

Birkholzer, J.T., J.A. Apps, L. Zheng, Y. Zhang, T. Xu and C.-F. Tsang., 2008. Research project on co_2 geological storage and groundwater resources: water quality effects caused by co_2 intrusion into shallow groundwater. Technical Report LBNL-1251E, Lawrence Berkeley National Laboratory, Berkeley, CA.

Bondor, P.L., 1992. Applications of carbon dioxide in enhanced oil recovery. Energy Conversion & Management 33(5-8): 579-586.

Bradbury, M. H. and B. Baeyens, 2005. Modelling the sorption of Mn(II), Co(II), Ni(II), Zn(II), Cd(II), Eu(III), Am(III), Sn(IV), Th(IV), Np(V) and U(VI) on montmorillonite: Linear free energy relationships and estimates of surface binding constants for some selected heavy metals and actinides. Geochimica et Cosmochimica Acta, 69(4): 875-892.

Brudi, K., N. Dahmen and H. Schmieder, 1996. Partition coefficients of organic substances in two-phase mixtures of water and carbon dioxide at pressures of 8 to 30 mpa and temperatures of 313 to 333 K. The Journal of Supercritical Fluids, 1996(3): 146-151.

Bruno, J., W. Stumm, P. Wersin and F. Brandberg, 1992. On the influence of carbonate in mineral dissolution: 1. The thermodynamics and kinetics of hematite dissolution in bicarbonate solutions at T=25 ^{o}C. Geochim. Cosmochim. Acta, 56: 1139-1147.

Buckley, S.E., C.R. Hocott and M.S. Taggart, Jr., 1958. Distribution of dissolved hydrocarbons in subsurface waters. In: L.G. Weeks (Editor), Habitat of Oil. Am. Assoc. Petrol. Geologists, Tulsa, Okla., pp. 850-882.

Burgess, M.P. and R.P. Germann, 1969. Physical properties of hydrogen sulfide water mixtures. AIChE J., 15: 272-275.

Canadian Environmental Quality Guidelines for the Protection of Aquatic Life, 1999. Canadian Council of Ministers of the Environment, Winnipeg.

Carroll, J.J. and A.E. Mather, 1989. The solubility of hydrogen sulfide in water from 0 to 90°C and pressures to 1 MPa. Geochimica et Cosmochimica Acta 53: 1163-1170.

Carroll, S., 2009. Trace metal release from Frio Sandstone re-acted with CO_2 and 1.5N NaCl brine at 60 oC, Eighth Annual Carbon Capture & Sequestration Conference, Pittsburgh, PA.

Chandler, K., B. Eason, C.L. Liotta and C.A. Eckert, 1998. Phase equilibria for binary aqueous systems from a near-critical water reaction apparatus. Ind. Eng. Chem. Res., 37: 3515-3518.

Chapoy, A., A.H. Mohammadi and B. Tohidi, 2005. Experimental measurement and phase behavior modeling of hydrogen sulfide-water binary system. Ind. Eng. Chem. Res., 44: 7567-7574.

Chen, H. and J. Wagner, 1994. An apparatus and procedure for measuring mutual solubilities of hydrocarlions + water: benzene + water from 303 to 373 K. J. Chem. Eng. Data, 39: 470-474.

Chiou, C.T., V.H. Freed, D.W. Schmedding and R.L. Kohnert, 1977. Partition coefficients and bioaccumulation of selected organic chemicals. Environ. Sci. Technol., 11(5): 475-478.

Connolly, J.F., 1966. Solubility of hydrocarbons in water near the critical solution temperatures. Journal of Chemical and Engineering data, 11(1): 13-16.

Connor J.J and H.T. Shacklette, 1975. Background geochemistry of some rocks, soils, plants and vegetables in the conterminous United States. U.S. Geological Survey Professional Paper 574-F (168 pp.)

D'Amore, F. and A.H. Truesdell, 1988. A review of solubilities and equilibrium constants for gaseous species of geothermal interest. Sci. Geol. Bull., 41: 309-332.

Deeds, N.E., D.C. McKinney and G.A. Pope, 2000. Laboratory characterization of non-aqueous phase liquid/tracer interaction in support of a vadose zone partitioning interwell tracer test. J. Contaminant Hydrol., 41: 193-204.

Denbigh, K., 1983. The principles of chemical equilibrium. Cambridge University Press, Cambridge, UK.

Dixit, S. and J.G. Hering, 2003. Comparison of arsenic(v) and arsenic(iii) sorption onto iron oxide minerals: implications for arsenic mobility. Environ. Sci. Technol. 37: 4182-4189.

Donahue, R.B., S.L. Barhour and J.V. Headley, 1999. Diffusion and adsorption of benzene in Regina clay. Can. Geotech. J., 36(3): 430-442.

dos Ramos, M.C. and C. Clare McCabe, 2010. Modeling the phase behavior, excess enthalpies, and Henry's constants of the H_2O+H_2S binary mixture using the SAFT-VR+D approach. Fluid Phase Equilibria, 290, 137–147.

Doughty, C. and K. Pruess, 2005. Modeling supercritical carbon dioxide injection in heterogeneous porous media. Vadose Zone Journal, 3(3): 837-847.

Drummond, S.E., 1981. Boiling and mixing of hydrothermal fluids: Chemical effects on mineral precipitation., Pennsylvania State University, PA.

Duan, Z., R. Sun, R. Liu and C. Zhu, 2007. Accurate thermodynamic model for the calculation of h_2s solubility in pure water and brines. Energy & Fuels, 21: 2056-2065.

Francis, A.W., 1954. Ternary systems of liquid carbon dioxide. Journal of Physical chemistry, 58: 1099-1114.

Freund, H. and S.R. Kelemen, 1989. Low-temperature pyrolysis of Green River kerogen. AAPG Bulletin, 73: 1011-1017.

Furutaka, S. and S.-I. Ikawa, 2001. Effect of temperature and pressure on a water–benzene mixture as studied by infrared spectroscopy. Fluid Phase Equilibria, 185: 379-387.

Ghonasgi, D., S. Gupta, K.M. Dooley and F.C. Knopf, 1991. Supercritical CO_2 extraction of organic contaminants from aqueous streams. AIChE J., 37.

Gilespie, P.C., L.J. Owens and G.M. Wilson, 1984. Sour water equilibria extended to high temperature and with inerts present. AIChE Winter National Meeting. Paper no. 34b, Atlanta, GA.

Green, L.A. and A. Akgerman, 1996. Supercritical co_2 extraction of soil-water slurries. The Journal of Supercritical Fluids, 9(3): 177-184.

GSPA, 2004. Engineering Data Book, I & II. Gas Processors Suppliers Association, Tulsa, Oklahoma.

Gu, X. and L.J. Evans, 2007. Modelling the adsorption of Cd(II), Cu(II), Ni(II), Pb(II), and Zn(II) onto Fithian illite. Journal of Colloid and Interface Science 307, 317-325.

Gunter, W.D., E. H. Perkins and I. Hutcheon, 2000. Aquifer disposal of acid gases: modeling of water-rock reactions for trapping of acid wastes. Appl. Geochem. 15 (8), 1085–1095.

Gunter, W.D., A. Pratt, B.E. Buschkuehle and E.H. Perkins, 2005. Acid gas injection in the Brazeau Nisku Q carbonate reservoir: Geochemical reactions as a result of the injection of an H_2S-CO_2 waste stream. Greenhouse Gas Control Technologies 7, 469-477

Gupta, M.K., Y.H. Li, B.J. Hulsey and R.L. Robinson Jr., 1982. Phase equilibrium for carbon dioxide-benzene at 313.2, 353.2, and 393.2 K. J. Chem. Eng. Data, 27(1): 55-57.

Hauthal, W.H., 2001. Advances with supercritical fluids [review]. Chemosphere, 43: 123-135.

Hawthorne, S.B. and D.J. Miller, 2003. Evidence for very tight sequestration of BTEX compounds in manufactured gas plant soils based on selective supercritical fluid extraction and soil/water partitioning. Environ. Sci. Technol., 37: 3578-3594.

Hefter, G.T., 1989. Hydrocarbons with water and seawater: part 1, hydrocarbon C_5 to C_7; Part 2, Hydrocarbon C_8 to C_{36} In: D.G. Shaw (Editor), Solubility data series. pergamon, Oxford.

Hizal, J. and R. Apak, 2006. Modeling of copper(II) and lead(II) adsorption on kaolinite-based clay minerals individually and in the presence of humic acid. Journal of Colloid and Interface Science 295, 1-13.

Illiassov, P.A. and A. Datta-Gupta, 2002. Field-scale characterization of permeability and saturation distribution using partitioning tracer tests: the Ranger Field, Texas. SPE Journal, 7(4): 409-420.

Inel, Y. and R. Iseri, 1997. The octanol-water partition coefficient of benzene derivatives based on three dimensional structure directed molecular properties. Chemosphere, 35(5): 993-1002.

Jacquemet, N., J. Pironon and J. Saint-Marc, 2008. Mineralogical changes of a well cement in various H_2S-CO_2 (-brine) fluids at high pressure and temperature. Environ. Sci. Technol., 42: 282-288.

Jean, J.-S., C.-L. Tsai, S.-H. Ju, C.-W. Tsao and S.-M. Wang, 2002. Biodegradation and transport of benzene, toluene, and xylenes in a simulated aquifer: comparison of modelled and experimental results. Hydrological Processes, 16: 3151-3168.

Jou, F.-Y. and A.E. Mather, 2003. Liquid-liquid equilibria for binary mixtures of water + benzene, water + toluene, and water + p-xylene from 273 K to 458 K. J. Chem. Eng. Data, 48: 750-752.

Kamath, G. and J.J. Potoff, 2006. Monte Carlo predictions for the phase behavior of H2 S+n-alkane, H_2 S+CO_2, CO_2+CH_4 and H_2 S+CO_2+CH_4 mixtures. Fluid Phase Equilibria, 246(1-2): 71-78.

Karickhoff, S.W., D.S. Brown and T.A. Scott, 1979. Sorption of hydrophobic pollutants on natural sediments. Water Research, 13(3): 241-248.

Kharaka, Y.K. and J.S. Hanor, 2007. Deep fluids in the continents: I. sedimentary basins. In: J.I. Drever (Editor), Surface and Ground Water, Weathering and Soils. Elsevier, Treatise on Geochemistry, pp. 1-48.

Kharaka, Y.K., J.J. Thordsen, E. Kakouros, G. Ambats, W.N. Herkelrath, S.R. Beers, J.T. Birkholzer, J.A. Apps, N.F. Spycher, L. Zheng, R.C. Trautz, H.W. Rauch and K.S. Gullickson, 2010, Changes in the chemistry of shallow groundwater related to the 2008 injection of CO_2 at the ZERT field site, Bozeman, Montana. Environmental Earth Sciences, v. 60, p. 273-264. DOI: 10.1007/s12665-009-0401-1

Kim, C.-H., P. Vimalchand and M.D. Donohue, 1986. Vapor-liquid equilibria for binary mixtures of carbon dioxide with benzene, toluene and p-xylene. Fluid Phase Equilibria, 31: 299-311.

Knauss, K.G., J.W. Johnson and C.I. Steefel, 2005. Evaluation of the impact of CO_2, co-contaminant gas, aqueous fluid and reservoir rock interactions on the geologic sequestration of CO_2. Chemical Geology, 217: 339-350.

Koschel, D., J.-Y. Coxam and V. Majer, 2007. Enthalpy and solubility data of H_2S in water at conditions of interest for geological sequestration. Ind. Eng. Chem. Res., 46: 1421-1430.

Koschel, D., J.-Y. Coxam, L. Rodier and V. Majer, 2006. Enthalpy and solubility data of CO_2 in water and NaCl(aq) at conditions of interest for geological sequestration. Fluid Phase Equilibria, 247: 107-120.

Kraemer, T.F. and D.F. Reid, 1984. The occurrence and behavior of radium in saline formation water of the U.S. gulf coast region. Isotope Geoscience, 2: 153-174.

Kulp, J.L. and D.R. Carr, 1952. Surface Area of Deep-Sea Sediments. The Journal of Geology, 60(2): 148-159.

Larsen, T., P. Kjeldsen and T.H. Christensen, 1992. Correlation of benzene, 1,1,1-trichloroethane, and naphthalene distribution coefficient to the characteristics of aquifer materials with low organic carbon content. Chemosphere, 24(8): 979-991.

Lay, E.N., V. Taghikhani and C. Ghotbi, 2006. Measurement and correlation of CO_2 solubility in the systems of CO_2 + Toluene, CO_2 + Benzene, and CO_2 + n-Hexane at near-critical and supercritical conditions. J. Chem. Eng. Data, 51: 2197-2200.

Lee, J.I. and A.E. Mather, 1977. Solubility of hydrogen-sulfide in water. Berichte der bunsen-gesellschaft-physical chemistry. Chemical Physics, 81(10): 1020-1023.

Mackay, D., A. Bobra and W.Y. Shiu, 1980. Relationships between aqueous solubility and octanol water partition coefficients. Chemosphere, 9: 701-711.

Mackay, D. and W.Y. Shiu, 1977. Aqueous solubility of polynuclear aromatic hydrocarbons. Journal of Chemical and Engineering Data, 22(4): 399-401.

Mackay, D., Y.S. Wan and C.M. Kuo, 1992. Illustrated handbook of physical-chemical properties and environmental fate for organic chemicals. Volume 1. Monoaromatic hydrocarbons, chlorobenzenes, and PCBs. Lewis Boca Raton, 697 pp.

Manning, B.A. and S. Goldberg, 1997. Adsorption and stability of Arsenic(III) at the clay mineral-water interface. Environ. Sci. Technol. 31, 2005-2011.

Marche, C., H. Delepine, C. Ferronato and J. Jose, 2003. Apparatus for the on-line gc determination of hydrocarbon solubility in water: benzene and cyclohexane from 70 °C to 150 °C. J. Chem. Eng. Data, 48(2): 398-401.

McAuliffe, C., 1969. Determination of dissolved hydrocarbons in subsurface brines. Chemical Geology, 4: 225-233.

McGrath, A.E., G.L. Upson and M.D. Caldwell, 2007. Evaluation and mitigation of landfill gas impacts on cadmium leaching from native soils. Ground Water Monitoring & Remediation, 27 (99-109).

Miller, D.J. and S.B. Hawthorne, 2000. Solubility of liquid organics of environmental interest in subcritical (hot/liquid) water from 298 K to 473 K. J. Chem. Eng. Data, 45: 78-81.

Miller, D.J., S.B. Hawthorne, A.A. Clifford and S. Zhu, 1996. Solubility of polycyclic aromatic hydrocarbons in supercritical carbon dioxide from 313 K to 523 K and Pressures from 100 bar to 450 bar. J. Chem. Eng. Data, 41: 779-786.

Morris, J.S. and C.H. Byers, 1991. Near-critical-region equilibria of the CH_4-CO_2-H_2S system. Fltid Phase Equilibria, 66(291-308).

Moridis, G.J., M.B. Kowalsky, and K. Pruess, 2008. TOUGH+HYDRATE v1.0 user's manual: a code for the simulation of system behavior in hydrate-bearing geologic media, Report LBNL-00149E, Lawrence Berkeley National Laboratory, Berkeley, CA.

Muller, B. and L. Sigg, 1991. Adsorption of lead(ll) on the goethite surface: voltammetric evaluation of surface complexation parameters. Journal of Colloid and Interface Science 148(2), 517-532.

Murphy R., K. Lammers, A. Smirnov, M.A.A. Schoonen and D.R. Strongin, 2010. Ferrihydrite phase transformation in the presence of aqueous sulfide and supercritical CO_2. Chemical Geology 271: 26–30.

Neely, B.J., J. Wagner, R.L.Robinson Jr. and K.A.M. Gasem, 2008. Mutual solubility measurements of hydrocarbon–water systems containing benzene, toluene, and 3-methylpentane. J. Chem. Eng. Data., 53: 165-174.

Orbey, H. and S.I. Sandler, 1998. Modeling vapor-liquid equilibria: cubic equations of state and their mixing rules. Cambridge University Press.

Ohgaki, K. and T. Katayama, 1976. Isothermal vapor-liquid equilibrium data for binary systems containing carbon dioxide at high pressures: methanol-carbon dioxide, n-hexane-carbon dioxide, and benzene-carbon dioxide systems. Journal of Chemical and Engineering Data, 21(1): 53-55.

Palandri, J. and Y.K. Kharaka, 2004. A compilation of rate parameters of water-mineral interaction kinetics for application to geochemical modeling. Open File Report 2004-1068, US Geological Survey.

Palandri, J.L. and Y.K. Kharaka, 2005. Ferric iron-bearing sediments as a mineral trap for CO_2 sequestration: Iron reduction using sulfur-bearing waste gas. Chemical Geology, 217: 351-364.

Palandri, J.L. and M.H. Reed, 2001. Reconstruction of in situ composition of sedimentary formation waters. Geochim. Cosmochim. Acta, 65: 1741-1776.

Palandri, J.L., R.J. Rosenbauer and Y.K. Kharaka, 2005. Ferric iron in sediments as a novel CO_2 mineral trap: CO_2–SO_2 reaction with hematite. Applied Geochemistry, 20: 2038-2048.

Pfohl, O., P. Avramova and G. Brunner, 1997. Two- and three-phase equilibria in systems containing benzene derivatives, carbon dioxide, and water at 373.15 K and 10-30 MPa. Fluid Phase Equilibria, 141: 179-206.

Pohl, H.A., 1961. Thermodynamics of the hydrogen sulfide-water system relevant to the dual temperature process for the production of heavy water. J. Chem. Eng. Data., 6(4): 515-521.

Poling, B.E., 2007. Perry's Chemical Engineer's Handbook, 8th Edition, Section 2: Physical and Chemical Data. McGraw-Hill Professional

PouIson, S.R., J.I. Drevefi and P.J.S. Colbergh, 1997. Estimation of Koc values for deuterated benzene, toluene, and ethylbenzene, and application to groundwater contamination studies. Chemosphere, 35(10): 2215-2224.

Prausnitz, J.M., R.N. Lichtenthaller and E.G.D. Azedevo, 1986. Molecular thermodynamics of fluid phase equilibria. Prentice Hall, New York

Pruess, K., 2005. ECO2N: A TOUGH2 Fluid property module for mixture of water, NaCl, and CO_2. LBNL-57592, Lawrence Berkeley National Laboratory, Berkeley, CA.

Pruess, K. and A. Battistelli, 2002. TMVOC, a numerical simulator for three-phase non-isothermal flows of multicomponent hydrocarbon mixtures in saturated–unsaturated heterogeneous media, Lawrence Berkeley National Laboratory, Berkeley, CA.

Pruess, K., C. Oldenburg and G. Moridis, 1999. TOUGH2 user's guide, version 2.0. LBL-43134, Lawrence Berkeley National Laboratory, Berkeley, CA.

Reagan, M.T. and C.M. Oldenburg, 2006. WebGasEOS v1.0 User Guide, LBNL-3188, (June 2006).

Reed M.H. and N.F. Spycher, 1985. Boiling, cooling, and oxidation in epithermal systems: a numerical approach. Rev. Econ. Geol. 2: 249-272.

Reid, R.C., J.M. Prausnitz and B.E. Poling, 1987. The properties of gases and liquids. McGraw-Hill, Inc.

Robinson, D.B. and J.A. Bailey, 1957. The carbon dioxide—hydrogen sulfide—methane system. Part I. Phase behavior at 100°F. Can. J. Chem. Eng. , 35: 151-158.

RøeUtvik, T.I., 1999. Chemical characterization of produced water from four offshore oil production platforms in the North Sea. Chemosphere, 39: 2593–2606.

Ruan, H.D. and R.J. Gilkes, 1995. Acid dissolution of synthetic aluminous goethite before and after transformation to hematite by heating. Clay Miner., 30: 55–65.

Sakoda, N. and M. Uematsu. 2004. A thermodynamic property model for fluid phase hydrogen sulfide. International Journal of Thermophysics, 25 (3), May.

Sanemasa, I., M. Araki, T. Deguchi and H. Nagai, 1982. Solubility measurements of benzene and the alkylbenzenes in water by making use of solute vapor. Bull. Chem. Soc. Jpn, 55: 1054-1062.

Sanemasa, I., Y. Miyazaki, S. Arakawa, M. Kumamaru and T. Deguchi, 1987. Solubility benzene-hydrocarbon binary mixture in water. Bull. Chem. Soc. Jpn, 60: 517-523.

Selleck, F.T., L.T. Carmichael and B.H. Sage, 1952. Phase Behavior in the Hydrogen Sulfide-Water System. Ind. Eng. Chem., 44(9): 2219-2226.

Shock, E.L. and H.C. Helgeson, 1990. Calculation of the thermodynamic and transport properties of aqueous species at high pressures and temperatures: Standard partial molal properties of organic species. Geochimica et Cosmochimica Acta, 54: 915-945.

Silin, D., T. Patzek and S. Benson, 2009. A model of buoyancy-driven two-phase countercurrent fluid flow. Transport in Porous Media, 76(3): 449-469.

Sirivedhin, T. and L. Dallbauman, 2004. Organic matrix in produced water from the Osage-Skiatook Petroleum Environmental Research site, Osage county, Oklahoma. Chemosphere, 57 463–469.

Slaine, D.D. and J.F. Barker, 1990. The detection of naturally occuring BTX during a hydrogeologic investigation. Ground Water Monitoring & Remediation, 10(2): 89-94.

Smyth, R.C., S.D. Hovorka, J. Lu, K.D. Romanak, J.W. Partin, C. Wong and C. Yang, 2009. Assessing risk to fresh water resources from long term CO_2 injection – laboratory and field studies. Energy Procedia, 1(1957-1964).

Smyth, T.J., R.G. Zytner and W.H. Stiver, 1999. Influence of water on the supercritical fluid extraction of naphthalene from soil. Journal of Hazardous Materials, 67(2): 183-196.

Sonnenthal, E., A. Ito, N. Spycher, M. Yui, J. Apps, Y. Sugita, M. Conrad and S. Kawakami, 2005. Approaches to modeling coupled thermal, hydrological, and chemical processes in the Drift Scale Heater Test at Yucca Mountain. Int. J. Rock Mech. Min. Sci., 42: 6987–719.

Spycher, N. and K. Pruess, 2005. CO_2-H_2O mixtures in the geological sequestration of CO_2. II. Partitioning in chloride brines at 12–100°C and up to 600 bar. Geochimica et Cosmochimica Acta, 69(13): 3309-3320.

Spycher, N., K. Pruess and J. Ennis-King, 2003. CO_2-H_2O mixtures in the geological sequestration of CO_2. I. Assessment and calculation of mutual solubilities from 12 to 100°C and up to 600 bar. Geochimica et Cosmochimica Acta, 67(16): 3015-3031.

Spycher, N. and M.H. Reed, 1989. Evolution of a broadlands-type epithermal ore fluid along alternative P-T paths: implications for the transport and deposition of base, precious, and volatile metals. Economic Geology, 84: 328-359.

Suleimenov, O.M. and R.E. Krupp, 1994. Solubility of hydrogen sulfide in pure water and NaCl solutions,from 20 to 320 ^{o}C and at saturation pressures. Geochimica et Cosmochimica Acta, 58(11): 2433 - 2444.

Tang, J.S., 2005. Extended Brigham model for residual oil saturation measurement by partitioning tracer tests. SPE Journal, 10(2): 175-183.

Tsonopoulos, C., 2001. Thermodynamic analysis of the mutual solubilities of hydrocarbons and water. Fluid Phase Equilibria, 186: 185-206.

Van Leer, R.A.V. and M.E. Paulaitis, 1980. Solubilities of phenol and chlorinated phenols in supercritical carbon dioxide. Journal of Chemical and Engineering Data, 25(3): 257-259.

Wagner, J., 1999. Engineering data book revitalization and maintenance water-hdyrocarbon mutual solubility data. GPA Research Report RR-169, Gas processors associations, Tulsa, OK.

Walas, S.M., 1985. Phase equilibria in chemical engineering. Butterworth-Heinemann, 671 pp.

White, D.E., 1981. Active geothermal systems and hydrothermal ore deposits. Econ. Geol. 75th Anniv. Vol., 392-423.

Whitehouse, B.G. and R.C. Cooke, 1982. Estimating the aqueous solubility of aromatic hydrocarbons by high performance liquid chromatography. Chemosphere, 11: 689-699.

Wilhem, E., R. Battino and R. Wilcock, 1977. Low-pressure solubility of gases in liquid water. Chem. Rev., 77: 219–262.

Witter, A.E. and A.D. Jones, 1999. Chemical characterization of organic constituents from sulfide-rich produced water using gas chromatography/mass spectrometry. Environ. Toxicol. Chem., 18: 1920-1926.

Xia, J., A.P.-S. Kamps, B. Rumpf and G. Maurer, 2000. Solubility of hydrogen sulfide in aqueous solutions of the single salts sodium sulfate, ammonium sulfate, sodium chloride, and ammonium chloride at temperatures from 313 to 393 K and total pressures up to 10 MPa. Ind. Eng. Chem. Res. , 39: 1064-1073.

Xu, T., Apps, J. A. and Pruess, K., 2005. Mineral sequestration of carbon dioxide in a sandstone–shale system. Chemical Geology, 217: 195-318.

Xu, T., J.A. Apps, K. Pruess and H. Yamamoto, 2007. Numerical modeling of injection and mineral trapping of CO_2 with H_2S and SO_2 in a sandstone formation. Chemical Geology, 242: 319-346.

Xu, T. and Pruess, K., 2008. Numerical studies on enhanced CO_2 dissolution and mineral trapping due to formation of aqueous complexes. Computational Methods in Water Resources. San Francisco, California.

Xu, T., E. Sonnenthal, N. Spycher and K. Pruess, 2006. TOUGHREACT: a simulation program for non-isothermal multiphase reactive geochemical transport in variably saturated geologic media. Computers and Geosciences, 32: 145-165.

Xu, T., N. Spycher, E. Sonnenthal, G. Zhang, L. Zheng and K. Pruess, 2010. TOUGHREACT Version 2.0: A simulator for subsurface reactive transport under non-isothermal multiphase flow conditions. Computers and Geosciences (in press).

Young, C.L., 1986. In propane, butane and 2-methybutane. In: W. Hayduk (Editor), Solubility data series. Pergamon, Oxford.

Zarrella, W.M., R.J. Mousseau, N.D. Coggeshall, M.S. Norris and G.J. Schrayer, 1967. Analysis and significance of hydrocarbons in subsurface brines. Geochem. Cosmochim. Acta, 31: 1155--1166.

Zheng, L., J.A. Apps, Y. Zhang, T. Xu and J.T. Birkholzer, 2009. On mobilization of lead and arsenic in groundwater in response to CO_2 leakage from deep geological storage. Chemical Geology, 268(3-4): 281-297.

Appendix A

A1. Solubility of CO_2 in Water and Brine

The solubility of CO_2 in water or brine is computed using routines from ECO2N (Pruess, 2005), a fluid property module for the TOUGH2 simulator (Version 2.0) that was designed for applications to geologic sequestration of CO_2 in saline aquifers. ECO2N implements the mutual H_2O-CO_2 solubility model of Spycher et al. (2003) and Spycher and Pruess (2005), which was thoroughly tested against a large number of experimental data. To ensure correct implementation of the ECO2N solubility routines into TMVOC_REACT, published CO_2 solubilities in water at two temperatures were compared with values calculated by TMVOC_REACT. Comparisons between measured and calculated solubilities are shown in Figures A1 and A2. Also shown in Figure A1 are the results calculated by ECO2N. The close match indicates that the subroutine for the calculation of CO_2 solubilities in the aqueous phase has been correctly implemented in TMVOC_REACT.

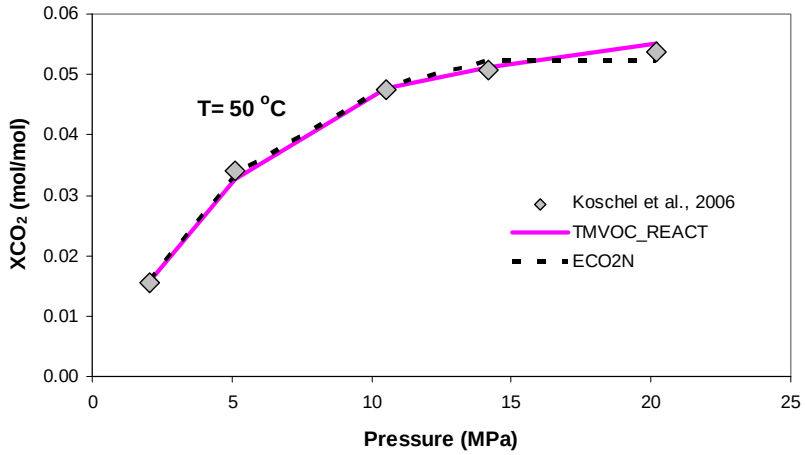

Figure A.1. Measured (Koschel et al., 2006) and calculated CO_2 solubilities in water at 50 °C by TMVOC_REACT and ECO2N.

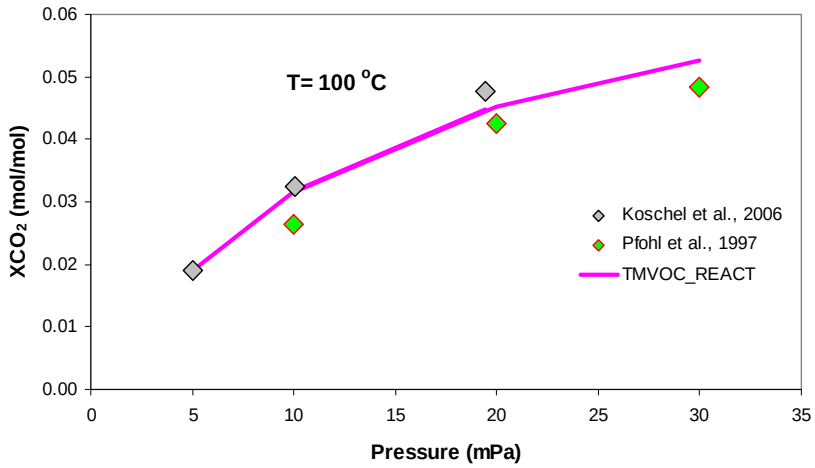

Figure A.2. Measured (Koschel et al., 2006; Pfohl et al., 1997) and calculated CO_2 solubilities in water at 100 °C by TMVOC_REACT (Pruess, 2005).

A2. Mutual Solubility of Benzene and Water

One of the main reasons benzene was selected in this study is its significant solubility in both water and SCC (Section 4.2). The phase behavior of the benzene-water system is shown in Figure A3. Although it covers mostly elevated temperatures, this phase diagram is still illustrative for low temperatures. A point below the three-phase equilibrium curve represents equilibrium between a liquid water-rich phase and vapor benzene-rich phase, while a point above the line represents equilibrium between benzene-rich and water-rich liquid phases. All three phases are at equilibrium at the three-phase equilibrium pressure.

Mutual solubilities can be measured at different pressure conditions. Usually, the mutual solubilities are measured along the three-phase equilibrium line, at given reported vapor pressures, such as in Chandler et al. (1998), Anderson and Prausnitz (1986), and Jou and Mather (2003). Some researchers (e.g., Sanemasa et al., 1982; 1987) were more interested in the solubility at low temperatures and measured the solubility of benzene in water at vapor-liquid equilibrium. Others researchers measured the solubility at liquid-liquid equilibrium (e.g., Neely et al., 2008; Miller and Hawthorne, 2000; Chen and Wagner, 1994)

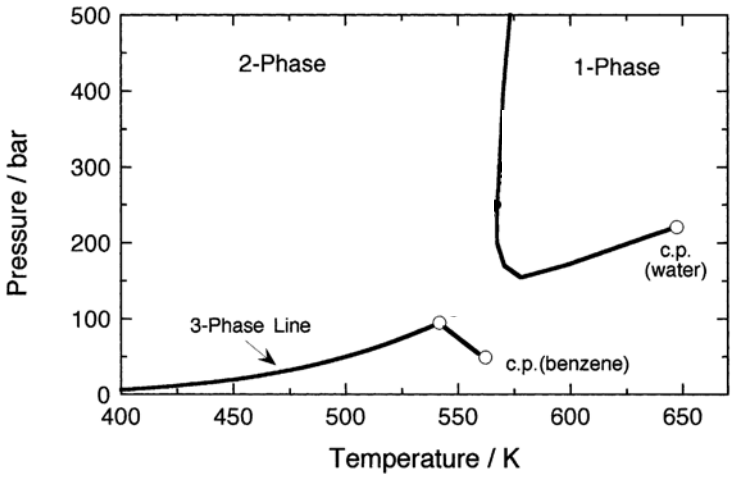

Figure A.3. Pressure–temperature phase diagram for the water–benzene mixture—thick solid lines: one-phase critical curve and liquid–liquid–vapor (LLV) three-phase equilibrium curve; c.p.: critical point (Furutaka and Ikawa, 2001).

Figure A4 shows the solubility of some hydrocarbons in water; among them, benzene is the most soluble. Reviews of benzene solubility are provided in compilations such as GSPA (2004) and Wagner (1999), the latter presenting an updated review of earlier reviews by Hefter (1989) and Young (1986). Tsonopoulos (2001) also reviewed the mutual solubility of hydrocarbons and water (including benzene), mainly focusing on data near 198.15 K. Additional references on the solubility of benzene in water at various temperatures and pressures are listed in Table A1. Most reported data are quite consistent, showing a significant increase in solubility with both temperature and pressure (Figures A5 and A6). The benzene solubility in water is well correlated with vapor pressure. However, when solubilities of benzene in water are measured at liquid-liquid equilibrium, measurements can be conducted for different temperatures (which yield different solubility values) but the same pressure (e.g., Miller and Hawthorne, 2000; see Figure A6), thus not allowing the correlation of solubility with pressure unless temperature data are provided.

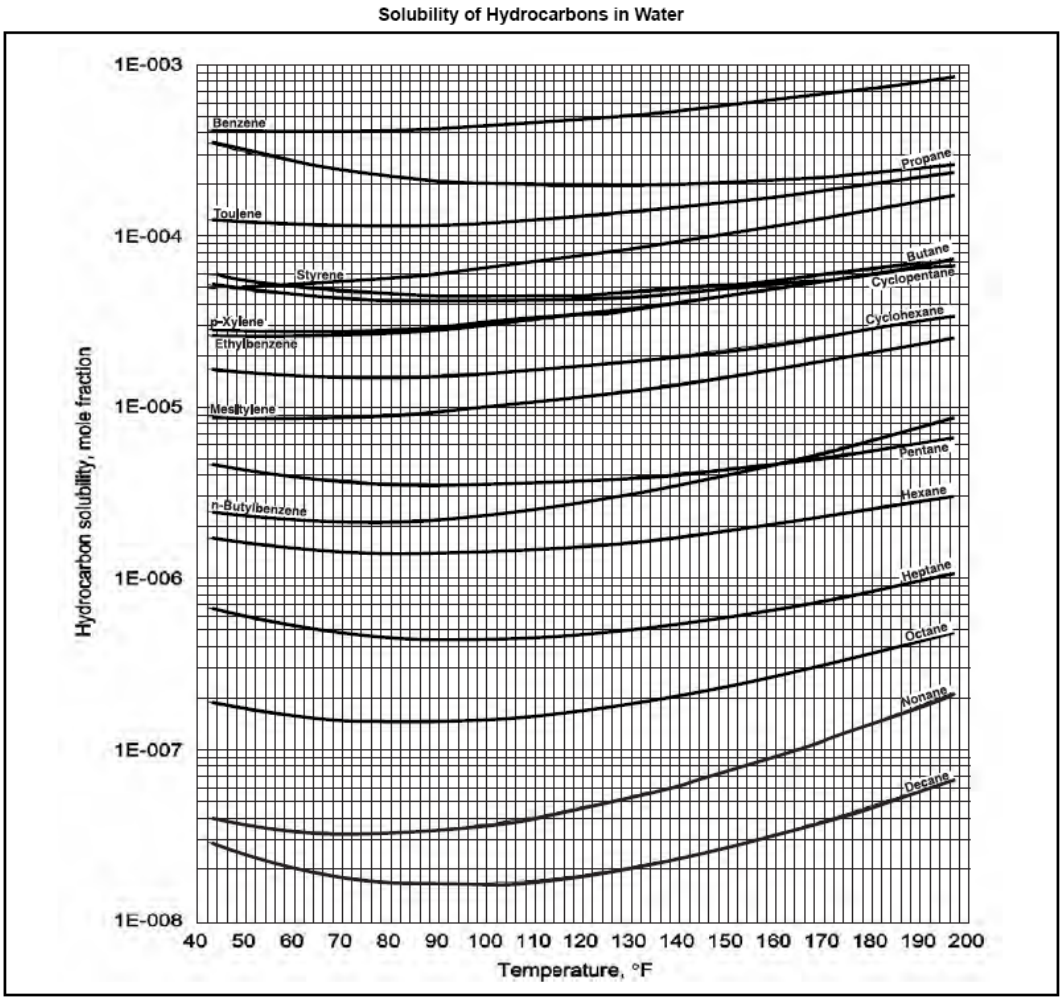

Figure A.4. Solubility of several hydrocarbons in water as a function of temperature at saturation pressures (GSPA, 2004).

Empirical equations have been developed to describe benzene solubility in water as a function of temperature. Neely et al. (2008), based on the reviews of Benson and Krause (1976) and Wilhem et al. (1977), selected the following equation to express the mole fraction of hydrocarbon as a function of temperature:

$$\ln x_{hc} = A + BT_{r,hc}^{-1} + CT_{r,hc}^{-2} \tag{A1}$$

where x_{hc} is the hydrocarbon mole fraction and $T_{r,hc}$ is the absolute temperature of the system divided by their critical temperature of the hydrocarbon. Neely et al. (2008) fitted measured solubility data for benzene in water, together with other published data, yielding A=11.09, B=-19.79 and C=5.176 for benzene. Tsonopoulos (2001) fitted measured solubility data with another equation:

$$\ln x_{hc} = A + B/T + C \ln T \quad \text{(A2)}$$

with A=–180.38, B=7524.83 and C= 25.8585.

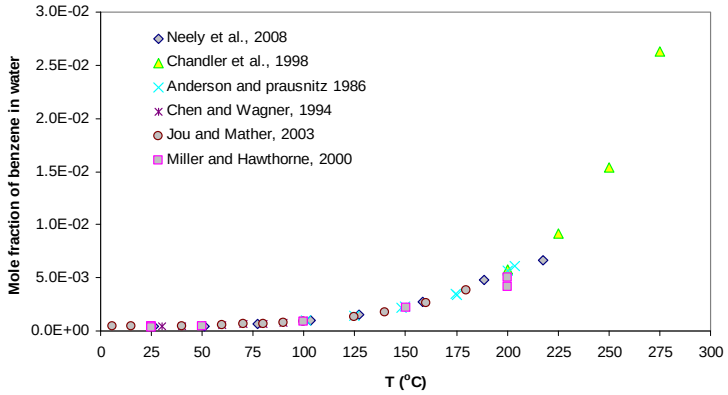

Figure A.5. Published solubility data for benzene in water, as a function of temperature (at saturation pressures).

Table A.1. List of references discussing the solubility of benzene in water

Reference	**T (°C)**	**P (bar)**	**Phase**
Sanemasa et al. (1982)	5-45	0.03-0.3†	Vapor-liquid
Sanemasa et al. (1987)	25	0.13†	Vapor-liquid
Neely et al. (2008)	26-218	2-69	Liquid-liquid
Chandler et al. (1998)	200-275	11-172	Vapor-liquid-liquid
Connolly (1966)	260-300	100-665	Near critical point,
Anderson and Prausnitz (1986)	101-203	2.8-32	Vapor-liquid-liquid Vapor pressure
Jou and Mather (2003)	6-180	0.058-20.3	Vapor-liquid-liquid Vapor pressure
Marche et al. (2003)	70-150	Not reported	
Miller and Hawthorne (2000)	25-200	1-400	Liquid-liquid, High pressure to maintain liquid water
Chen and Wagner (1994)	30-100	1-3.5	Liquid-liquid, Pressure is system pressure which is within 1 bar of three-phase pressure
Tsonopoulos (2001)	25	Not reported	

† The pressure value is the benzene partial pressure.

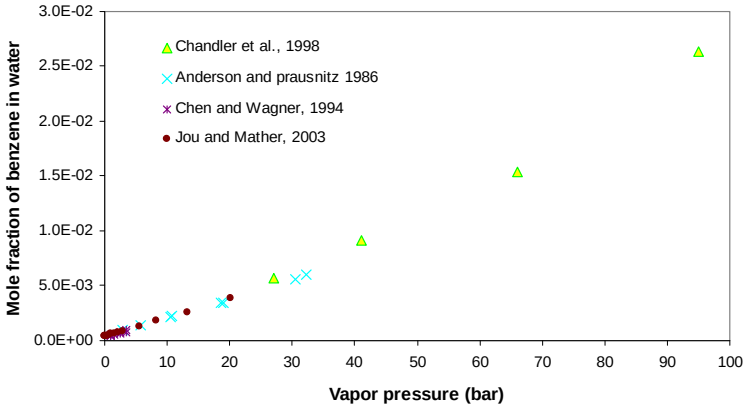

Figure A.6. Mole fraction of benzene in water as a function of vapor (total) pressure (at saturation temperatures).

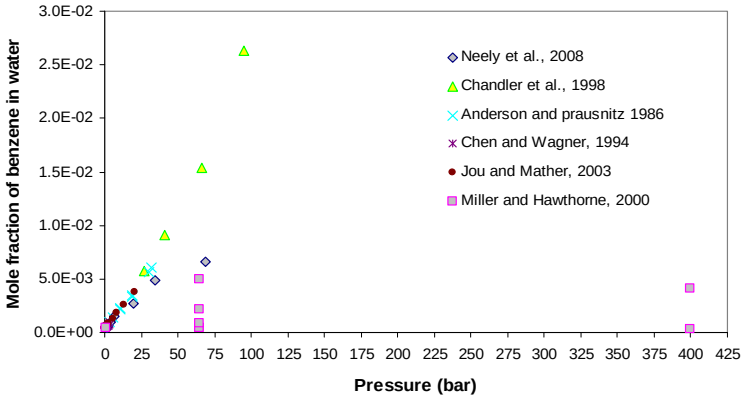

Figure A.7. Mole fraction of benzene in water as a function of pressure at liquid-liquid equilibrium at temperature ranging from 25–200°C (Miller and Hawthorne, 2000)) and along the three-phase pressure curve (Neely et al., 2008) at saturation temperatures.

A3. Reformulation of Solubility Data as Equilibrium Constants

The standard approach for calculating the mutual solubilities of liquids and compressed gases (by equating the fugacities of phases at equilibrium) is thoroughly described in the chemical engineering literature (e.g. Prausnitz et al., 1986). Spycher et al. (2003) used a similar approach derived from equating chemical potentials, but using conventions and standard states more typical of aqueous geochemistry studies. The approach relies on "true" equilibrium constants (K) (i.e., directly related to the standard Gibbs free energy of reaction) rather than the Henry's law constants (K_H) typically used in the chemical engineering literature.

At equilibrium, the following reaction and corresponding equilibrium constant can be written:

$$C_6H_{6(g)} \Leftrightarrow C_6H_{6(aq)} \quad K = a_{C6H6(aq)} / f_{C6H6(g)} \tag{A3}$$

where K is the "true" equilibrium constants, f is fugacity of the compressed "gas" benzene, and a is the activity of benzene in the aqueous phase.

The equilibrium constant K can be calculated from standard Gibbs free energy. The standard Gibbs free energy of formation for benzene, $\Delta G^0_{C_6H_6(g)}$, in an ideal gas at 25°C and 1 atm, is 1.297×10^5 J/mol (Reid et al., 1987). The Gibbs free energy of formation for benzene in the aqueous phase, $\Delta G^0_{C_6H_6(aq)}$, is 1.339×10^5 J/mol (Shock and Helgeson, 1990). Accordingly, $\Delta G^0_r = \Delta G^0_{C_6H_6(aq)} - \Delta G^0_{C_6H_6(g)} = 4188$ J/mol. The equilibrium constant K for Equation (A3) can be calculated according to the following relationship:

$$\Delta G^0_r = -RT \ln K \tag{A4}$$

where R is gas the constant (8.314 J $mol^{-1}K^{-1}$) and T is absolute temperature. Using Equation (A3) and the free energy of Equation (A4), the equilibrium constant K for this reaction is calculated to be 0.184 ($\log(K) = -0.7$) at 25°C and 1 bar. Values of K at higher temperatures and pressures are then extrapolated using published solubility data as described below.

From the definition of fugacity and partial pressure (e.g., Denbigh, 1983; Prausnitz et al., 1986), the benzene fugacity in Equation (A3) is expressed as

$$f_{C6H6(g)} = \phi_{C6H6(g)} y_{C6H6(g)} P_{tot} \tag{A5}$$

where $f_{C6H6(g)}$, $\phi_{C6H6(g)}$ and $y_{C6H6(g)}$ are the fugacity, fugacity coefficient, and mole fraction of benzene in the compressed "gas" phase, respectively, and P_{tot} is the total pressure. Values for $a_{C6H6(aq)}$, $y_{C6H6(g)}$ and P_{tot} were obtained from the literature. Fugacity coefficient values $\phi_{C6H6(g)}$ were then computed using TMVOC_REACT, yielding values of $f_{C6H6(g)}$ through Equation (A5). Log(K) values at different pressures and temperatures were then fitted to Equation (A3) using these fugacity values, and setting the activity of benzene in the aqueous phase ($a_{C6H6(aq)}$) equal to its concentration ($C_{C6H6(aq)}$) (effectively incorporating any deviations from non-unit activity coefficients into the computed log(K) values). Table A2 lists the log(K) values obtained in this way.

Table A.2. Mutual solubility data for the H_2O-benzene system vapor-liquid-liquid equilibrium at various temperatures and pressures, and fitted benzene log(K) values for Equation (3.3) (see text).

T (^{o}C)	P_{tot} (bar)	y_{H2O}	$C_{C6H6(aq)}$ (molal)	$\phi_{C6H6(g)}$	log(K)
Anderson and Prausnitz (1986)					
101	2.87	0.02135	0.05677	0.9331	-1.664
124.8	5.77	0.03658	0.077949	0.8871	-1.801
147.7	10.53	0.06081	0.120914	0.8241	-1.828
149.8	10.73	0.06513	0.127058	0.8232	-1.813
174.8	19.01	0.1058	0.194724	0.7289	-1.803
175.4	18.59	0.1053	0.189685	0.7375	-1.811
200.2	30.45	0.1792	0.315363	0.4157	-1.518
203.8	32.18	0.1886	0.339553	0.4173	-1.506
Chandler et al. (1998)					
200	27	0.188	0.320986	0.4634	-1.500
225	41	0.223	0.511739	0.4366	-1.434
250	66	0.394	0.869632	0.3848	-1.248
275	95	0.572	1.501777	0.3703	-1.001
Jou and Mather (2003)					
6	0.058	0.00168	0.022583	1	-0.4089
15	0.095	0.002285	0.022694	1	-0.6208
25	0.16	0.0032	0.022583	1	-0.8490
40	0.32	0.00492	0.02453	1	-1.113
60	0.7	0.00901	0.029539	1	-1.371
70	1.04	0.0113	0.033937	0.9693	-1.468
80	1.46	0.0157	0.037444	0.9601	-1.566
90	2.05	0.0204	0.042232	0.9481	-1.654
100	2.8	0.0258	0.048915	0.9343	-1.717
125	5.65	0.0461	0.073489	0.8894	-1.814
140	8.3	0.063	0.099702	0.8537	-1.823
160	13.2	0.0871	0.145496	0.7963	-1.819
180	20.2	0.13	0.214327	0.7226	-1.773

In addition to the three references listed in Table A1, the low temperature and pressure Henry's constants published by Sanemasa et al. (1982) for the benzene-H_2O system were also converted to log(K) values, neglecting departures from ideal behavior. These log(K) data were fitted as a function of temperature, assuming negligible pressure effect (given small Poynting factors estimated in the P-T range of gaseous benzene), yielding:

$$log(K) = -0.27046 - 2.324\times10^{-2}\ T + 8.321\times10^{-5}T^2 + 8.109\times10^{-8}T^3 - 4.076\times10^{-10}T^4$$

where T is temperature (°C). Figure A8 shows both the fitted log(K) values and fit results. This polynomial function was implemented in TMVOC_REACT and verified against experimental data (Figure A9). Generally, the solubilities calculated by TMVOC_REACT reproduce the measured data reasonably well, within acceptable margins for the objectives of this study.

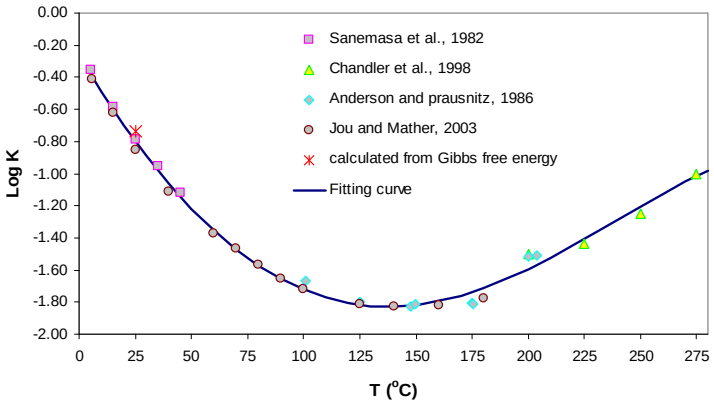

Figure A.8. Fitted equilibrium constant (log(K)) for Equation (3.3) compared to published solubility data and Henry's constants as a function of temperature (assuming negligible pressure effect over the fitted P-T range). Also shown is the log(K) calculated from published standard Gibbs free energy data at 25°C, 1 bar.

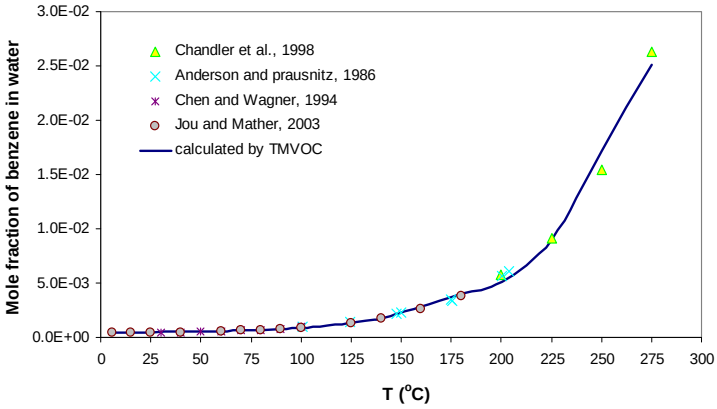

Figure A.9. Measured and computed mole fraction of benzene in water for benzene-H_2O vapor-liquid-liquid equilibrium as a function of temperature, ignoring pressure effects.

The log(*K*) derived from vapor-liquid-liquid equilibrium reflects the equilibrium of benzene in water with benzene in vapor. However, as shown in the phase diagram of benzene (Figure A3), benzene would be in the liquid state in the temperature and pressure range of most geological environments. Log(*K*) values for the benzene-H_2O system at liquid-liquid equilibrium could be derived from one set of correlations covering both vapor-liquid and liquid-liquid as a function of temperature and pressure. It is, however, more practical to develop another set of log(K) values for liquid-liquid equilibrium, in the same manner as done for vapor-liquid equilibrium. In this case, the reaction and corresponding equilibrium constant are written as:

$$C_6H_{6(l)} \Leftrightarrow C_6H_{6(aq)} \quad K = a_{c6h6(aq)} / f_{c6h6(l)} \tag{A6}$$

The data in Neely et al. (2008), together with the fugacity coefficient calculated by TMVOC_REACT, are used to calculate log(*K*) for Equation (A6) in the same manner as done previously. In this case, the fit of log(*K*) data yields:

$$log(K) = -1.7327 - 6.074\times10^{-4}\,T - 6.3342\times10^{-5}T^2 + 7.8003\times10^{-7}T^3 - 2.0518\times10^{-9}T^4,$$

with temperature T given in °C. Figure A10 shows the calculated log(*K*) values and the resulting fit. Although Miller and Hawthorne (2000) also reported some solubility data for liquid-liquid equilibrium, their data are not considered here because they did not report the solubility of water in the benzene-rich phase.

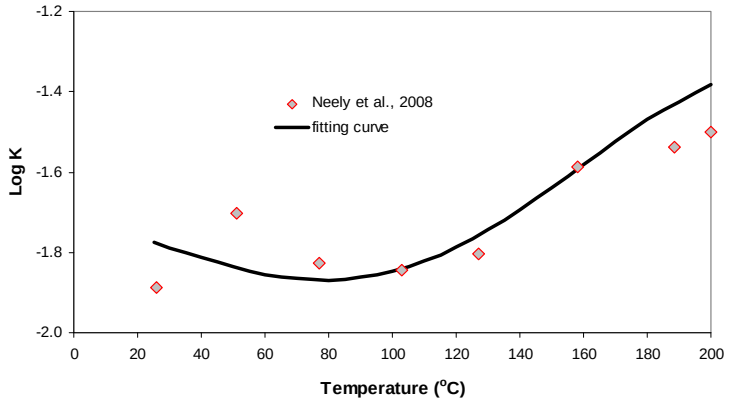

Figure A.10. Equilibrium constants for the equilibrium between liquid benzene and benzene in water calculated from Neely et al. (2008) and the fitting polynomial equation.

Both sets of log(*K*) values are then implemented into TMVOC_REACT (one for vapor-liquid-liquid and the other for liquid-liquid equilibrium). For a given temperature, the code then calculates the vapor pressure of the system. If the total pressure is higher than the vapor pressure of the mixture, benzene is in the liquid phase, and the log(*K*) for reaction (A6) is used. Otherwise, the log(K) for Equation (A3) is used.

A4. Binary Benzene + CO_2 System

The liquid-vapor phase equilibria of the binary benzene + CO_2 system have been widely studied. Table A3 lists some references in which liquid-vapor phase equilibria were reported. Figures A11 and A12 show the vapor pressure of benzene + CO_2 mixture at 25°C and 40°C. Also shown in Figures A13 and A14 are the vapor pressure of pure benzene (VP C6H6) and pure CO_2 (VP CO_2). An ideal solution obeys Raoult's law, according to which the total vapor pressure of the mixture is a linear function of the composition (the mole fraction of CO_2 in benzene in this case). As seen in Figures A13 and A14, measured vapor pressures are close to the straight line drawn between the vapor pressure of pure benzene and CO_2, indicating a relatively narrow departure from ideal behavior.

Francis (1954) reported that benzene and near-critical CO_2 are fully miscible at room temperature and 6.6 MPa. Hawthorne and Miller (2003), in a study related to supercritical fluid extraction of benzene from soils, indicate that benzene and SCC are fully miscible.

This behavior is properly accounted for by the equation-of-state module for gas mixtures in TMVOC_REACT.

Table A.3. List of references discussing mutual solubility data for the binary benzene + CO_2 system.

Reference:	T	P
Bendale and Enick (1994)	42.3-79.85	17-112
Kim et al. (1986)	70-110	5-60
Ohgaki and Katayama (1976)	25, 40	14-76
Gupta et al. (1982)	40, 80,120	74-133
Lay et al. (2006)	20,25,35	17-73.1

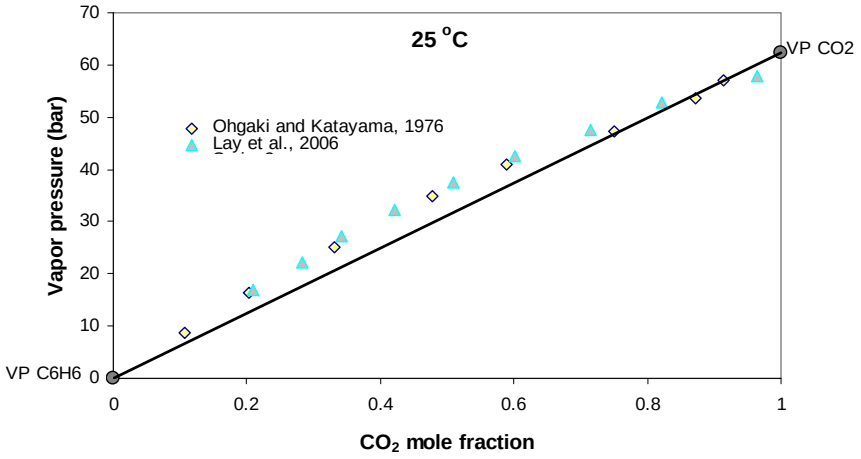

Figure A.11. Published vapor pressure data versus CO_2 mole fraction in the liquid phase at 25°C for the benzene-CO_2 system. "VP C6H6" is the vapor pressure of pure benzene whereas "VP CO_2" is that of pure CO_2.

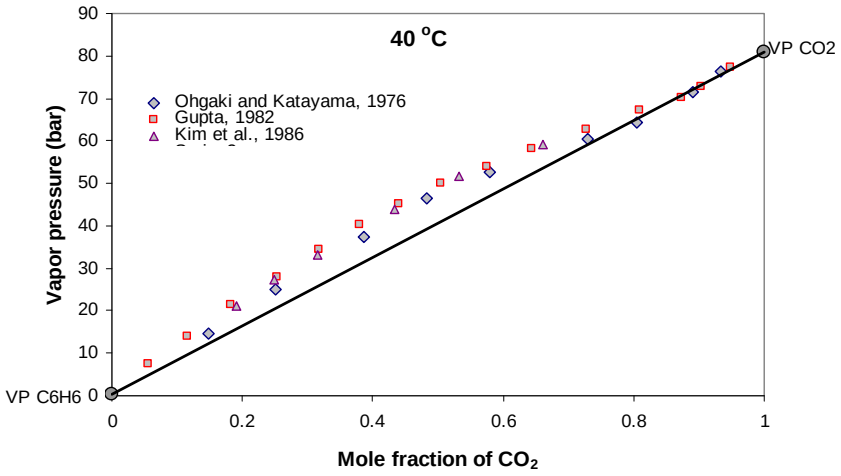

Figure A.12. Published vapor pressure data versus CO_2 mole fraction in the liquid phase at 40°C. "VP C6H6" is the vapor pressure of pure benzene while "VP CO_2" is that of pure CO_2.

A5. Ternary Benzene+CO_2+Water System.

The partition coefficient of benzene in SCC in the presence of water is one of the key parameters affecting benzene mobilization by SCC. TMVOC_REACT calculates this partitioning from its equation of state for gas mixtures, together with equilibrium constants for the binary systems as presented previously. To verify that proper partitioning is computed when all three phases (benzene, SCC, and H_2O) are present, we conducted a literature search for partition coefficients of the 3-phase system. This partition coefficient can be defined as (Green and Akgerman, 1996):

$$K_i = \frac{n_i^{SCF} / n^{SCF}}{n_i^{H_2O} / n^{H_2O}} \qquad \text{(A7)}$$

where n_i^{SCF} / n^{SCF} is the mole fraction of organic species *i* in the supercritical fluid, and $n_i^{H_2O} / n^{H_2O}$ is the mole fraction of organic species *i* in water.

If mass fraction instead of mole fraction is used, K_i can be converted to $(K_i)_m$as:

$$(K_i)_m = K_i \left(\frac{MW^{H2O}}{MW^{CSF}} \right) = \frac{m_i^{SCF} / m^{SCF}}{m_i^{H_2O} / m^{H_2O}}$$

where m_i^{SCF} / m^{SCF} is the mass fraction of organic specie *i* in SCC and $m_i^{H_2O} / m^{H_2O}$ is mass fraction of organic species *i* in water.

Partition coefficients K_i for benzene have not been widely reported. Measured K_i by Ghonasgi et al. (1991) are the only data found in our literature search. The partition

coefficients calculated by TMVOC_REACT were verified against these data. As illustrated in Figures A13 and A14, the calculated values are slightly lower than the measured data at 40°C, whereas they agree reasonably well at 50°C. It should be noticed that Ghonasgi et al. (1991) observed a large scatter in the distribution coefficients for benzene, and pointed out that even small errors in concentrations could generate significant scatter in their partition coefficient values. Given this scatter, results from TMVOC_REACT (Figures A13 and A14) are reasonable. The differences between measured and calculated K_i reflect differences in measured and calculated benzene concentrations in the aqueous phase (mole fraction, x_i) (Figure A17), which may be the result of ignoring pressure effects in the calculation of log(K) values for the benzene-water system (Appendix A3), in addition to measurement variability. Note that Ghonasgi et al. (1991) did not directly report x_i values. The values listed in Table A4 were calculated using Equation (A7) and their reported measured K_i and y_i values. Because this study aims at evaluating, in a semi-quantitative manner, the potential mobilization of benzene by SCC, and not at predicting accurately water contamination for a given site, the reproduction of their partition coefficients within a factor of less than two and largely within the scatter of their data is deemed sufficient.

Table A.4. Published partition coefficient of benzene between SCC and water (Ghonasgi et al., 1991). y_i and x_i are the mole fraction of benzene in SCC and water, respectively.

Temperature (°C)	Pressure (bar)	K_i	y_i	x_i
40	96.5	1957.8	0.000202	1.03E-07
40	110.25	3809.6	0.000393	1.03E-07
40	124.04	3726.4	0.000390	1.05E-07
40	138	3645.9	0.000376	1.03E-07
40	151.6	3102.3	0.000423	1.03E-07
40	165.4	3941.2	0.000510	1.03E-07
50	96.5	981.82	0.000101	1.03E-07
50	110.25	1648.1	0.000170	1.03E-07
50	124.04	1252.1	0.000129	1.03E-07
50	138	1324.6	0.000240	1.03E-07
50	151.6	1654.2	0.000171	1.03E-07
50	165.4	1553.1	0.000263	1.03E-07

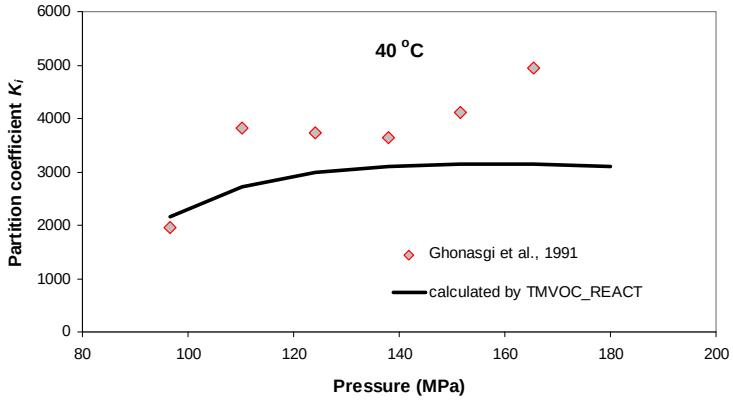

Figure A.13. Comparison of measured partition coefficients of benzene between water and SCC (symbols) and calculated values by TMVOC_REACT at 40°C (line).

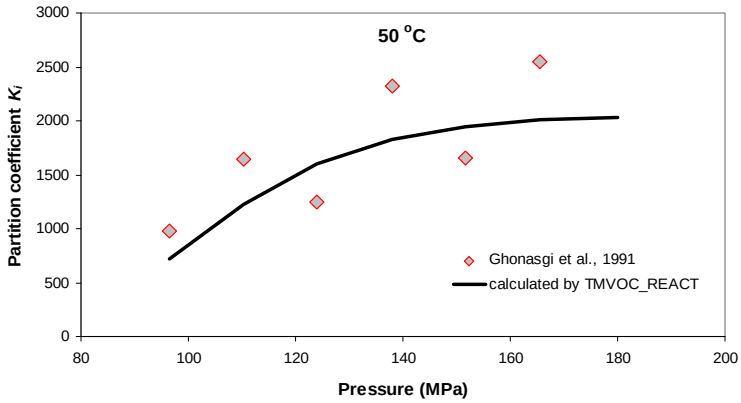

Figure A.14. Comparison of measured partition coefficients of benzene between water and SCC (symbols) and calculated values by TMVOC_REACT at 50°C (line).

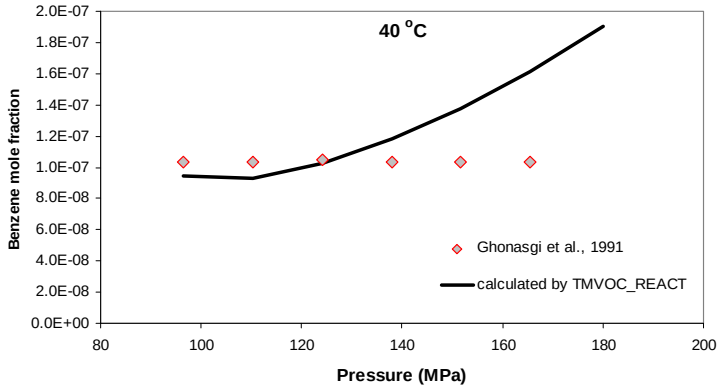

Figure A.15. Comparison of benzene mole fraction in water, x_i, derived from experimental measurements (symbols), and calculated values by TMVOC_REACT at 40°C (line).

A6. PVT Properties of H_2S + CO_2 Mixtures

Mixtures of H_2S and CO_2 are an important nonaqueous system in acid-gas injection. The phase behavior of such mixtures has been investigated experimentally (e.g., Bierlein and Kay, 1953; Robinson and Bailey, 1957), and these data were subsequently used to verify numerical models (Kamath and Potoff, 2006; Morris and Byers, 1991). Figure A18 shows the P-T diagram for the H_2S + CO_2 system. Under the pressure and temperature conditions in the storage formation assumed in this report (about 200 bar and 75°C), a mixture of H_2S + CO_2 would be in supercritical condition. Morris and Byers (1991) compared the predictions of the Peng-Robinson (PR) and Soave-Redlich-Kwong (SRK) equations of state with data measured by Bierlein and Kay (1953), and concluded that the calculated phase equilibria for H_2S + CO_2 mixtures based on both equations agree well with measured data. The binary interaction parameters for a H_2S + CO_2 system used in Morris and Byers (1991) are 0.0989 for PR and 0.0997 for SRK. Here, we used the SRK option of the GASEOS routine in TMVOC_REACT, with a binary interaction parameter equal to 0.101 (Walas, 1985). Because (1) the capability of equations of state to reproduce measured data has been proved by Morris and Byers (1991), (2) the same equations of state are used in TMVOC_REACT, and (3) the interaction parameter in TMVOC_REACT is very close to that reported by Morris and Byers (1991), testing against experimental data for this system was not deemed necessary.

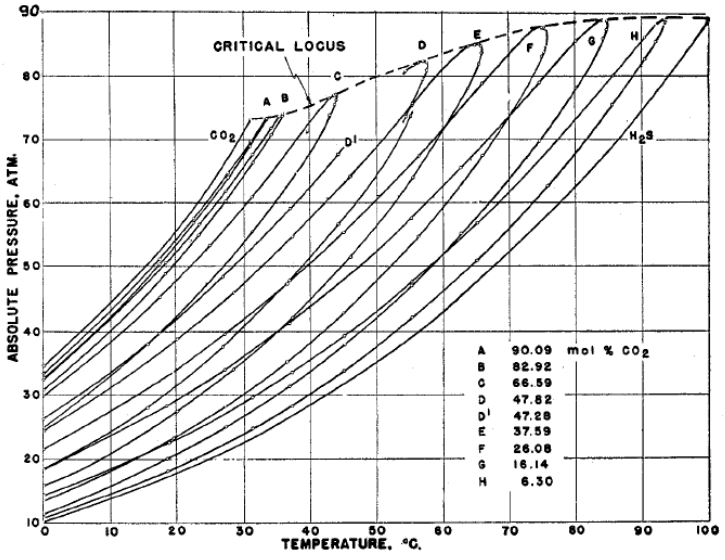

Figure A.16. Pressure-Temperature diagram for H_2S+CO_2 mixtures (Bierlein and Kay, 1953)

A7. Solubility of H_2S in Water

As done for CO_2 (Spycher et al., 2003) and benzene (see Sections A1 and A3), solubilities of H_2S in water are computed using "true" equilibrium constants (K) (i.e., directly related to the standard Gibbs free energy of reaction) rather than Henry's law constants (K_H). At equilibrium, the following reaction and corresponding equilibrium constant can be written:

$$H_2S_{(g)} \Leftrightarrow H_2S_{(aq)} \quad K = a_{H2S(aq)} / f_{H2S(g)} \tag{A8}$$

where K are "true" equilibrium constants, f are fugacities of the gas components, and a are activities of components in the aqueous phase.

The thermodynamic model presented by Duan et al. (2007) is used here to calculate the equilibrium constant. They proposed the following equation to calculate the solubility of H_2S in water and NaCl solution:

$$\ln \frac{y_{H_2S(g)} P}{m_{H_2S(aq)}} = \frac{\mu^{(0)}_{H_2S(aq)}}{RT} - \ln \phi_{H_2S(g)} + \ln \gamma_{H_2S(aq)} \tag{A9}$$

where $y_{H_2S(g)}$ is the mole fraction of H_2S in gas phase, P is pressure, $m_{H_2S(aq)}$ is the concentration of H_2S in aqueous phase, $\mu^{(0)}_{H_2S(aq)}$ is the standard chemical potential of H_2S in aqueous phase, $\phi_{H_2S(g)}$ is the fugacity coefficient of H_2S in the gas phase, and $\gamma_{H_2S(aq)}$ is the activity coefficient of dissolved H_2S.

Rewriting Equation (A9) yields

$$\ln \frac{\phi_{H_2S(g)} y_{H_2S(g)} P}{\gamma_{H_2S(aq)} m_{H_2S(aq)}} = \frac{\mu^{(0)}_{H_2S(aq)}}{RT} \tag{A10}$$

Considering that

$$K = \frac{a_{H_2S(aq)}}{f_{H_2S(g)}} = \frac{\gamma_{H_2S(aq)} m_{H_2S(aq)}}{y_{H_2S} P \phi_{H_2S}} \tag{A11}$$

we arrive at:

$$\ln K = -\frac{\mu^{(0)}_{H_2S(aq)}}{RT} \tag{A12}$$

The right-hand term $\frac{\mu^{(0)}_{H_2S(aq)}}{RT}$ is a function of temperature and pressure that takes the form (Duan et al., 2007):

$$par(T,P) = c_1 + c_2 T + c_3/T + c_4 T^2 + c_5/(680-T) + c_6 P + c_7 P/(680-T) + c_8 P^2/T \quad \text{(A13)}$$

with parameters $c_1 - c_8$ given by Duan et al. (2007, Table 2).

Equation (A13) is used to compute K values for H_2S. The H_2S solubility is then computed using Equation (A8), noting that $a_{H2S(aq)} = m_{H_2S(aq)} \gamma_{H_2S(aq)}$, with m and γ representing molality and activity coefficient, respectively. Duan et al. (2007) used a virial expansion of excess Gibbs energy to calculate $\gamma_{H_2S(aq)}$. Here, however, we use the equation presented by Drummond (1981), which is more easily implemented and provides results very close to those of Duan et al. (2007):

$$ln(\gamma_{H2S(aq)}) = (0.2905\text{-}1.574\times10^{-4}T\text{-}46.2/T)\cdot I - (0.5705\text{-}1.777\times10^{-3})\cdot I/(1+I)$$

where T is the temperature (K) and I is the ionic strength of the solution (molality). This approach was verified against experimental data (Tables A6 and A7, Figures A23–A27). The fairly good match between calculated and measured solubilities in NaCl solutions demonstrates that TMVOC_REACT is capable of calculating the solubility of H_2S in solutions with NaCl concentrations up to ~6 molal. Experimental data considered in the code verification are further discussed below.

Reviews of H_2S solubility in water and brines are presented by Chapoy et al. (2005), Duan et al. (2007), and Koschel et al. (2007), as well as in an earlier study by Carroll and Mather (1989). Table A5 summarizes some of the existing data at conditions of interest for CO_2 geological sequestration. Note that the critical point for pure H_2S is at T_c ~100°C and P_c ~90 bar (e.g., Sakoda and Uematsu, 2003), and the upper critical end point for H_2S+H_2O mixtures is at T_{UCEP} ~ 132°C and P_{UCEP} ~ 123 bar (dos Ramos and McCabe, 2010). Therefore, data points for the H_2S+H_2O system (no CO_2) in the pressure and temperature range relevant to geologic sequestration fall in the subcritical region.

Table A.5. List of literature discussing H_2S solubility in water (note that published data at pressure around 1 bar are not included in this table)

Reference	Solution	T ^oC	P (bar)	Number of measurement	Comments
(Suleimenov and Krupp, 1994)	NaCl (0-2.5M)	20-320	0-140	72	Solubility of H2S at saturation pressure is given as function of T.
(Selleck et al., 1952)	Pure water	37-170	6-210	50	Data at high temperature are not reliable
(Lee and Mather, 1977)	Pure water	10-180	1-70	355	Cited in (Duan et al., 2007)
(Gilespie et al., 1984)	Pure water	38-204	10-210	44	Cited in (Duan et al., 2007)
(Xia et al., 2000)	NaCl (4-6 M) Na_2SO_4 (0-1 M) $(NH_4)_2SO_4$ (1.9-4 M)	40-120	10-100	225	
(Pohl, 1961)	Pure water	30-43	17	15	
(Koschel et al., 2007)	Pure water	50-120	17-31	12	
(Chapoy et al., 2005)	Pure water	5-40	25-65	31	
(Burgess and Germann, 1969)	Pure water	50-170	17-23	35	Cited in (Chapoy et al., 2005)

Table A6 compares H_2S solubilities measured by Suleimenov and Krupp (1994) with values computed using TMVOC_REACT, showing good agreement except for one large deviation (at 40.4°C and 2.64 bar) attributed either to a transcript or experimental error. Experimental data in a similar temperature range were also presented by Drummond (1981), falling within 7–10% of the data from Suleimenov and Krupp (1994).

Table A.6. Measured H_2S solubility (x= mole fraction) by Suleimenov and Krupp (1994) and calculated value by TMVOC_REACT.

T (°C)	P (bar)	xH_2S_exp	xH_2S_cal	error%*
24.20	2.22	0.004125	0.004170	1.1
21.40	2.60	0.005089	0.005251	3.1
40.40	2.64	0.000102	0.003402	188.4
23.50	2.95	0.005483	0.005645	2.9
22.40	3.93	0.007651	0.007727	1.0
20.80	4.25	0.008977	0.008700	3.1
21.30	4.29	0.008519	0.008669	1.7
40.00	4.53	0.006065	0.005929	2.3
22.30	4.96	0.009886	0.009787	1.0
60.20	5.00	0.004591	0.004477	2.5
22.80	5.41	0.010297	0.010497	1.9
35.60	5.56	0.007657	0.007993	4.3
100.80	7.44	0.004145	0.003774	9.4
22.80	7.90	0.015546	0.015227	2.1
85.80	8.66	0.005835	0.005419	7.4
84.60	9.48	0.006525	0.006054	7.5
155.40	11.59	0.003028	0.002829	6.8
153.60	13.30	0.003991	0.003744	6.4
142.60	15.82	0.006290	0.005652	10.7
140.80	15.91	0.006147	0.005808	5.7
151.00	16.03	0.005501	0.005174	6.1
150.80	16.06	0.005472	0.005202	5.1
155.10	16.36	0.005289	0.005024	5.1
156.20	18.04	0.006346	0.005708	10.6
167.10	20.45	0.006316	0.005911	6.6
199.80	21.12	0.002475	0.002585	4.3
206.20	27.07	0.004115	0.004321	4.9
193.50	27.28	0.006405	0.006201	3.2
216.50	27.55	0.002475	0.002748	10.5
196.20	27.99	0.006176	0.006174	0.0
198.20	28.45	0.006032	0.006104	1.2
221.10	37.42	0.006514	0.006405	1.7
229.60	42.59	0.006691	0.007020	4.8
232.40	43.24	0.006442	0.006686	3.7
234.70	44.81	0.006487	0.006876	5.8
234.30	44.98	0.007066	0.007052	0.2
242.50	49.29	0.006818	0.006989	2.5
242.60	49.46	0.006745	0.007047	4.4
256.40	55.11	0.005128	0.005536	7.7
254.80	56.89	0.006632	0.006975	5.0
266.00	62.63	0.005319	0.005752	7.8
274.60	65.41	0.002868	0.003423	17.6
264.10	72.85	0.011850	0.011660	1.6
273.00	73.33	0.007103	0.008352	16.2
279.10	86.35	0.012592	0.012427	1.3
291.80	89.38	0.007747	0.007467	3.7
300.70	99.92	0.008022	0.007909	1.4
310.90	112.86	0.008561	0.008194	4.4
321.00	138.61	0.015358	0.015816	2.9

* $error = \frac{\left|(xH_2S\_\exp - xH_2S\_cal)\right|}{(xH_2S\_\exp + xH_2S\_cal)/2} \times 100$

Chapoy et al. (2005) reported a set of data measured at low temperature and pressure conditions (T<70°C, P<40 bar). The comparison of measured data and calculated values at 35°C, 45°C, 55°C, and 65°C (Figure A19 and A20) shows that TMVOC_REACT is capable of reproducing measured data at low temperatures and pressures. Pohl (1961) measured solubilities at 17 bar as a function of temperature, and values calculated from TMVOC_REACT also match closely with his data set (Figure A21).

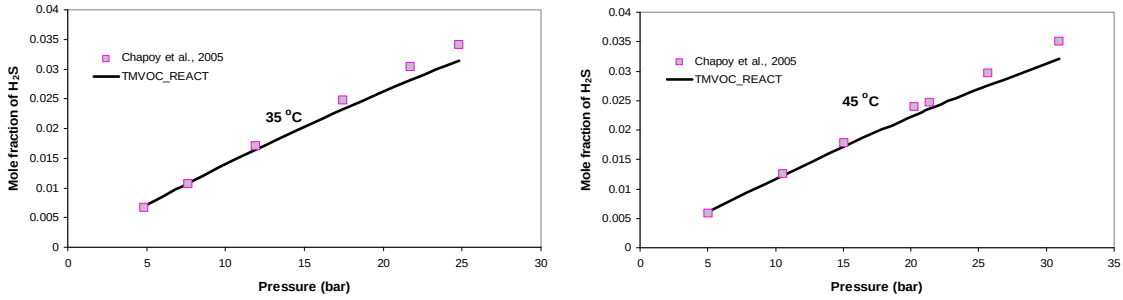

Figure A.17. Measured (Chapoy et al., 2005) and calculated H_2S solubilities in water at 35°C (right) and 45°C (left).

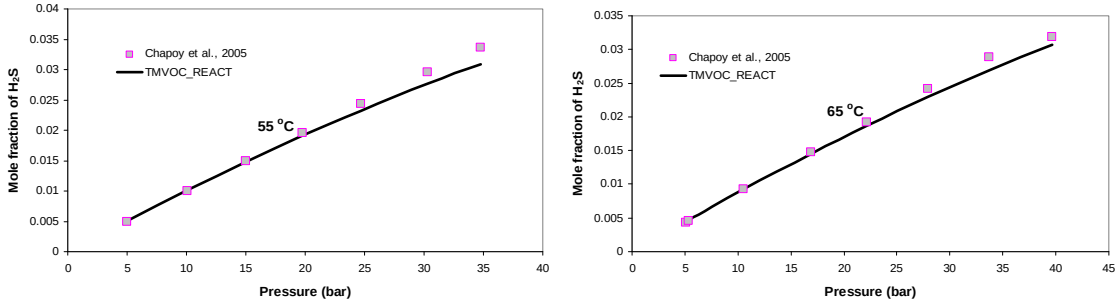

Figure A.18. Measured (Chapoy et al., 2005) and calculated H_2S solubilities in water at 55°C (right) at 65°C (left).

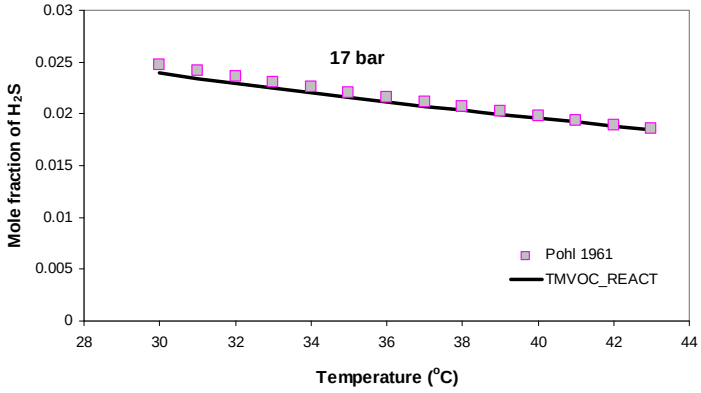

Figure A.19. Measured (Pohl, 1961) and calculated H_2S solubilities in water as a function of temperature at pressure of 17 bar.

The solubilities measured by Chapoy et al. (2005) are mainly for low temperatures and pressures, whereas those measured by Suleimenov and Krupp (1994) cover a larger temperature and pressure range. TMVOC_REACT was also tested against measured data at relatively low temperature (about 50–100°C) but rather high pressure—thus conditions more relevant for CO_2 geological sequestration. Figure A22 shows the comparison of measured and calculated solubility values at 71°C at pressures ranging from about 10 to 200 bar, indicating a reasonably good agreement. Note that the small discontinuity in the solubility curve at around 60 bar is not physical. It is caused by the phase change from gaseous to liquid H_2S, which cannot be accurately reproduced using a simple cubic equation of state (PR), as done here. This discontinuity, however, is inconsequential for the work presented in this study and vanishes in the CO_2+H_2S+H_2O system as the presence of CO_2 lowers the upper critical end point temperature (i.e., the phase transition occurs at much lower temperatures). For comparison, results from TMVOC incorporating Henry's constants from d'Amore and Truesdell (1988) are also shown in Figure A.22 Clearly, the solubility routines implemented in TMVOC_REACT improve the accuracy of calculating H_2S solubility in water compared to those used in TMVOC. Further tests were also conducted with measured data from other sources (Figure A.23).

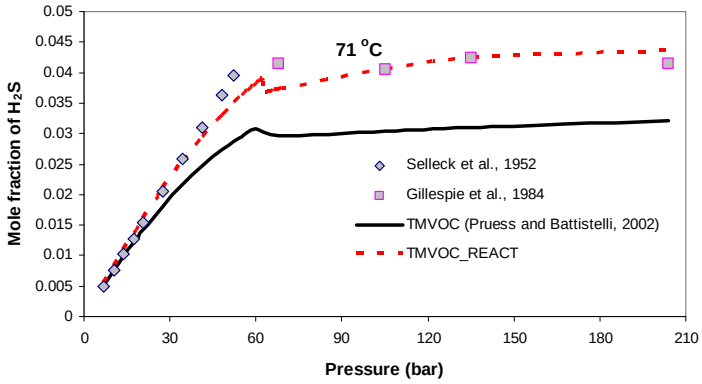

Figure A.20. Measured (Gilespie et al., 1984; Selleck et al., 1952) and calculated H_2S solubilities in water by TMVOC_REACT and TMVOC (Pruess and Battistelli, 2002)

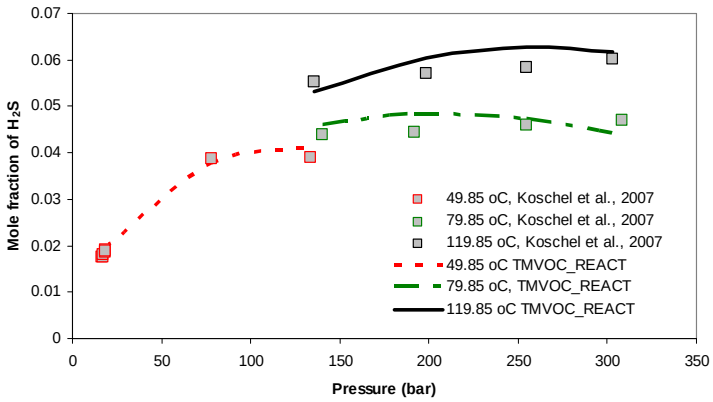

Figure A.21. Measured (Koschel et al., 2007) and calculated H_2S solubilities in water by TMVOC_REACT.

The effect of salinity on the solubility of H_2S (the salting-out effect), has also been tested with TMVOC_REACT against measured data (Xia et al., 2000), and showed reasonably good agreement up to ~6 M NaCl (Figures A24–A27).

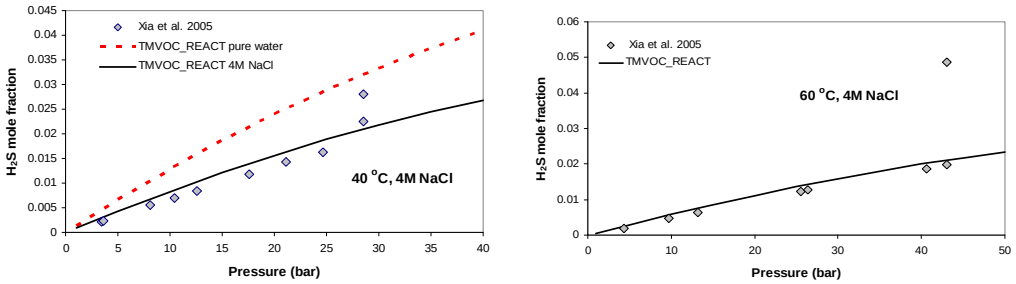

Figure A.22. Measured (Xia et al., 2000) and calculated H_2S solubilities in 4M NaCl solution at 40°C (right) and 60°C (left).

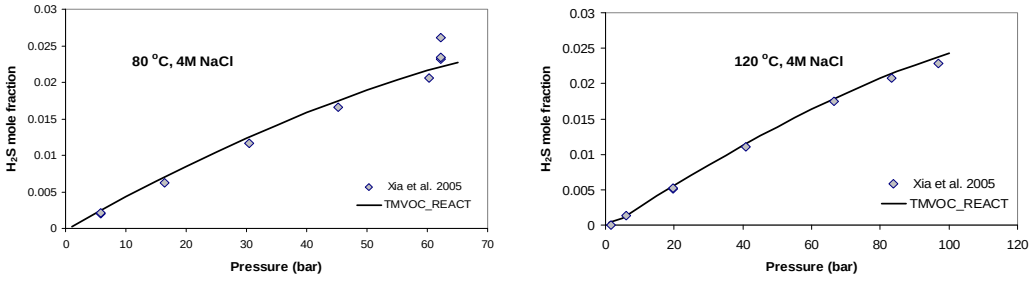

Figure A.23. Measured (Xia et al., 2000) and calculated H_2S solubilities in 4M NaCl solution at 80°C (right) and 120°C (left).

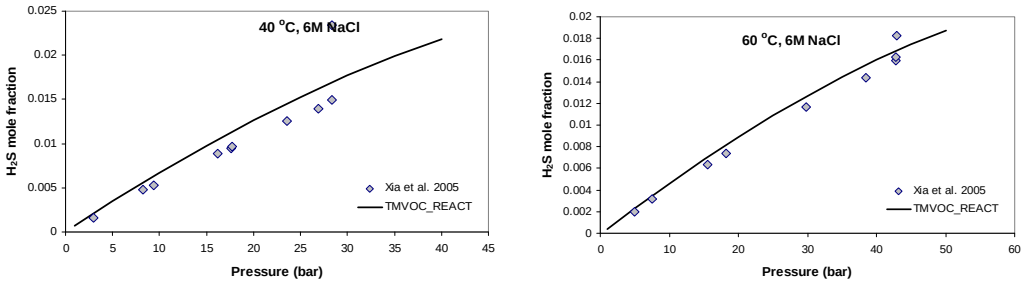

Figure A.24. Measured (Xia et al., 2000) and calculated H_2S solubilities in 6M NaCl solution at 40°C (right) and 60°C (left).

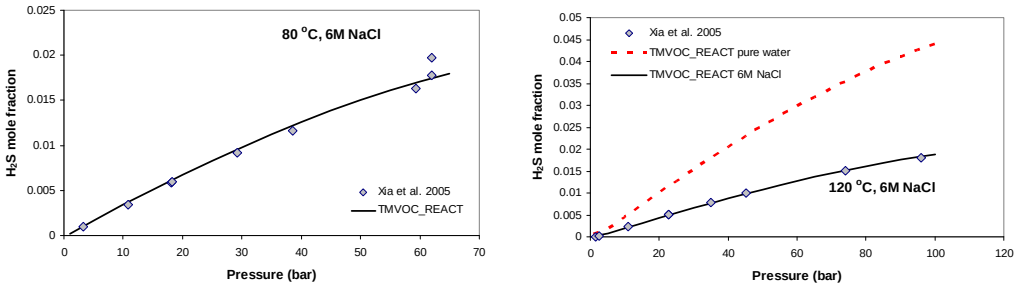

Figure A.25. Measured (Xia et al., 2000) and calculated H_2S solubilities in 6M NaCl solution at 80°C (right) and 120°C (left).

A8. Distribution of Benzene between Kerogen and Water

The distribution of benzene between soil and water has been studied in the field of environmental remediation for cleaning organic contaminated soils (for example, Hawthorne and Miller, 2003). Usually a K_d (distribution coefficient) approach is applied. The distribution coefficient between soil and water is defined as:

$$K_d = \frac{m_i^S / m^S}{m_i^{H_2O} / m^{H_2O}} \tag{A14}$$

where m_i^S and $m_i^{H_2O}$ is the mass of organic species *i* in the sediments and water respectively, m^S and $m_i^{H_2O}$ is the mass of sediments and water respectively. Note that K_d in Equation (A14) is dimensionless. Alternatively, K_d can also take units of mL/g or L/kg if expressed as a ratio of concentrations (i.e., mg/kg_{soil} divided by mg/L_{water}). Table A7 lists some published K_d values, which show a large variation. Also shown in Table A7is the weight fraction of organic carbon in sediments, f_{oc}, calculated based on a K_{oc} of 79 ($logK_{oc}$=1.9) , (the definition of f_{oc} and K_{oc} will be discussed later.

Table A.7. Compilation of published K_d for benzene between soil and water

Reference	K_d (mL/g)	f_{oc}	Comments
Larsen et al. (1992)	0.05-0.65	0.00063-0.0082	Measured for aquifer samples which are located at various places in Denmark and have a great variety.
Donahue et al. (1999)	0.1-1.0	0.0013-0.013	Measured for Regina clay in Canada
Jean et al. (2002)	0.16-0.5	0.0021-0.0063	Measured in a laboratory experiment for artificial medium-size sand
Hawthorne and Miller (2003)	28-59	0.35-0.75	Measured for manufactured Gas Plant Soils (contaminated by organic compounds)

The large range of measured K_d values is primarily due to the dependence of K_d on the organic matter content of soils, which is quite variable. In other words, K_d is soil specific, and the same K_d value is not necessarily applicable to a range of different soil types. Moreover, the experimental methods followed to determine K_d values can significantly affect significantly measured K_d values. Green and Akgerman (1996) observed differences in K_d of up to 74% depending on the method used.

Although the value of K_d depends on the properties of sediments, the hydrophobic partitioning theory as reviewed by Karickhoff et al. (1979) implies that the partitioning of a specific compound between water and organic carbon, as expressed by K_{oc}, is largely independent of the organic content of the solid material. K_d can be calculated from K_{oc} by the equation:

$$K_d = f_{oc} \times K_{oc} \tag{A15}$$

where $f_{oc} = m_{oc}^S / m^S$ is the mass fraction of organic carbon in sediments, defined as the mass of organic carbon in sediments m_{oc}^S divided by the mass of sediments. K_{oc} may be thought of as the ratio of the amount of chemical adsorbed per unit weight of organic carbon in the soil to the concentration of the chemical in solution at equilibrium:

$$K_{oc} = \frac{m_i^S / m_{oc}^S}{m_i^{H_2O} / m^{H_2O}} \tag{A16}$$

K_{oc} is usually related to K_{ow} by:

$$\log K_{oc} = a \log K_{ow} + b \tag{A17}$$

where K_{ow} is the octanol/water partition coefficient.

Karickhoff et al. (1979) reported the following equation from least squares fitting for $logK_{oc}$ versus $logK_{ow}$.

$$\log K_{oc} = 1.0 \cdot \log K_{ow} - 0.21 \tag{A18}$$

Table A8 lists some published values for K_{ow} and K_{oc}. Mackay et al. (1992) reported that the *log* K_{oc} ranges from 1.09 to 2.53 with a median around 1.8–2.0.

Table A.8. Published K_{ow} and K_{oc} (unitless).

$logK_{ow}$	$logK_{oc}$	Reference
2.1	1.9	Karickhoff et al. (1979)
2.13[§]	1.92[¥]	Inel and Iseri (1997)
	1.09–2.53	Mackay et al. (1992)
	1.89	PouIson et al. (1997)

[§] Inel and Iseri (1997) complied the experimental K_{ow} based on the work of Chiou et al. (1977), Mackay et al. (1980) and Whitehouse and Cooke (1982) and the average values of $logK_{ow}$ is 2.13.
[¥] calculated from Equation (A18)

The mass transfer between the aqueous and solid phases is a key process for leaching of benzene by CO_2. The K_d approach is used to calculate the release of adsorbed benzene into the aqueous phase via the surface complexation model (SCM) capability implemented into TMVOC_REACT. This requires the conversion of K_d values to K_{SCM} values, which represent sorption intrinsic equilibrium constants input into the simulator. Basically, the following reaction applies:

$$SOH\_C_6H_6 \rightleftharpoons C_6H_6(aq)+SOH \tag{A19}$$

where $_{SOH\_C_6H_6}$ is sorbed benzene concentration (the "surface complex") and SOH is the concentration of unoccupied sorption sites, both in units of mol/kg_{water}. The (intrinsic) sorption constant is then given as:

$$K_{scm}=\frac{[C_6H_6][SOH]}{[SOH\_C_6H_6]} \tag{A20}$$

where brackets represent concentration (mol/kg_{water}), assuming ideal solution behavior. The total concentration of sorption sites is equal to the sum of [SOH_C_6H_6] and [SOH]. Considering that [SOH_C_6H_6] is much smaller than [SOH], the total concentration of sorption sites is roughly the same as [SOH]. The total mass of sorbing organic matter (m^S_{oc}) and the mass of sorbed benzene (m^S_i) can then be related directly to [SOH] and [SOH_C_6H_6] by:

$$\frac{[SOH]}{[SOH\_C_6H_6]}=\frac{m^S_{oc}\,/\,f_{oc}\cdot Sd\cdot A}{m^S_i\,/\,W} \tag{A21}$$

where *Sd* is sorption site density (mol/m^2), *A* is specific surface area of the sorbent (m^2/g) and *W* is the molecular weight of benzene. By combining Equations A20 and A21 the sorption constant $_{K_{SCM}}$ can then be related to K_{oc} as follows:

$$K_{SCM} = \frac{[C_6H_6(aq)][SOH]}{[SOH\_C_6H_6]} = m_i^{H_2O} / m^{H_2O} \times 1000/W \cdot \frac{m_{oc}^S / f_{oc} \cdot Sd \cdot A}{m_i^S / W} = m_i^{H_2O} / m^{H_2O} \times 1000/W \cdot \frac{Sd \cdot A \cdot W}{f_{oc} \cdot m_i^S / m_{oc}^S}$$

$$= 1000 \cdot \frac{Sd \cdot A}{f_{oc} \cdot \frac{m_i^S / m_{oc}^S}{m_i^{H_2O} / m^{H_2O}}} = 1000 \cdot \frac{Sd \cdot A}{f_{oc} \cdot K_{oc}}$$

(A22)

Therefore, as shown in Equation (A22), one needs to estimate values of *Sd, A, K_{oc} and* f_{oc} to calculate values of K_{SCM} for input into the model. Baldi and Bargagli (1982) measured the specific area of marine sediments ranging from 10 to 40 m^2/g. Kulp and Carr (1952) reported specific surface areas of deep-sea sediment ranging from 2.5 to 48 m^2/g. Based on these values, we assume a specific surface area of 10 m^2/g. A site density of 10^{-6} mol/m^2 is used as a starting point to yield an assumed 1×10^{-4} ppm benzene in the soil (about 0.01 ppm in kerogen) at an aqueous benzene concentration of 0.001 mg/L, and K_{oc} and f_{oc} values discussed below. Sensitivity analyses are then conducted to account for variabilities and uncertainties in these data. A K_{oc} value of 1.9 is selected, based on the values shown in Table 4.10, which are quite consistent. Considering that f_{oc} values for natural or uncontaminated soil ranges from 0.0006 to 0.013 (Table 4.9), we assume a value of 0.01, which falls in the higher range of these data. Using these assumed values for *Sd, A, K_{oc} and* f_{oc}, the calculated $\log K_{SCM}$ based on Equation (A22) is –1.9. These data correspond to an initial aqueous benzene concentration of 1.28×10^{-8} mol/kg_{water} (~0.001 mg/L), and adsorbed benzene concentration of 1.23×10^{-8} mol/kg_{water} (corresponding to 1×10^{-4} ppm in the sediment, and corresponding to 0.01 ppm in kerogen).